Hydrokinetic Turbine

Featuring Variable Flux Generation

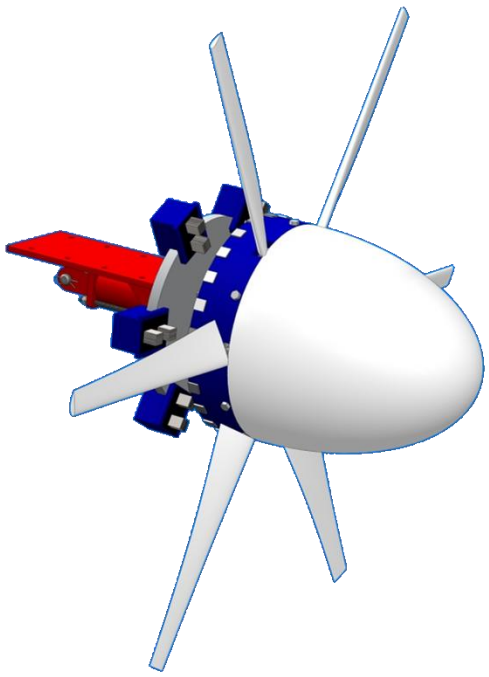

Nathaniel Allen
Patrick Kilar
Brian Roy

TECH 797: Ocean Projects
2010 – 2011

University of New Hampshire

Sea Grant
New Hampshire

Acknowledgements

This work is the result of research sponsored in part, by the National Sea Grant College Program, NOAA, Department of Commerce, under grant #NA06OAR4170109 through the New Hampshire Sea Grant College Program.

We would like to thank the faculty and staff of the Ocean Engineering and Mechanical Engineering Departments at the University of New Hampshire. A special acknowledgement to our faculty advisors Kenneth Baldwin and Martin Wosnik for their knowledge, advice, time and support throughout the year; Ben Brickett for providing advice and expertise in regards to Variable Flux Generation; Bob Champlin and Paul Lavoie for their machining assistance and use of tools; Jennifer Bedsole for her administrative assistance with ordering and finances; Cabot Trott for his expertise and time manufacturing the rotor blades; Adam Perkins for his electrical assistance and time spent developing a time-delay controller; and lastly Matt Rowell for all his help behind the scenes.

Abstract

With global energy demand on the rise and fossil fuel supplies diminishing there is a growing market for renewable electrical energy. The Department of Energy (DOE) has stated that "marine and hydrokinetic energy technologies have a significant potential to contribute to the nation's future supply of clean, cost-effective renewable energy." Hydrokinetic turbines extract the energy available in tidal, ocean or river currents. Because water is 832 times denser than air, these currents represent a powerful, highly-concentrated and currently untapped clean energy resource.

An ongoing research project at the University of New Hampshire is looking into a more efficient way to extract the vast amount of energy in this renewable resource. The research is focused on energy conversion with a horizontal axis turbine and a direct drive generator featuring Variable Flux Generation (VFG). This choice of technology is intended to provide a simple and robust system that will have the ability to efficiently utilize low velocity tidal currents for power generation. Therefore, the turbine will be able to generate power over a wider range of flow velocities compared to a conventional hydrokinetic turbine. This will allow more energy to be harvested from the flow resulting in a more efficient turbine with greater net power generation.

The first generation of this project proved that VFG technology could be implemented in a marine environment on a hydrokinetic turbine. However, their proof-of-concept VFG-based hydrokinetic turbine proved to be neither efficient nor durable. For the second generation, the main focus was to increase the overall efficiency of the turbine by improving both the rotor and generator designs. In addition, the project was also focused on improving the reliability and lifetime by building a more robust turbine able to withstand the harsh marine environment.

One of the biggest improvements made on the generator was doubling the diameter of the magnet ring from the first generation design. A larger magnet ring diameter increases the tangential velocity of the magnets which creates more magnetic flux in the coils leading to a larger electrical output of the generator. The larger diameter also provided space for a greater number of magnets and twice the number of stator coils. This alone doubled the potential power output compared to the first generation. To improve the rotor, new blades were designed using Blade Element Momentum (BEM) theory, which is extensively used in the wind turbine industry. A generalized rotor design code using this theory was programmed in Matlab. The code was used to derive the ideal blade twist, chord taper and coefficient of performance as well as lift and drag forces. The ideal blade design was chosen based on overall performance and structural integrity.

The turbine was designed to be deployed in the Piscataqua River at the UNH Tidal Energy Test Site located at the General Sullivan Bridge in Portsmouth, New Hampshire. Preliminary bench top-testing of the generator has indicated the turbine will be able to output upwards of 2.5 Kilowatts of power at a rotational speed of 120 RPM. This rotational speed corresponds to a flow velocity of 3 m/s, the max velocity expected at the test site, and a designed tip-speed-ratio of 3. The turbine will be deployed at the test site in May 2011 and data will be taken on the torque produced by the rotor and the overall power production. From the gathered performance data the overall efficiency of the hydrokinetic turbine can be benchmarked.

Table of Contents

List of Figures

List of Tables

1 – Introduction

1.1 – Purpose

Traditional turbines cannot produce electricity below a certain "cut-in" speed due to high start-up torque experienced in conventional permanent magnet generators. The purpose of this project was to develop a new hydrokinetic turbine with the ability to efficiently utilize low velocity tidal currents previously untouched by conventional devices. The new turbine design incorporates a unique new direct drive generator technology, Variable Flux Generation. This technology promotes the controlled axial engagement of a ring of permanent magnets (rotor) with respect to a stationary ring of yoke type coils (stator) thereby eliminating high start-up torque. This will allow the turbine to operate over a wider range of flow velocities enabling more energy to be extracted from the flow resulting in a more efficient turbine with greater net power generation.

1.2 – Background

The global energy demand is projected to steadily increase over the next forty years and due to the increasing threat of diminishing fossil fuels; there is a growing effort to meet these demands using renewable energy resources. The Department of Energy's 2009 Annual Energy Review reported that in the United States the electrical generation sector has the greatest energy consumption at 40 percent of the total energy consumed. Of that 40 percent only 11 percent currently comes from renewable energy resources. The electric generation sector therefore provides one of the best opportunities for renewable energy resources to expand and help meet this increasing global demand.

The oceans cover more than 70 percent of the Earth and have long been appreciated as a vast energy source. The energy is stored in the oceans partly as thermal energy and partly as kinetic energy (waves and currents). Because water is 832 times denser than air, these currents represent a powerful and highly-concentrated clean energy resource. If a suitable hydrokinetic technology can be developed for harnessing this energy, a sustainable and predictable electrical energy supply could be produced.

Although tidal, ocean and river currents provide an attractive renewable energy source; they are still predominantly untapped and unutilized. This is because hydrokinetics are at a relatively early stage of development and maturity compared to other renewable energy technologies like wind or solar energy. However, the US Department of Energy has stated that marine hydrokinetics have "significant potential to contribute to the nation's future supply of clean, cost-effective renewable energy." The US Department of Energy is a leading organization helping to advance research and development of this technology.

1.3 – Scope

This report covers the design and development of a horizontal axis hydrokinetic turbine featuring a new generator technology. The report begins by discussing the background and theory of hydrokinetics. Next the report covers the research and design of the turbine including major design considerations, component improvements and manufacturing methods. This section of the report was broken down into major components; rotor, generator, actuation and structure. The report concludes with performance testing results and recommendations for future generations.

2 – Background

2.1 – What is Variable Flux Generation?

Variable Flux Generation (VFG) is a direct drive generator technology that enables wind or water turbines to efficiently utilize low velocity flows for power generation. Therefore the generator can produce power over a wider range of flow speeds starting at very low velocities. The technology achieves this by allowing a ring of permanent magnets (rotor) to engage axially with respect to a stationary ring of yoke type coils (stator). The engagement of the magnetic rotor with respect to the stator plate is controlled by the hydrodynamic drag force on the rotor. The magnet rotor ring is initially disengaged from the stator coils eliminating the high start-up torque by allowing the rotor to spin easily with no magnetic resistance. As the flow speed increases, the magnet rotor ring is engaged into the stator coils. The amount of engagement is directly dependent on the speed of the flow. This is pictorially shown below in Figure 2.1.

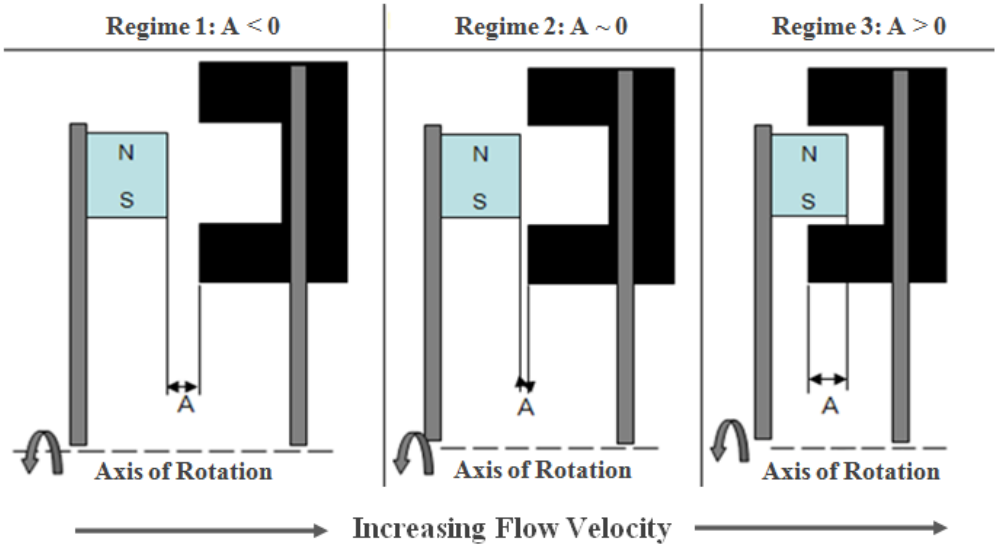

Figure 2.1: Axial engagement VFG generator

As the magnet ring engages into the stator yokes the magnetic flux being captured by the coils increases. As larger amounts flux is captured in the coils more electricity is generated. This is best represented by the chart below in Table 2.1. This table represents two flow regimes; low current speeds and high current speeds. The ability to generate power in both flow regimes is something that is uniquely possessed only by VFG machines.

Table 2.1: VFG flow regimes

Low Flow Velocity	High Flow Velocity
❖ Small drag force	❖ Large drag force
❖ Minimal magnet-coil engagement	❖ Maximum magnet-coil engagement
❖ Rotor spins easily, low torque	❖ Rotor spins with high torque
❖ Small power generation	❖ Maximum power generation

2.2 – Previous Work

This is the second year that students at the University of New Hampshire have researched implementing a hydrokinetic turbine featuring Variable Flux Generation. The first generation was a feasibility study to determine if VFG technology could be implemented in a marine environment on a hydrokinetic turbine. Previously, VFG technology had only been implemented on wind turbines. The first generation team was able successfully prove this. The turbine they designed was tested in the tow tank at the Chase Ocean Engineering Laboratory as shown in the figure below. Testing at a 1.5 m/s tow velocity, their turbine was able to produced 21 Watts of power at 70 RPM. Although, this proof-of-concept VFG-based hydrokinetic turbine worked, it proved to have a small power output and was neither efficient nor durable.

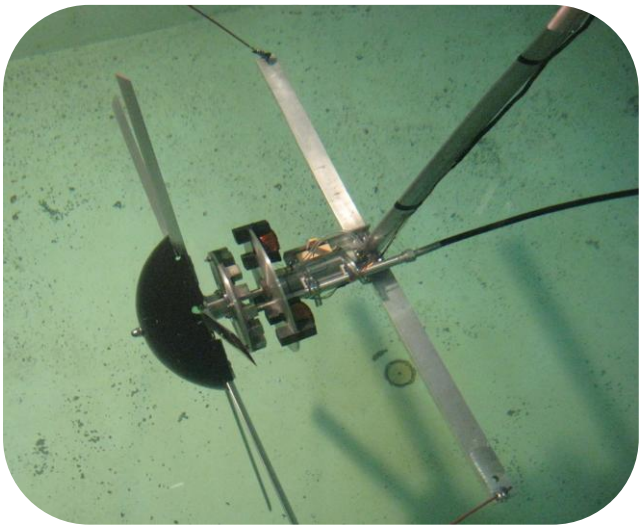

Figure 2.2: First generation VFG turbine

For the second generation design, the main focus was to increase the overall power output and efficiency of the turbine by improving both the rotor and generator designs. In addition to this, the project also focused on improving the reliability and lifetime of the device by building a more robust turbine able to endure the harsh marine environment.

2.3 – UNH Tidal Energy Test Site

The UNH Tidal Energy Test Site is part of the UNH Center for Ocean Renewable Energy (CORE) testing infrastructure. The site is located on the Piscataqua River at the General Sullivan Bridge in Newington, NH. At this site approximately 40 percent of the volume of Great Bay flows under the bridge every tidal cycle. This site is also where the Lower Piscataqua enters Little Bay through a constriction. This results in peak current speeds of greater than 4 knots (2 m/s) which are considered some of the highest tidal current velocities in North America. The tidal range at the site is nominally 8.2 ft (2.5 m). This site is considered a full-scale test site for vertical axis turbines and a “large-scale” test site for horizontal axis turbines. An aerial view of the New Hampshire Sea cost is shown in the figure below. In the figure the UNH Tidal Energy Test site is indicated as well as the other UNH CORE facilities and open water sites.

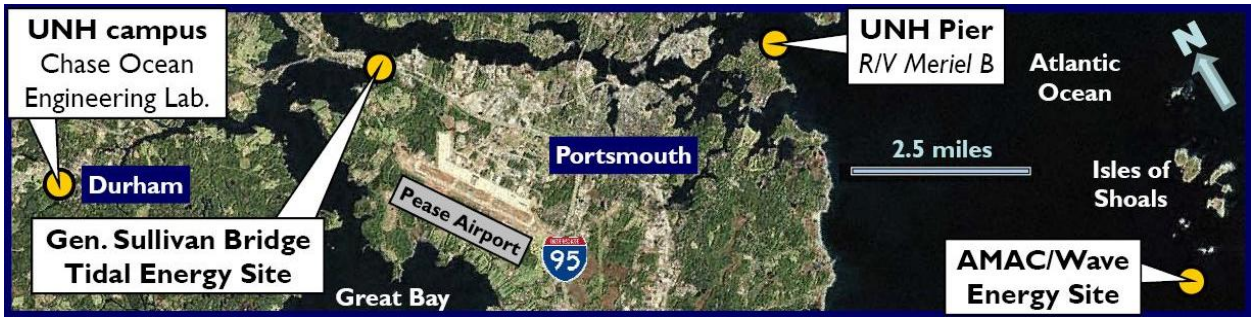

Figure 2.3: Arial view depicting the UNH CORE facilities and test sites

2.4 – Open Water Deployment Infrastructure

A sister group of students at the University of New Hampshire has been concurrently working on developing a deployment structure for horizontal axis hydrokinetic turbines. Their structure is designed to be mounted to the first generation UNH Test Barge. The Test Barge is a twin hull deck barge which was initially equipped with a derrick to raise and lower a cage containing a Gorlov style vertical axis turbine. The horizontal axis deployment structure has a tripod configuration and is made out of airfoil shaped struts to greatly reduce drag and improve testing conditions. The structure is designed to have a universal mounting box for easy attachment of any in-stream turbine. The structure is intended to be raised into place from beneath the barge. This allows the structure the ability to mount moderate sized horizontal axis turbines (~5 ft diameter). The structure has been analyzed and built to withstand the hydrodynamic drag forces expected on a 5 foot diameter turbine. The deployment structure and the UNH Test Barge are shown below in Figure 2.4.

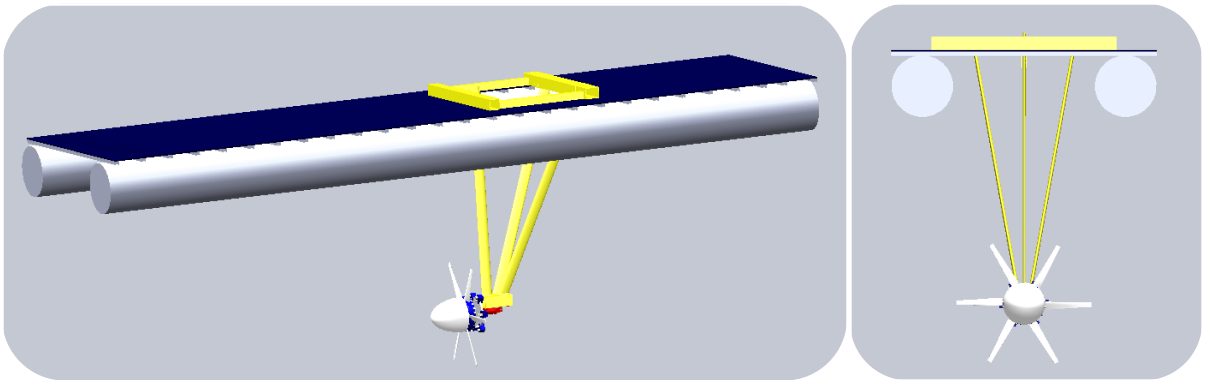

Figure 2.4: UNH Test Barge and Turbine Deployment Structure

3 – Rotor

3.1 – Introduction

The most important component of any turbine with respect to performance is the rotor. This is because in any given flow there is a finite amount of kinetic energy and the rotor is the component of a turbine which converts this kinetic energy into usable energy. The more efficient a rotor is the more energy a turbine will potentially be able to harvest from a flow. A rotor generally consists of three main parts: blades, nose cone and a hub.

3.2 – Theory

3.2.1 – Energy Extraction

The total theoretical power available in a flow of fluid is

$$P_{theoretical} = \frac{1}{2}\rho A U^3,$$

where ρ is the density of the fluid, A is the swept area of the rotor and U is the free stream velocity of the fluid. Because the density and swept area are assumed constant, the theoretical power in a flow is assumed proportional to the cube of its velocity.

In hydrokinetics the marine currents tend to be very slow compared to wind speeds, however since the density of water is 823 times greater than air, the energy content of a marine current of only 1 m/s is equivalent to a wind speed of 9 m/s. The theoretical power for a flow of 6 knots with a 5 foot diameter rotor would be 8.4 Kilowatts.

The power that a turbine can actually extract from a fluid flow will be reduced by the efficiencies of the device. The actual power that can be extracted from a flow is

$$P_{actual} = \eta_R \eta_M \eta_E \frac{1}{2}\rho A U^3,$$

where η_R is the rotor efficiency which is typically referred to as the power coefficient, C_P; η_M is the mechanical efficiency of the device and incorporates transmission, bearing and gearbox losses; η_E is the electrical efficiency which includes the generator and power conditioning losses.

Generally the electrical and mechanical efficiencies are very high, usually around 0.9. These efficiencies are typically much greater than the rotor efficiency. The maximum theoretical possible rotor power coefficient is defined by the Betz limit and is 16/27 or 0.593. This is based on an idealized model and therefore in practice efficiencies of less than 0.5 are generally seen.

3.2.2 – Angle of Relative Flow

It can be seen that blades designed for optimum power production have an increasingly large chord and twist angle as one gets closer to the blade root. The blade is designed with twist so

that each blade cross section will have an optimal angle of attack to the relative flow that is experienced by the blade. The angle and magnitude of the relative flow is dependent on the free stream velocity as well as the tangential velocity of each blade section. Below in Figure 3.1 is a velocity vector diagram that shows a blade cross section and its tangential velocity vector, the velocity vector of the free stream velocity and the relative velocity vector which is the vector sum of the previous two.

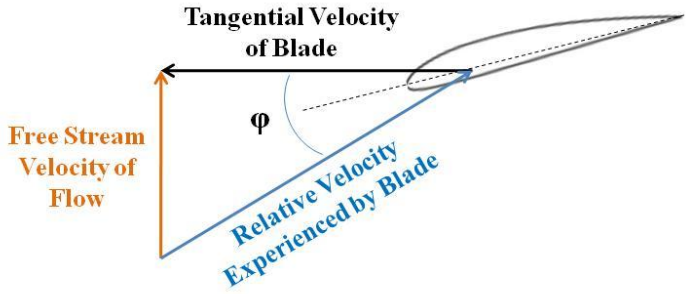

Figure 3.1: Velocity vector diagram of blade cross section

The angle of relative flow is the angle between the relative velocity vector and the rotor plane of rotation. This angle is depicted as φ in Figure 3.1 above. If the free stream velocity is assumed to be constant than that velocity vector will remain the same magnitude. The change of the angle of relative flow is created because the blade cross section at the blade tip is traveling at a greater tangential velocity than the blade cross section at the rotor hub. This change in tangential velocity changes the geometry of the vector diagram as seen below in Figure 3.2.

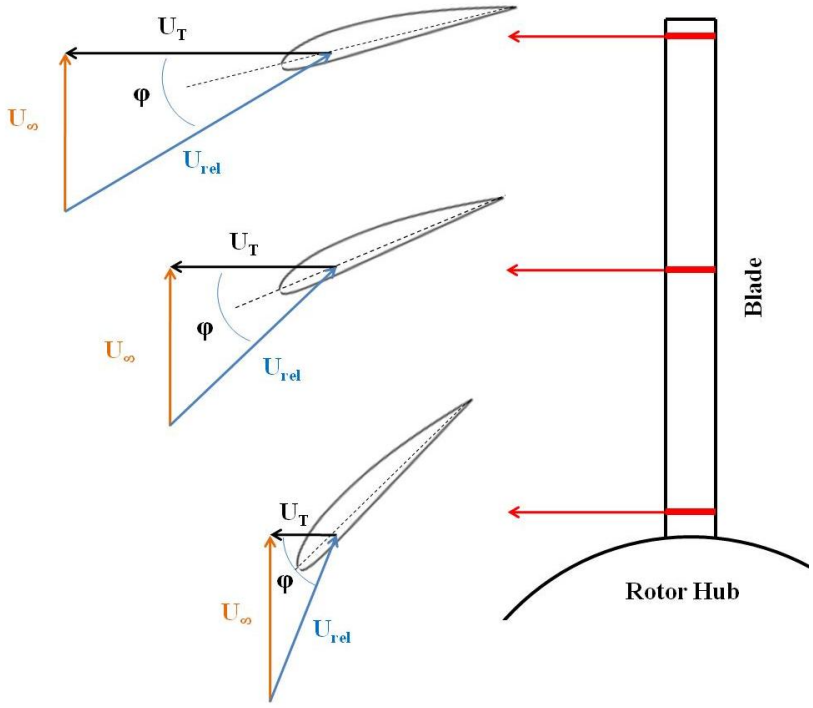

Figure 3.2: Vector diagrams showing the rotation of the relative velocity vector

3.2.3 – General Aerodynamic Concepts

A hydrokinetic turbines power production depends on the interaction between the rotor and the current flow. Most horizontal axis turbine blade designs use airfoils to develop mechanical power. Airfoils are structures with specific geometric shapes that are used to generate mechanical forces due to the relative motion of the airfoil and the surrounding fluid flow.

Airfoil Terminology

The chord, *c*, of the airfoil is the straight line distance between the leading and trailing edges. The angle of attack, α, is defined as the angle between the chord line and the relative wind, U_{rel}. The thickness of an airfoil is the distance between the top and bottom surfaces measured perpendicular to the chord line. The mean camber line is the line that lies halfway between the upper and lower surfaces. If the airfoil is symmetric the mean camber line lies on the chord line. This terminology is shown pictorially on an airfoil profile below in Figure 3.3.

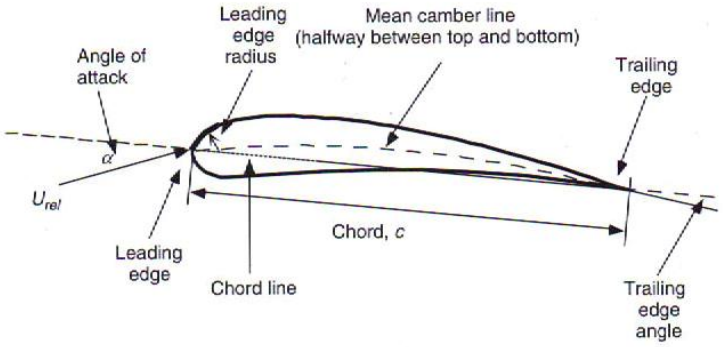

Figure 3.3: Airfoil Nomenclature

Aerodynamic Forces

A fluid flow over an airfoil creates a distribution of pressure and frictional forces. These pressure and frictional forces can be resolved into a lift force, drag force and pitching moment as displayed in the following figure. These resultant forces have been found to act along the chord line at a quarter of its length measured from the leading edge. The lift force is defined to be the force perpendicular to the relative flow direction and the drag force is defined to be parallel to the relative flow direction. Cross sections of rotor blades have airfoil profiles, therefore the lift and drag forces that develop on the blade act a finite distance from the rotor's axis of rotation creating torque. This torque is what causes the rotor spin.

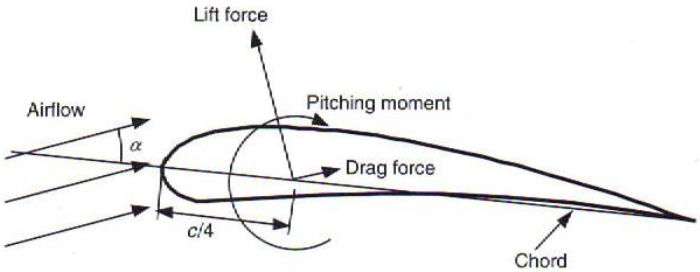

Figure 3.4: Resultant forces and moments on an airfoil section

The lift and drag forces can be numerically defined as

$$F_L = C_L \frac{1}{2} \rho A_p U^2 \text{ and } F_D = C_D \frac{1}{2} \rho A_p U^2$$

where C_L and C_D are the non-dimensional lift and drag coefficients, ρ is the density of the fluid, A_p is the planform area (chord times span) and U is the free stream velocity of the fluid. The lift and drag coefficients are functions of the Reynolds number, defined as the ratio of inertial to viscous forces. The Reynolds number is numerically represented as

$$Re = \frac{UL}{\nu},$$

where U is the water free stream velocity, L is distance traveled (chord length) and ν is the kinematic viscosity of water (μ/ρ). For every Reynolds number there are different flow characteristics around the airfoil resulting in different lift and drag coefficients. This relationship is characterized using experimental data as shown below in Figure 3.5. The figure shows the coefficient of lift versus angle of attack and the coefficient of drag versus angle of attack for a NACA 0012 airfoil at varying Reynolds number.

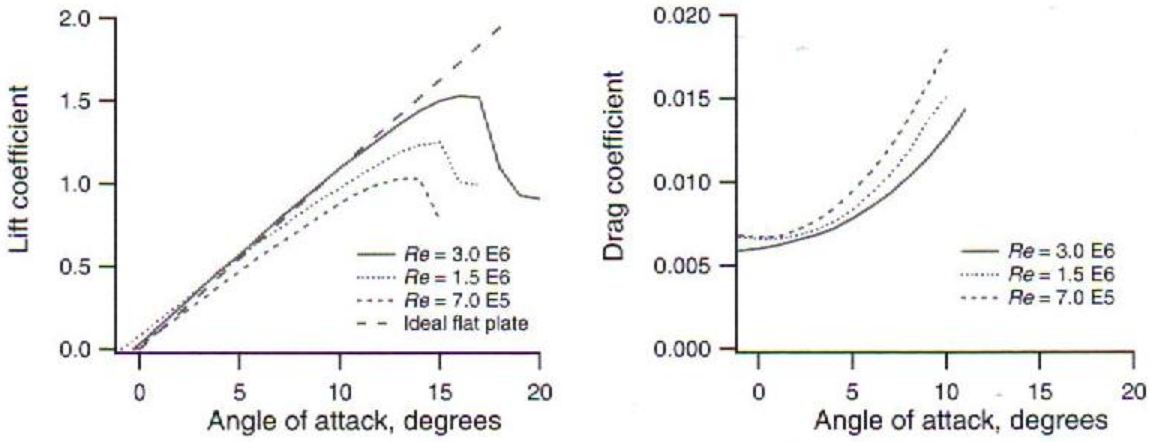

Figure 3.5: Experimental C_L and C_D

The optimal angle of attack can be determined using this experimental data by identifying when the ratio of C_D/C_L is minimum. At this location there will be the greatest lift force and the smallest drag force producing the maximum amount of torque on the rotor.

3.3 – Blade Design

An ideal blade shape was derived using Blade Element Momentum (BEM) theory which is extensively used in the Wind turbine industry. BEM theory is a combination of both momentum theory which is a control volume analysis of forces on the blade and blade element or strip theory which is the analysis of forces at a specific blade section as a function of local blade geometry. Using BEM the optimal blade shape and performance characteristics can be calculated

for each annular section of the blade. The entire shape and performance of the blade can be obtained by summing the values calculated for each annular section.

3.3.1 – Rotor Design Code

A rotor design code was created in Matlab based off of a generalized rotor design procedure presented in Wind Energy Explained (Manwell, 2009). The code begins by allowing the user to define basic turbine parameters and operating conditions. An example of these inputted parameters is presented in Table 3.1 below.

Table 3.1: Input parameters for rotor design code

Radius of Rotor [inch]	30.0
Radius of Hub [inch]	9.0
Number of Blades	6.0
Number of Blade Elements	20
Tip-Speed-Ratio	3.0
Flow Velocity [knots]	6.0
Reynolds Number	125,000

The values in the above table are the chosen parameters and operating conditions used for the design of the final blade shape. The diameter of the turbine rotor was designated to be 5 feet. To increase the direct drive generator efficiency, a 19 inch hub diameter was chosen. Therefore, the blades are designed to be 21 inches in length. Six blades were chosen for the complete rotor based on practical dynamic stability issues and on the tip-speed-ratios expected for a hydrokinetic application. The blades were designed for the largest flow speed expected, 6 knots or roughly 3 m/s. This was done to ensure that the blades would be most efficient when the flow contained the largest amount of kinetic energy allowing the rotor to extract maximum power. A tip-speed-ratio of 3 was chosen so that the rotor would spin at realistic rotational speeds for a marine application.

Once the operating conditions and parameters were inputted, the user then designates a hydrofoil profile for the code to use in design calculations. The user inputs this designation by inputting the name of the foil along with its aerodynamic characteristics, i.e. coefficient of lift and drag versus angle of attack. Once the airfoil profile is chosen and the performance data is inputted, the code then implements BEM theory and derives the optimal blade shape for that profile. BEM theory begins by dividing the blade into a specified amount of annular sections. Our blade was designed using 20 sections which proved to have an effective balance between accuracy and computation time. The derived blade shape is defined by the chord and twist for each blade element. The optimal blade design has an increasingly large chord and twist angle as one approaches the rotor hub.

With the blade shape defined the code then calculates the theoretical rotor performance. The rotor performance is determined by calculating the power coefficient at each annular element. The total power coefficient of the blade is then determined using a sum approximating an integral over the blade. The power coefficient is defined as the ratio of how much usable energy the rotor extracts to how much theoretically available energy is in the

flow. With the shape and performance calculated the code then analyzes the expected lift and drag forces on each blade element. These forces can then be used for a structural analysis of the blade. All these values are outputted in an organized table showing the calculated values for each annular element and the totals for the entire blade. An example of this output is shown in Table 3.2 below.

Using this computer program, multiple traditional airfoils used in the wind turbine industry were run through the design code. The resulting shape, expected forces and overall performance were compared for the different airfoil blade designs. Through the comparison of these traditional airfoils, the most "ideal" profile for our specified operating conditions was chosen based on overall performance and structural integrity of the blade.

3.3.2 – Final Blade Design

From the previously mentioned to analysis of many traditional airfoils, the NACA 44XX series was chosen as the ideal airfoil series for our final blade design. This series was chosen because it had one of the highest power coefficients and because it had by far the smallest deviation of power coefficient with respect to the percent thickness. The high power coefficient was favorable because it increases the potential amount of energy that can be harvested from a flow. The small deviation and predictable trend of blade performance to profile thickness was ideal for a blade design having a varying thickness throughout the blade.

Using the optimal blade shapes derived for five NACA 44XX series airfoils (4412, 4415, 4418, 4421, and 4424) a finite element structural analysis was conducted. This analysis determined the NACA 4421 profile (21% thickness based on chord length) to be an acceptable thickness for the stress that the blade will be experiencing near the hub. The analysis also showed that the stress in the blade decreases as the radius increases, therefore the profile thickness could also decrease while still maintaining an acceptable factor of safety. The conclusion of the structural analysis was to vary the thickness starting at a 4421 for the hub and decreasing to a 4418 and then to a 4415 at the tip.

Due to the increased complexity of varying the thickness along the radii of the blade and due to the minimal decrease in overall power coefficient by keeping a constant thickness, the final blade design was chosen to use a NACA 4421 profile throughout the length of the blade. The greater profile thickness resulted in an overall stronger blade which is advantageous for the large forces experienced in marine environments. Along with this, a minimal decrease in performance was encountered making this the ideal choice for the final blade design.

The final blade shape including angle of twist, chord taper, power coefficient and lift and drag forces is shown below in Table 3.2. The following table shows the output of the rotor design code for the chosen NACA 4421 airfoil and the operating parameters and conditions shown above in Table 3.1.

Table 3.2: Rotor design code output for the final blade shape

Radius [inch]	Chord [inch]	Angle of Relative Flow	Blade Twist Angle	Power Coefficient	Lift Force [lbf]	Drag Force [lbf]
9.8	4.42	30.48	24.48	0.0157	11.70	0.20
11.3	4.24	27.76	21.76	0.0187	13.05	0.23
12.8	4.04	25.41	19.41	0.0216	14.41	0.25
14.3	3.83	23.37	17.37	0.0246	15.77	0.27
15.8	3.63	21.61	15.61	0.0275	17.15	0.30
17.3	3.43	20.07	14.07	0.0303	18.53	0.32
18.8	3.25	18.71	12.71	0.0331	19.92	0.35
20.3	3.08	17.52	11.52	0.0358	21.33	0.37
21.8	2.92	16.46	10.46	0.0383	22.74	0.39
23.3	2.78	15.52	9.52	0.0404	24.15	0.42
24.8	2.64	14.67	8.67	0.0418	25.58	0.44
26.3	2.52	13.90	7.90	0.0417	27.01	0.47
27.8	2.41	13.21	7.21	0.0381	28.44	0.49
29.3	2.30	12.58	6.58	0.0235	29.88	0.52
			Totals →	0.4437	300.00	5.20

Figure 3.6 below contains three different views of the 3D computer model of the blade made using Solidworks. The blade contains approximately18 degrees of twist and 2.12 inches of chord taper and has an overall power coefficient of 0.444.

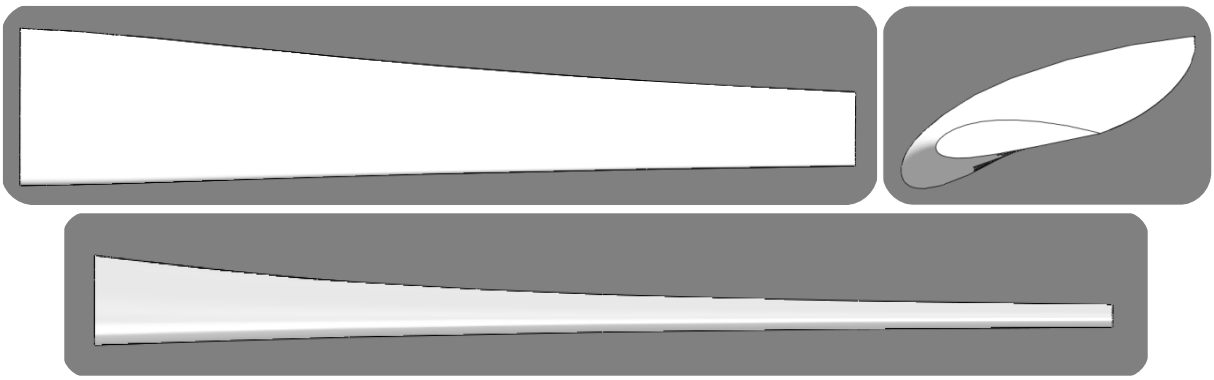

Figure 3.6: CAD model of final blade design

3.3.3 – Complete Rotor Design

The complete rotor was designed to have 6 blades and a diameter of 5 feet. To increase the direct drive generator efficiency a large hub/nacelle diameter was chosen, 19 inches. Therefore, the blades were designed to be 21 inches in length. To help reduce drag and to divert the fluid flow to the blades an elliptical nose cone was chosen. The complete rotor design can be seen in Figure 3.7 below.

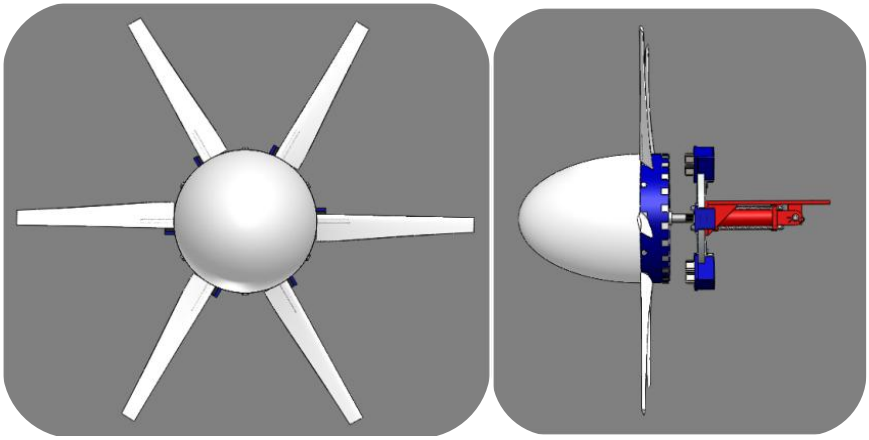

Figure 3.7: CAD model of final rotor design

3.4 – Manufacturing

3.4.1 – Blades

The blades proved to be difficult to manufacture do to the complexity of the derived blade shape. Not only does the blade twist and taper it is relatively thin, therefore further complicating the manufacturing and attachment. To achieve the best performance out of the blade, it was essential to manufacture the blades as close to our derived shape as possible. In addition to this, it was also important to make sure the leading edge of the blade was kept as smooth as possible to stay true to the airfoil characteristics.

Although there was a decrease in strength from the initial desired aluminum, the blades were cast using an ABS plastic. A blank of the blade shape was made on a rapid prototype printer, which was able to quickly and cheaply produce a prototype of the exact blade shape that was designed in CAD. This prototype was then used as a blank to create a fiberglass mold. Once the mold was made to the exact shape, six blades were cast with the engineering plastic. These blades are depicted below in Figure 3.8. This manufacturing process allowed each blade to be made quickly and with an identical shape. This also kept manufacturing cost much less than machining an aluminum blade on a 5-axis CNC machine would have been. To help increase the structural rigidity of the blades, they were coated with two layers of epoxy resin and 4 mil fiberglass cloth. This strengthened the blades greatly decreasing their deflection while still maintaining the original shape of the blades.

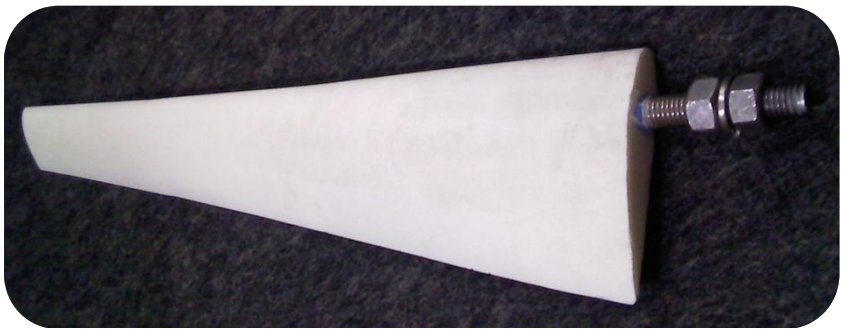

Figure 3.8: ABS plastic blade with mounting shaft

The blades were cast with a piece of ½”- 13 threaded rod inside them as seen in the above figure. This rod was positioned at exactly quarter chord, which is where the resultant forces act. The threaded rod went 7 inches into the base of the blade and had holes drilled in it. This allowed the ABS plastic to cure around and through the shaft firmly holding it in place. The threaded rod stuck out the bottom of the blade an additional 2.5 inches, so that the blades could be threaded into a central rotor hub. This attachment is shown below in Figure 3.9. The rotor hub is 1 inch thick and has 6 circumferentially tapped holes for the blade attachments. This attachment method allows the blades to be continuous adjusted to any desired angle of attack. The blades held from rotating using two lock nuts.

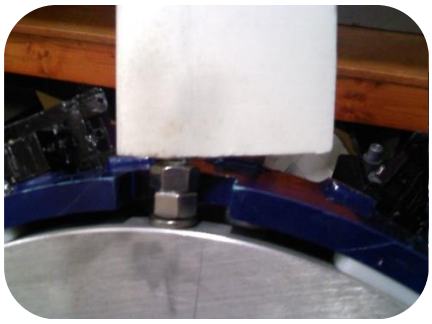

Figure 3.9: Blade attachment to rotor hub

3.4.2 – Nose Cone

The nose cone was made out of buoyancy foam. Not only is this a suitable material for a marine environment it will also help counteract the overall weight of the turbine. Three pieces of foam were adhered together to create a square cube. Then using a lathe, the square billet was turned down into a perfect half ellipse with a ratio of 2 (Length/Diameter). The resulting elliptical nose cone is shown below in Figure 3.10. A ¾ inch copper tube was then sent through the center of the ellipse. The nose cone will be mounted to the hub by sliding the nose cone and copper pipe over a length of threaded rod coming off the front of the rotor. The nose cone will be held up against the rotor plate using two jam nuts. To create a smooth and firm surface on the nose cone it was painted with two coats of waterproof latex paint.

Figure 3.10: Foam elliptical nose cone

4 – Generator

4.1 – Introduction

The generator is the device that converts the rotational shaft work from the rotor into electricity. A generator plays an extremely important role in hydrokinetics because it converts the rotational shaft energy into electrical energy which can be easily and quickly transported above water for use in any location. VFG generators have a relatively simple design yet are very effective. The general VFG design consists of a ring of permanent magnets that can move axial into a ring of yokes. The yokes are U-shaped and are wound with transformer wire creating a coil. As the magnets rotate through the yokes they induce an electrical current in the coils.

4.2 – Theory

Magnets create an invisible "magnetic field" by permanently aligning the atoms inside the magnet. This arrangement forms magnetic poles which make a magnet attract or repel other dissimilarly/similarly arranged objects.

"Magnetic flux" is the term used to describe the quantity of magnetism flowing through and leaving a magnet's poles. The flux of a magnet can be imagined as flowing out one pole and returning at the other pole in a circular pattern as seen below in Figure 4.1. Near the poles where the lines converge, the magnetic field and force is the largest. The magnetic field and force are weaker away from the poles as the lines are dispersed.

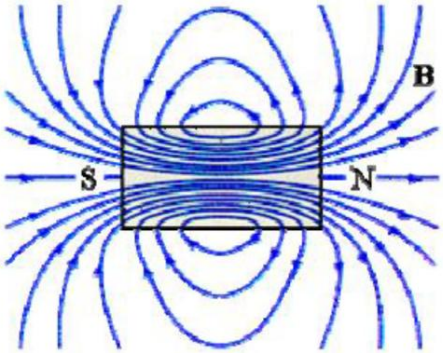

Figure 4.1: Magnetic flux lines of a permanent magnet

In a generator, a rotating ring of magnets normally spins within a stationary set of conductive cores (yokes) that are wound with wire (coils). A number of coils assembled together are called a stator. As the magnet ring spins, the magnetic flux of the magnets is captured in the yoke. As the magnetic flux flows through the yoke it induces a current within the coils. This phenomenon is pictorially shown in Figure 4.2 below.

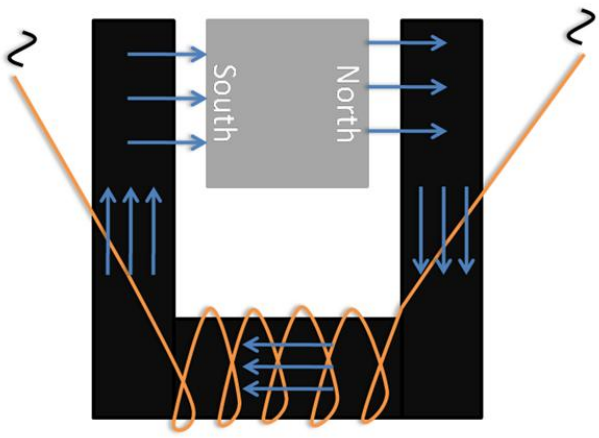

Figure 4.2: General schematic of a generator; magnet, yoke and coil.

In order to increase the effectiveness of a generator it is important to alternate the exposed magnetic poles in the magnet ring. If the magnets all shared the same exposed poles, they would essentially magnetize the yokes. If this happens, the ability of the stator to produce power is greatly compromised. Instead, if the magnetic poles are alternating, the stator yokes will never become magnetized, and the rotating magnetic field will produce a consistent AC voltage and current. In addition to this, since the permanent magnets generate a constant magnetic flux field, the stator output voltage and current vary directly with the rotational speed of the generator.

4.3 – Design Improvements

The main areas of consideration within the design of the generator are the concentric alignment of the permanent magnets, yokes design, and the method of isolating the coils power output from dissipation to the surrounding environment. An important stage in the design of the generator was applying the recommendations of the first generation group in order to successfully increase the power output and efficiency of the generator.

To increase both the overall power output and efficiency of the direct drive generator a 19 inch magnet ring diameter chosen. This is roughly double the diameter of the first generation. The larger the magnet ring diameter, the greater the tangential velocity of the magnets which creates an increase in magnetic flux through the yokes therefore inducing a larger electrical current in the coils. This larger electrical current produces a greater power output.

The increase in diameter also provided space for twice the number of stator yoke/coil assemblies compared to the first generation. The chosen design utilizes six yokes which will alone double the potential power output of the generator. The increase in magnet ring diameter also created room for an increase in the number of magnets. The ratio of the magnets to generator yokes is important to the operational efficiency of the generator. The ratio must allow each coil to align with a magnet of the same orientation. Therefore each yoke is experiencing the same pole at the same time creating a single phase AC output. The magnet ring was chosen to contain 24 permanent magnets, double the amount in last year's design.

4.4 – Manufacturing

4.4.1 – Magnet ring

The magnet ring is made up of 24 Neodymium N42 1 inch cube magnets purchased from Applied Magnets. Neodymium magnets are a rare earth magnet with the strongest magnetic properties of any material currently in use. Neodymium's high strength and compact size make them a desirable choice for our design. Each permanent magnet has 114 pounds of pull force. The high magnetic strength creates large amounts of magnetic flux in the yokes which produces more power per magnet than that of a weaker magnet.

A drawback of the first generation's magnet ring design was its inability to reliably secure the magnets in a concentric circle. Due to the magnets physical properties they cannot be machined or altered; therefore the magnet cubes had to be secured in a mechanical way. Our magnet ring used a 4 inch section of 19 inch diameter PVC piping. Notches were machined around the radius of the pipe to hold the 24 magnet cubes into place, as seen below.

Figure 4.4: Notches machined in PVC ring

These notches were made slightly smaller than the magnet size so that the magnets would be firmly held in place. All magnets were positioned perfectly concentric around the ring using a spacing tool. The poles of the magnets were aligned using a special magnet flux paper shown below in Figure 4.4. A two part epoxy adhesive was also used to add extra support ensuring the magnets stayed in place for the lifetime of the turbine. The magnet ring was then affixed to the rotor hub which can be seen in the following figure.

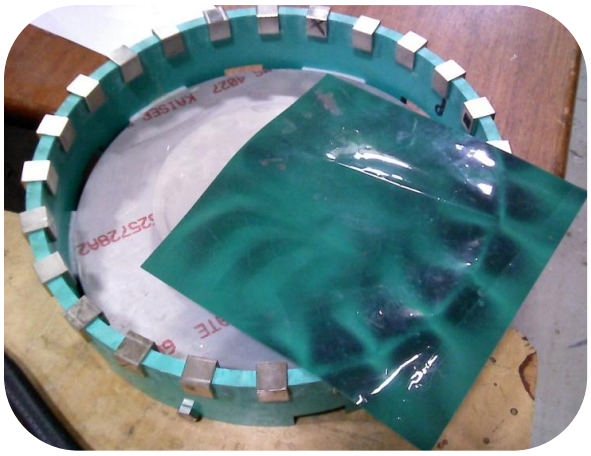

Figure 4.4: Fully assembled magnet ring with magnetic flux paper

4.4.2 – Yokes and coils

The first generation used pre-manufactured U-shaped Ferroxcube yokes. These yokes were chosen because of their high permeability making them much less likely to be saturated by the large magnetic flux. However, a problem faced with this yoke design was the gap tolerances between the magnets and yokes. As the air gap increases, the amount of magnetic flux being captured in the yoke decreases which results in a decrease in electrical output. The Ferroxcube yokes were not able to be machined or altered to change this gap because of the material's physical properties.

The chosen design of the new generator assembly incorporated a laminate yoke design instead of a solid material. The laminations of the yoke were cut from 1/16" steal sheet metal. Each piece was cut in a U-shape as shown in the following figure.

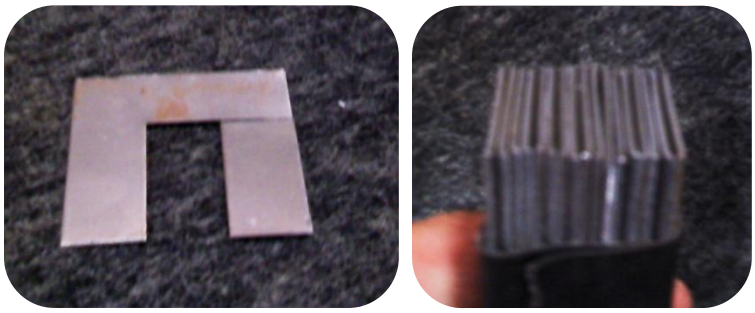

Figure 4.5: U-shaped yoke layer and complete laminate stack

By stacking 17 laminations up a 1 inch thick yoke was formed as shown above. This design had many benefits that proved advantageous to the generator's efficiency. First, the steel laminate yoke was machinable allowing us to precisely adjust the air gap tolerance. In addition to this, the laminate design has also been proven to help increase the magnetic flux flow in the yoke.

In order to form the yoke, an assembly jig was made to ensure each yoke was formed identically. The assembly jig allowed for the laminations to be pressed together tightly while holes for bolts could be drilled with consistent positioning. Six bolts were positioned along the two vertical sections of the yokes ensured the laminations would remain in position. Once complete the, yokes were wound with 18 gauge insulated transformer wire. Each yoke was wound with 300 turns of wire creating a coil able to capture significant electrical current. A wound wire coil is shown below in Figure 4.6.

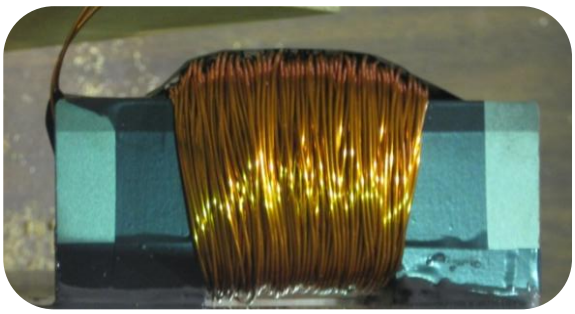

Figure 4.6: Wire coil comprising of 300 turns of 18 gauge wire

Precautions were taken to ensure that power was not lost to the surrounding environment, i.e. dissipated as heat in the stator plate. The solution to this possible problem was to pod the generator coils. To do so, the generator coils were positioned in a plastic electrical housing box and filled with short strand fiberglass body filler. The pods can be seen below in Figure 4.7. This potting technique isolated the electrical coils making sure that the magnet flux remains in the yokes and coils. This technique also protects the yokes and coils from the harsh marine environment, allowing then to have a longer lifetime.

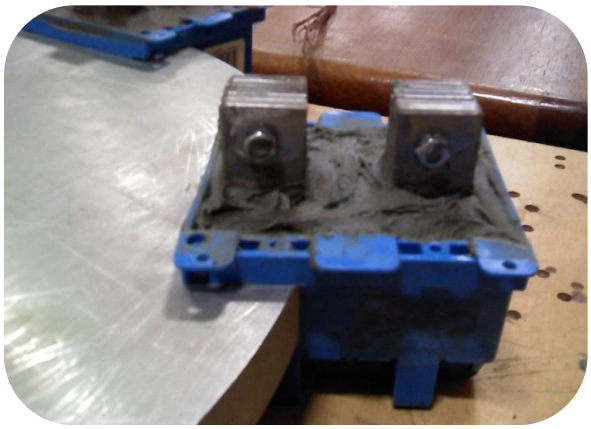

Figure 4.7: Potted yoke and coil assembly

Each pod was precisely mounted to the stator plate. The pods were affixed using aluminum angle iron mounting brackets. Each mounting bracket was slotted allowing the entire pod to move axially. This permitted us to position the yokes to have equal air gaps on both sides of the magnet ring. A picture of how these pods are mounted is shown below.

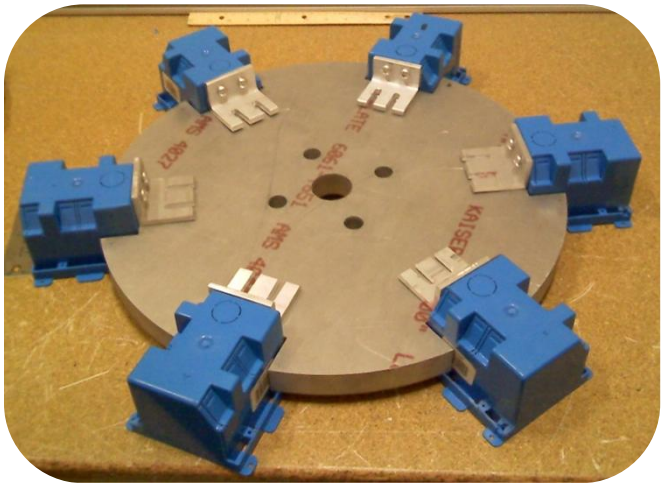

Figure 4.8: Attachment of pods to stator plate

5 – Actuation

5.1 – Introduction

Actuation of the magnet rotor ring relative to the stator coils is an essential component of the VFG generator design. Ideally for long term deployment of a hydrokinetic turbine with Variable Flux Generation, this actuation would be achieved using a passive actuation system. A passive system would automatically engage the rotor relative to the stator solely based on hydrodynamic drag exerted by the tidal current. As the velocity increased the magnet ring would be engaged further into the yokes generating more power and as the velocity decreased the magnet ring would recede back out.

5.2 – Alternative Designs

5.2.1 – Passive Mechanical

In order to control the actuation autonomously a spring and damper could be used to govern the axial displacement between the yolks and magnets. An example of this possible system is shown below in Figure 5.1. A spring alone would be insufficient because of the strong magnetic pull force that occurs when the magnets begin to become engaged in the yolks. Combining the damper with the spring would dissipate the large magnetic attraction force. Therefore the axial engagement with a spring damper system would vary depending on the hydrodynamic drag force present.

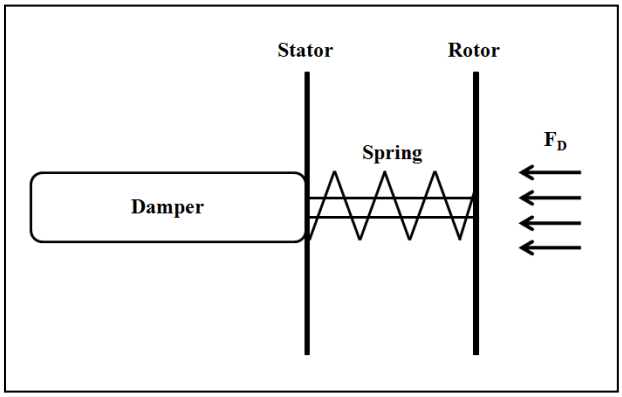

Figure 5.1: Schematic of passive mechanical system

5.2.2 – Passive Electrical Actuation

The blades of the turbine were engineered to perform optimally when spun at a specific rotational speed. This rotational speed will change depending on the flow velocity as well as the magnet yoke engagement. A system could therefore be designed to measure the rotational speed, processes the signal with an electronic controller and output a signal to an actuation system which would move the rotor and magnet ring axially with respect to the stator and yokes. An example of this possible design is represented in Figure 5.2. As the flow velocity increases the RPM will increase which will cause the controller to tell the actuator to engage the magnets further. This will increase the magnetic resistance on the rotor decrease the RPM back to the desired level.

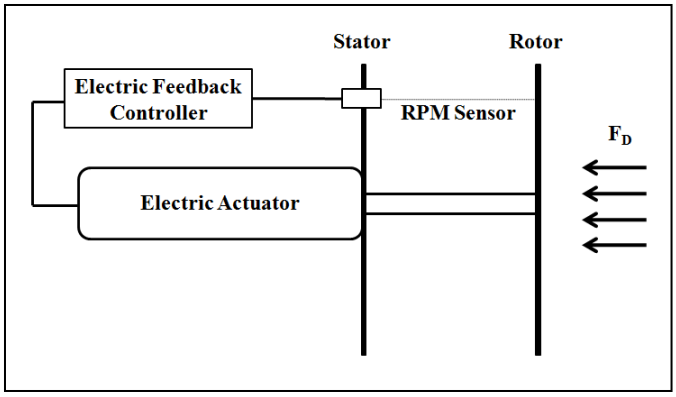

Figure 5.2: Schematic of passive electrical system

5.2.3 – Manual Hydraulic System

A manual system could also be used position the rotor incrementally based on the rotor speed and power output. One possible manual system could use hydraulics as shown by the schematic in Figure 5.3. A hydraulic system uses a small diameter rod at high fluid pressures to produce large pull and push forces. These systems are controlled manually, and can be adjusted to move in specific increments which would allow for more data to be taken at desired locations.

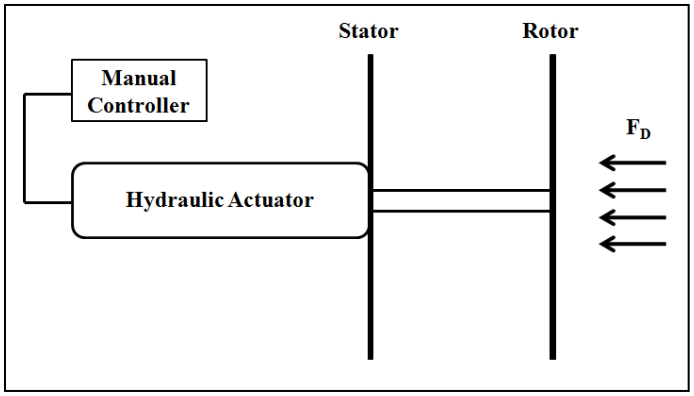

Figure 5.3: Schematic of manual hydraulic system

5.3 – Chosen Design

Passive control systems are optimal for long term deployment however they involve very complex designs. To accurately design a passive system there must be data on drag and magnetic forces encountered as well as rotational speed and power output at various engagements. With this data a system could be designed to accurately control the magnet ring engagement; however, there would still be a very lengthy calibration period to ensure the device is operating properly.

For these reasons, a manual hydraulic system was chosen for the final design. The hydraulic system was the favorable choice because it was a reliable way to control actuation and because it will allow us to precisely control the engagement for testing purposes. Considering our goal was to design a more powerful, reliable and efficient turbine it was necessary to have an actuation system that could be manually controlled allowing us to get a more comprehensive and

repeatable set of experimental data. This data could then be used in future generations, to help design a passive system.

The manual hydraulic system is composed of a power unit, controller, and hydraulic cylinder. The hydraulic cylinder, tubing line and power unit were all designed to withstand the worse case hydrodynamic drag forces that could be encountered by the rotor. The cylinder face was designed to be mounted to the stationary stator plate and the end of the cylinder shaft to mount to the rotor hub. Therefore, as the hydraulic cylinder actuates the rotor and magnet ring will be moved axial with respect to the stator and yokes. A controller was designed to allow small incremental movements of the cylinder in both directions. It was also designed to allow continuous movement when quick axial movement was desired. This controller allows the engagement of the rotor to be accurately positioned.

5.4 – Manufacturing

5.4.1 – Cylinder

The hydrodynamic drag force acting on the turbine was calculated to be 2,400 lbs for an approximated 5 foot diameter solid disk. Using this value, hydraulic cylinder calculations were performed that quantified the required fluid flow rates, push/pull force ranges for each shaft diameter, and operating pressures. It was desired to have the cylinder stroke long enough to fully disengage the magnets from the yokes. Also, to make attachment to the rotor hub easier the cylinder was chosen to have the end of its shaft threaded. Lastly, a tie rod cylinder was the chosen type because it allowed for easy mounting to the stator plate. The chosen hydraulic cylinder has a 3 inch cylinder bore, a 1.25 inch diameter shaft, a 6 inch axial stroke and a maximum operating pressure of 3,000 psi. The hydraulic cylinder is shown in the following figure mounted to the mounting bracket. The mounting bracket gets bolted to the deployment structure and holds the stator plate.

Figure 5.4: Hydraulic cylinder pictured with mounting bracket

5.4.2 – Controller

The controller operates the solenoid valves and fluid pumps in the power unit which are used to extend or retract the hydraulic cylinder. The custom designed controller was a culmination of electrical relays which were programmed to allow the hydraulic cylinder to move in

specific increments. The relays achieved this by controlling the amount of time the electrical circuit was connected for the solenoids. Because this controller is set to move the cylinder a specific increment each time, the axial position of the rotor can be determined solely by the number of times the button was pushed.

5.4.3 –Power Unit

The function of the power unit is to house a reservoir of hydraulic fluid and to provide the force to pressurize two hydraulic lines which are attached to the hydraulic cylinder. For the VFG application the power unit had to be double operating as opposed to single operating. This means it is capable of providing pressure in both hydraulic lines to sustain either pushing or pulling forces. It does this by the means of solenoids which use 12 volt direct current power from a battery to pressurize the hydraulic fluid up to 2,000 pounds per square inch at a rate of 1.35 gallons per minute. The maximum pressure rating and flow rate were two parameters sized based on the forces we expected to see on the hydraulic cylinder (see Appendix B). The purchase power unit, controller and 12 volt battery are shown below in Figure 5.5.

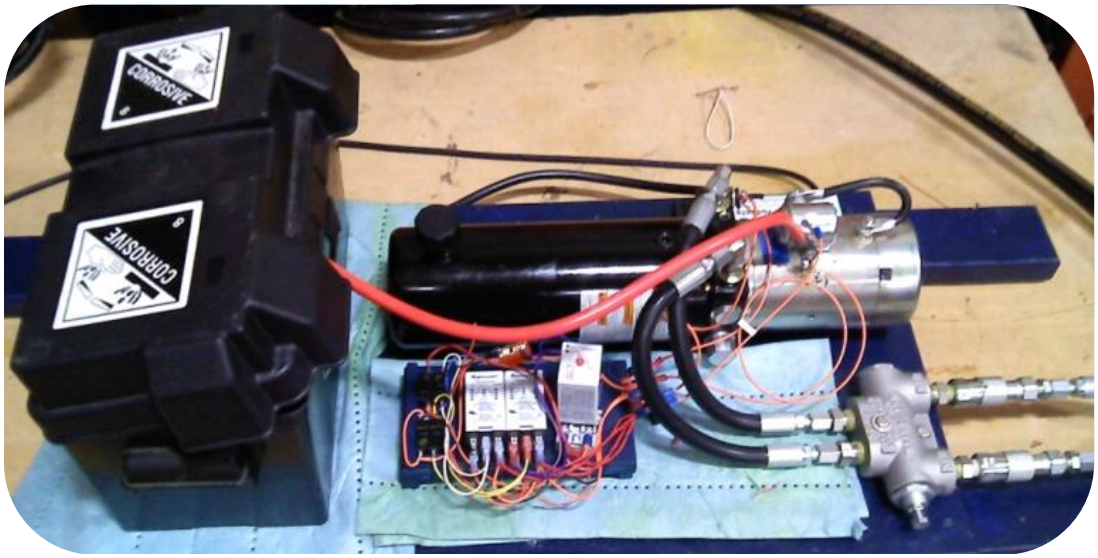

Figure 5.5: Hydraulic power unit pictured with battery and controller

6 – Structure

6.1 – Introduction

The turbine structure is an assembly of three main components; the rotor hub, stator plate, and mounting bracket. The mounting brackets main function is to connect the turbine to the deployment structure. It is also designed to add extra support for the hydraulic cylinder. The function of the rotor hub is to be a rotating plate on which the blades, magnet ring, and nose cone can be mounted. Lastly, the stator plate is designed to hold the yokes, mounting bracket and hydraulic cylinder in place. Altogether these components make up the turbine structure.

6.2 – Design of Components

6.2.1 – Mounting Bracket

A structure needed to be designed that was capable of attaching to the deployment structure positioned above it and to the stator plate in front of it. The deployment structure was designed to bolt to the bottom of the deployment structure using 8 bolts sized to withstand the shearing force. The stator plate was designed to support the hydraulic cylinder. To achieve this, a 5-hole pattern was machined into the front plate allowing the cylinder shaft and four tie rods to go through. These 4 tie rods hold the cylinder to the mounting bracket and are used to mount the mounting bracket to the stator plate. The design of the mounting can be shown below in Figure 6.1.

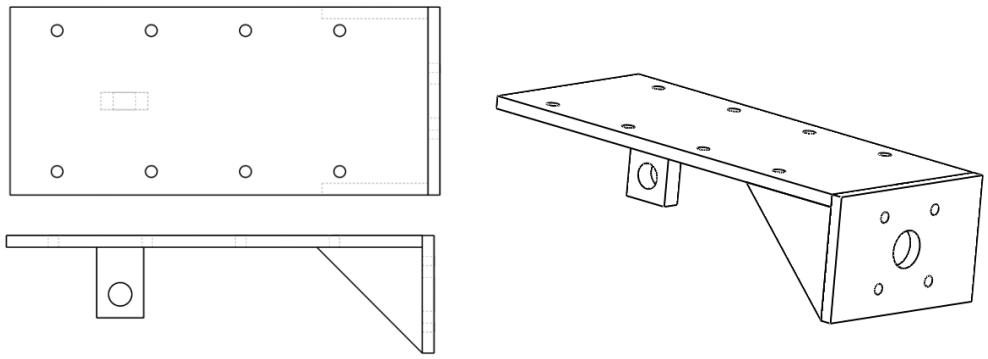

Figure 6.1: CAD drawings of the mounting bracket

6.2.2 – Rotor Hub

The rotor hub is designed to incorporate the turbine blades, nose cone, and hydraulic cylinder shaft. On the perimeter of the hub are 12 evenly space tapped holes. Six of these holes are used to attach the blades and the remaining six holes are used to attach the PVC magnet ring. Bearings are used to decouple the rotational motion of the rotor. With the rotation decoupled a threaded rod is positioned centrally on the hub and extends out. The nose cone is then slid on and fastened to this rod. CAD wireframe schematics of the rotor hub can be seen in Figure 6.2.

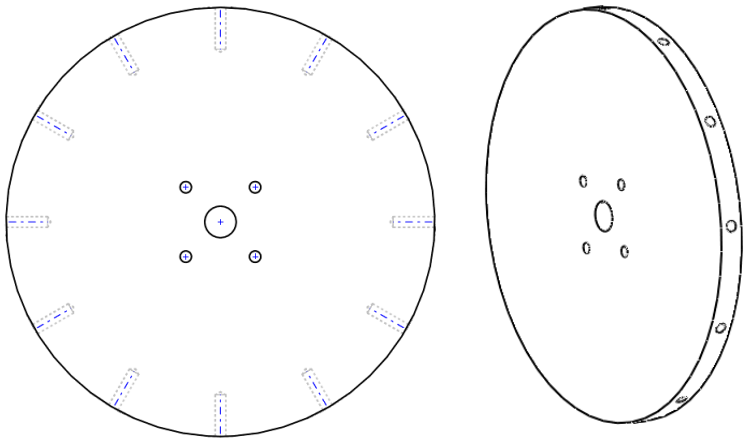

Figure 6.2: CAD drawings of the rotor hub

6.2.3 – Stator Plate

The stator is designed to be a stationary plate on which the yolks and their pod housings can be attached. Notches are positioned concentrically around the stator to help align the pods. The pods are secured to the stator plate using slotted aluminum brackets and tapped holes. The plate is designed with the same 5-hole configuration as the mounting bracket. Therefore the mounting bracket and hydraulic cylinder can be attached easily. This whole pattern also allows the cylinder shaft to be centrally located on the stator plate. This plate was also designed to mount the optical RPM sensor and the torque measurement infrastructure. Figure 6.3 below shows two views of the designed stator plate.

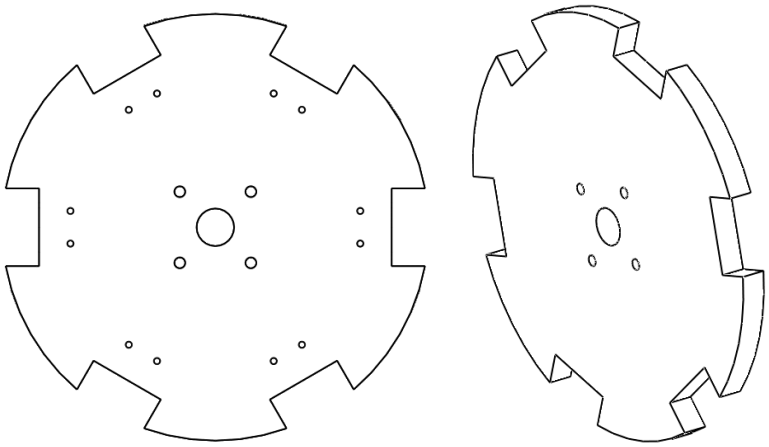

Figure 6.3: CAD drawings of the stator plate

6.3 – Manufacturing

6.3.1 – Mounting Bracket

Two steel plates put at a 90 degree angle to another were welded together to form an L-shape. That structure was reinforced with a triangular supports welded between them. The

top plate had 8 holes drilled in it. These holes match the hole configuration on the deployment structure and will be used for mounting. The front plate has a 5-hole configuration machined in it for the cylinder tie rods and shaft. For added strength and support for the hydraulic cylinder a small steel plate with a hole thru it was positioned and welded to the upper plate. This plate was used to pin the end of the hydraulic cylinder in place. The plate was manufactured out of A-36 hot rolled steel. All components were welded together as shown in Figure 6.4. Once the entire structure fabricated it was coated with Rustoleum primmer and then two coats of Rustoleum paint to prevent corrosion.

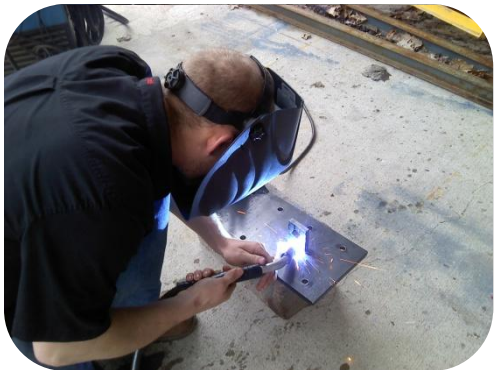

Figure 6.4: Welding of mounting bracket

6.3.2 – Rotor Hub and Stator Plate

The circular shape and five holes patterns in both the rotor hub and stator plate were water-jet cut out of 1 inch thick pieces of 6061 Aluminum plate. Along the perimeter of the rotor hub twelve holes were drilled and tapped using a rotary table and a milling machine. For the stator plate, two small ¼”-20 holes were drilled and tapped at the base of each notch to allow for the attachment of the pods. Photos of the fabricated stator and rotor plates are shown below in the following two figures.

Figure 6.5: Aluminum rotor hub with magnet ring attached

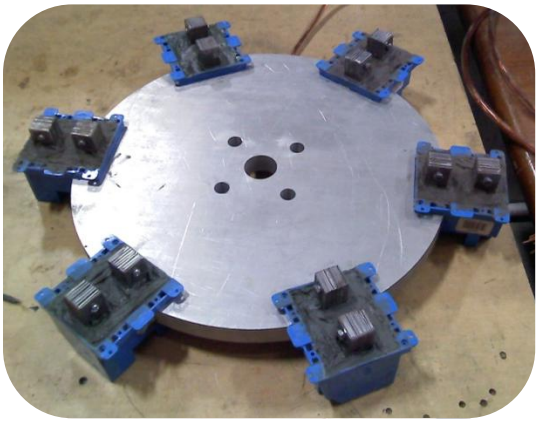

Figure 6.6: Aluminum stator plate with pods attached

7 – Performance Testing and Results

Multiple tests need to be performed to determine the overall performance and efficiency of the turbine. These tests include: bench-top generator tests, rotor torque measurements, overall performance tests. These three tests can be used to quantify the generator efficiency, rotor efficiency and overall efficiency independently.

7.1 – Bench-top Generator Tests

For the generator bench-top test, the rotor/magnet ring was spun at various rotational speeds based on the expected tip speed ratios and current velocities in tidal flows. The magnet ring was engaged into the stator coils at small increments and the power output was measured. Therefore, at each rotational speed the power output versus axial engagement was determined.

The rotor/magnet ring was spun using a high torque hand drill as shown below in Figure 7.1. The hand drill was plugged into a variac which allowed us to control the power input to the drill. By controlling the power input of the drill we were able to accurately control the rotational speed (RPM). The magnet ring was engaged incrementally using the hydraulic cylinder and the custom designed controller. The axial distance of the magnets after each increment was measured using a string and a ruler. The RPM was measured at each increment using an optical laser tachometer. The power was dissipated using a resistive load bank shown in the background of Figure 7.1.The power output was measured and recorded using digital multi-meters. To achieve maximum power, the resistive load was varied until the maximum current was outputted. The resistance was then measure and held fixed throughout the tests. At each increment the current and voltage were recorded. The power output was calculated using $P = I^2R$, where P is the power output, I is the current and R is the resistive load.

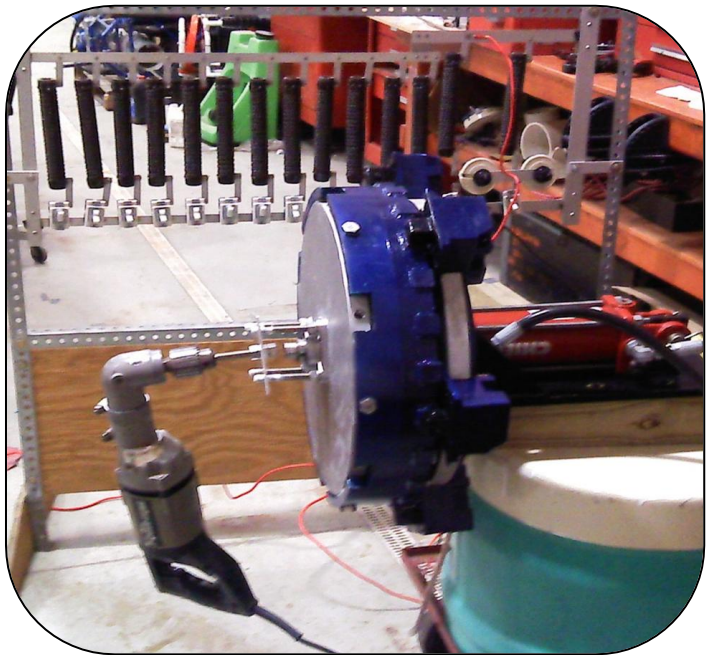

Figure 7.1: Generator bench-top test experimental setup

Preliminary baseline generator tests have been run for three rotational speeds; 100, 110 and 120 RPM. These rotational speeds correspond to the designed tip-speed-ratio of 3 and current velocities of 2.75, 3, and 3.25 m/s respectively. The power output per axial engagement curve for one yoke/coil assembly is shown below in Figure 7.2. Only one yoke was tested due to power dissipation concerns. From these preliminary tests, the one yoke was able to output a maximum current of 3.9 amps over a 7 ohm resistive load. This corresponds to a power output of around 110 Watts. Although 110 watts for one yoke seems low, if all six of these yokes are wired in parallel their current adds. Considering the power output is the square of the current, the power output will greatly increase when all six yokes are tested. Based on the 3.9 amp out of one yoke, a conservative estimate of total current for all six yokes in parallel would be around 20 amps. If the generator can output around 20 amps for a rotational speed of 120 RPM then the generator will be able to output over 2,500 watts of power or 2.5 kilowatts.

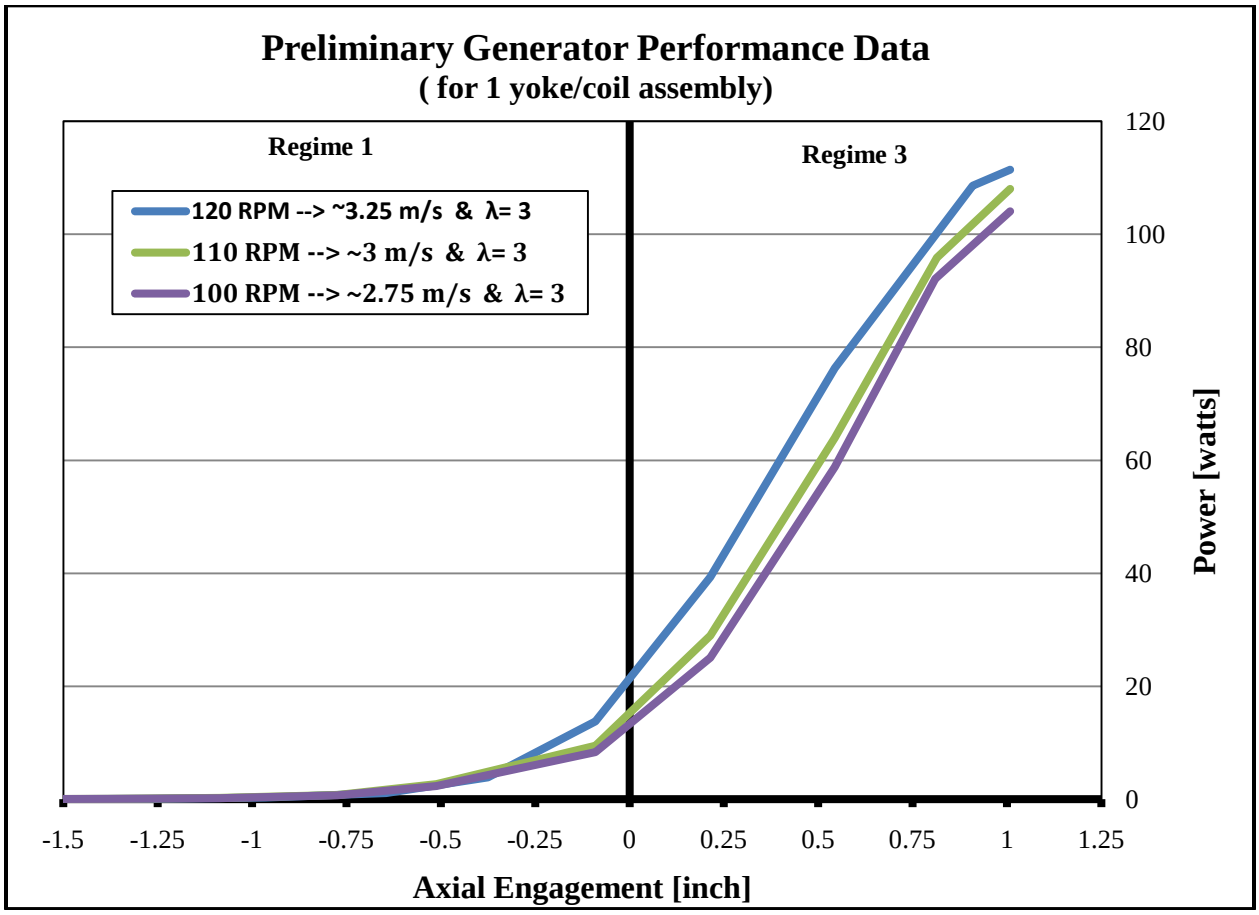

Figure 7.2: Preliminary data for generator bench-top test

7.2 – Rotor Torque Measurement

While the turbine is fully deployed, the barge will be towed at various speeds simulating current velocities. With the generator fully disengaged, a mechanical braking force will be applied to the rotor. As the braking force is being applied the tangential force that is induced on the brake will

be measure along with the change in RPM. This measured torque and change in rotational speed can then be used to find the power coefficient of the rotor.

The turbine will be mounted to the deployment structure which is secured to the test barge. The test barge will be hip towed by another vessel. The barge will be towed at set speeds which will correspond to expected current velocities that our hydrokinetic turbine may see. During the torque testing the rotor will be fully disengaged from the stator so that no magnetic forces interact with the rotor allowing it to spin freely.

Mounted to the rotor plate is a circular disk and mounted to that disk is a bicycle disk brake. The disk brake is mounted to an arm that has the freedom to rotate about the center shaft. Attached to the brake is a force transducer which will be used to measure tangential force on the brake. A CAD model of this setup is shown below in Figure 7.3. In this figure the brake is shown in blue and the force transducer is represented as the white S-shaped object.

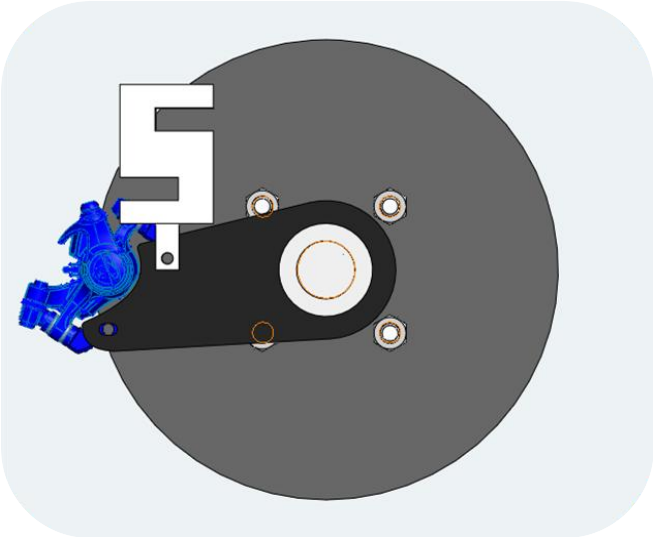

Figure 7.3: CAD schematic of torque measuring infrastructure

As the brake is applied with the rotor spinning freely, frictional resistance will cause it to try to rotate. As the brake attempts to rotate it will be held in place by the force transducer. This will apply a tensile force on the force transducer which will be measured. Knowing this tangential force and the moment arm that the braking force is applied the torque can be determined.

Along with this, as the braking force is being applied the RPM will be continuously measured. This will allow the change in rotational speed to be determined. Using these values the power coefficient of the rotor can be determined from the following equation

$$C_P = \frac{2T\omega}{\rho A U^3},$$

where C_P is the power coefficient of the turbine rotor, U is the current velocity, A is the swept area of the rotor, ρ is the density of water, T is measured torque and ω is the angular velocity of the rotor. The power coefficient will determine how efficient the rotor is.

7.3 – Overall Turbine Performance

Lastly, while the turbine is fully deployed, the barge will again be hip towed at various speeds simulating realistic current velocities. At each speed the total power output of the generator will be measured in the same manner as it was during the bench-top generator test, using a resistive load bank and multi-meters. For each speed the generated will be incrementally engaged. At each engagement the RPM will be measured along with the current and voltage output. Using the measure current and the resistive load the total power output will be determined. This power output data at certain engagements and at certain RPM will be compared to the total theoretical power and the efficiency of the entire turbine can be found.

Full deployment in open water is planned for May 2011. At this time data will be collected for both the torque measurement and overall performance. From this data the rotor performance, generator performance and overall performance of the turbine can be benchmarked.

8 – Budget

The total cost to manufacture the VFG turbine was $3,642.69. Including the cost of the instrumentation purchased for performance measurement the total cost was $4,501.52. The expenditures are broken down by turbine component and item and are shown below in Table 8.1.

Table 8.1: Budget Breakdown

Component	Part	Quantity	Company	Cost
Actuation	12V Hydraulic Power Unit	1	MSC Industrial Supply	541.01
	Custom Relay Controller	1		90
	6" Stroke Hydraulic Cylinder	1	Bailey	109.00
	3/8" Hydraulic Tubing 40'	1		277.00
	Safety Lock Valve	1	Northern Tool + Equipment	79.99
	6' 18-8 SS Threaded Rod 7/16"-14	1	McMaster-Carr	18.81
			Sub-Total -->	**1115.81**
Generator	1/16" Steel U-Shaped Plate	100	Custom Welding Inc	350.00
	Neodymium N42 1" Cube Magnets	28	Applied Magnets	124.04
	Magnetic Wire 1400'	1	McMaster-Carr	112.31
	Pods	6	Home Depot	12.96
	Fiberglass Epoxy Body Filler	3	Home Depot	41.91
	3/8" Clear Tubing 20'	1	Home Depot	14.04
	Plastic Epoxy for magnets	4	Home Depot	21.88
			Sub-Total -->	**677.14**
Blades	Blade Blank	1	UNH Rapid Prototype	130.00
	Blades	6	Salty Boats	700.00
	3' 18-8 SS Threaded Rod 1/2"-13	1	Home Depot	13.97
	Plastic Epoxy for Blades	1	Home Depot	5.96
			Sub-Total -->	**849.93**
Structure	18"x18"x1" 6061 Aluminum Plate	2	McMaster-Carr	469.00
	Nickel-Plated Cast Iron Bearings	2	McMaster-Carr	79.48
	2" 303 SS Round Stock 1'	1	McMaster-Carr	60.19
	Hot Rolled A36 Steel Plate	4	Yarde Metals	130.45
	3/4" copper tube 2'	1	Aubuchon	5.69
			Sub-Total -->	**744.81**
Instrumentation	ACT-1B Tachometer	1	Monarch Instruments	398.10
	ROLS-W Remote Optical Laser	1	Monarch Instruments	168.30
	5' Waterproof Reflective Tape	1	Monarch Instruments	14.40
	Disk Brake	1	Bicycle Bob's Outlet	50
	12"x12" 304 Stainless Steel Plate	1	McMaster-Carr	18.05
	Brake Handle	1	Bicycle Bob's Outlet	20
	Brake Cable and Housing 10'	1	Bicycle Bob's Outlet	30
			Sub-Total -->	**698.85**

Machining	Stator Plate	1	McMaster-Carr	120.00
	Rotor Plate	1	McMaster-Carr	100.00
	Welding for Mounting Bracket	1	Custom Welding Inc	35.00
			Sub-Total -->	**255.00**
Fasteners and Adhesives	18-8 SS Hex Nut 7/16"-14	50	McMaster-Carr	9.49
	316 SS Split Lock Washer 7/16"	25	McMaster-Carr	7.42
	18-8 SS Threaded Rod 7/16"-14 3'	1	McMaster-Carr	9.41
	15/16" O-ring	2	Home Depot	1.82
	1-1/2" 10-24 Machine Screw	50	Home Depot	6.15
	White Paint 1 gallon	1	Home Depot	27.44
	Blue Spray Paint	1	Home Depot	4.48
			Sub-Total -->	**66.21**
			Total Shipping Charges -->	**93.77**
			Total -->	**3642.69**
			Total w/ Instrumentation-->	**4501.52**

9 – Conclusion

As a result of an entire academic year of work, a new and improved hydrokinetic turbine featuring Variable Flux Generation has been design, fabricated and assembled. Many months at the start of the year were devoted to using Blade Element Momentum theory to derive an optimal rotor blade design. As a result from this an ideal blade shape having twist and taper was designed. This optimal blade design yields a high power coefficient increasing the total potential energy extraction from the flow.

Also during the early months a lot of research went into different passive and mechanical actuation systems. Multiple different systems were extensively researched and designed until the most practical and feasible design was chosen. A manual hydraulic system was picked to control the rotor engagement. This system allowed for precise and repeated axial engagements which proved beneficial for testing purposes.

During the middle of the year, time was spent finalized the turbine and generator designs as well as running various analyzes and preliminary tests on certain purchased components. The latter half of the year has been greatly focused on the fabrication of the turbine. Many of the components were machined and modified in house and various different materials and products were used to help keep manufacturing costs low. In the past month or so, with the turbine almost completely fabricated, a lot of time and effort has been spent at developing and building the testing infrastructure. In addition to this some preliminary performance tests have been run and the turbine is ready for open water deployment.

The objectives of the project were accomplished. The new second generation turbine was designed and developed to have a much larger power output, project 2.5 kilowatts. The turbine was designed with a new more efficient rotor and generator. And lastly, the turbine was built robust and corrosion resistant to endure marine open water deployment.

10 – Future Work

Do to time constraints; the amount of performance data originally hoped for was not accomplished. Therefore, more time should be spent on performance testing of the current turbine design. This data could be used not only to accurately benchmark the efficiency and performance of this turbine design but also to give more insight into what specific aspects of the design could benefit from adjustments or redesigns.

This generation's turbine was designed with future generations in mind. The goal was to build a robust turbine that would be able to handle many open water deployments so that ample performance data can be taken. A lot of time and money went into the turbine design in hopes that the next generation might use the existing turbine and would not have to start from scratch with a completely new design.

The one aspect that was not fully covered by this year's group and that could greatly benefit from more in depth research would be the generator actuation system. The ideal actuation system would be a passive system with the ability to automatically position itself in the optimal location for any current velocity. This proves to be a very complex problem and data will need to be acquired to aid the design and calibration of this type passive system.

References

[1] Abbott, Ira H. A., and Albert Edward Doenhoff. *Theory of wing sections, including a summary of airfoil data*, . [Corr. version, ed. New York: Dover Publications, 1959. Print.

[2] "Analysis of Airfoils." *Javafoil*. N.p., n.d. Web. 1 Apr. 2011. <://www.mh-aerotools.de/airfoils/jf_applet.htm>.

[3] Eggleston, David M., and Forrest S. Stoddard. *Wind turbine engineering design* . New York: Van Nostrand Reinhold, 1987. Print.

[4] Figliola, R. S., and D. E. Beasley. *Theory and design for mechanical measurements* . 4th ed. Hoboken, N.J.: John Wiley & Sons, 2006. Print.

[5] Manwell, J. F., J. G. McGowan, and Anthony L. Rogers. "3-Aerodynamics of Wind Turbines." *Wind energy explained: theory, design and application*. 2nd ed. Chichester, U.K.: Wiley, 2009. 83-140. Print.

[6] "Marine and Hydrokinetic Energy." *Renewable Energy Focus*. N.p., n.d. Web. 15 Apr. 2011. <www.renewableenergyfocus.com/view/6346/marine-and-hydrokinetic-energy-can-play-a-substantial-role-in-clean-energy-options>.

[7] Ogata, Katsuhiko. *System dynamics* . 4th ed. Upper Saddle River, NJ: Pearson/Prentice Hall, 2004. Print.

[8] "Optical Laser Sensors." *Monarch Instrument*. N.p., n.d. Web. 20 Nov. 2010. <http://www.monarchinstrument.com/product.php?ID=46>.

[9] "Panel Tachometers: ACT Series" *Monarch Instrument*. N.p., n.d. Web. 20 Nov. 2010. <http://www.monarchinstrument.com/product.php?ID=16>.

[10] "Refraction - Snell's Law." Web. 14 Dec. 2010. <http://interactagram.com/physics/optics/refraction/>.

[11] Spera, David A.. *Wind turbine technology: fundamental concepts of wind turbine engineering*. New York: ASME Press, 1994. Print.

[12] "UNH Center for Ocean Renewable Energy: CORE." *University of New Hampshire*. N.p., n.d. Web. 15 Apr. 2011. <http://www.unh.edu/core/>.

Appendix A – Experimental Data

Preliminary Generator Bench-top Data

Trial (130)	*RPM*	*[rpm]*	129	128	130	130	129	131	130	129	130	129	130	**129.5455**	<-- Average RPM
	?X	*[inch]*	0.6875	0.84375	1	1.1875	1.3125	1.46875	1.625	1.75	1.875	1.96875	2.03125		
	A	*[inch]*	-1.9443	-1.6695	-1.3843	-1.0258	-0.7747	-0.4443	-0.0906	0.2140	0.5441	0.8141	1.0080		
	Resistance	*[ohms]*	7.50	7.50	7.50	7.50	7.50	7.50	7.50	7.50	7.50	7.50	7.50		
	Voltage	*[volts]*	0.011	0.017	0.028	0.048	0.085	0.156	0.29	0.533	0.78	0.966	1.005		
	Current	*[ampre]*	0.075	0.126	0.214	0.372	0.677	1.266	2.354	4.19	6.12	7.51	7.78		
	Power	*[watts]*	0.010547	0.029768	0.085868	0.25947	0.859367	3.005168	10.38997	32.91769	70.227	105.7502	113.4908		

Trial (120)	*RPM*	*[rpm]*	120	120	120	120	120	120	120	118	119	120	120	**119.7273**	<-- Average RPM
	?X	*[inch]*	0.6875	0.875	1.0625	1.21875	1.375	1.5	1.625	1.75	1.875	2	2.03125		
	A	*[inch]*	-1.9443	-1.6133	-1.2670	-0.9640	-0.6450	-0.3756	-0.0906	0.2140	0.5441	0.9094	1.0080		
	Resistance	*[ohms]*	7.50	7.50	7.50	7.50	7.50	7.50	7.50	7.50	7.50	7.50	7.50		
	Voltage	*[volts]*	0.012	0.019	0.031	0.054	0.096	0.175	0.333	0.58	0.823	0.986	0.997		
	Current	*[ampre]*	0.083	0.14	0.241	0.422	0.765	1.434	2.711	4.58	6.38	7.61	7.71		
	Power	*[watts]*	0.012917	0.03675	0.108902	0.333908	1.097297	3.855668	13.78035	39.33075	76.32075	108.5852	111.4577		

Trial (110)	*RPM*	*[rpm]*	110	109	111	110	110	110	110	109	111	110	110	**110**	<-- Average RPM
	?X	*[inch]*	0.65625	0.84375	1	1.15625	1.3125	1.4375	1.625	1.75	1.875	1.96875	2.03125		
	A	*[inch]*	-1.9982	-1.6695	-1.3843	-1.0869	-0.7747	-0.5120	-0.0906	0.2140	0.5441	0.8141	1.0080		
	Resistance	*[ohms]*	7.50	7.50	7.50	7.50	7.50	7.50	7.50	7.50	7.50	7.50	7.50		
	Voltage	*[volts]*	0.011	0.016	0.027	0.046	0.081	0.146	0.27	0.498	0.754	0.945	0.981		
	Current	*[ampre]*	0.072	0.121	0.208	0.356	0.648	1.202	2.252	3.93	5.84	7.15	7.59		
	Power	*[watts]*	0.00972	0.027452	0.08112	0.23763	0.78732	2.709008	9.50907	28.95919	63.948	95.85469	108.0152		

Trial (100)	*RPM*	*[rpm]*	100	100	100	100	100	99	100	102	102	102	100	**100.4545**	<-- Average RPM
	?X	*[inch]*	0.6875	0.84375	1	1.15625	1.3125	1.4375	1.625	1.75	1.875	1.9675	2.03125		
	A	*[inch]*	-1.9443	-1.6695	-1.3843	-1.0869	-0.7747	-0.5120	-0.0906	0.2140	0.5441	0.8103	1.0080		
	Resistance	*[ohms]*	7.50	7.50	7.50	7.50	7.50	7.50	7.50	7.50	7.50	7.50	7.50		
	Voltage	*[volts]*	0.01	0.016	0.025	0.044	0.076	0.138	0.258	0.478	0.724	0.9	0.945		
	Current	*[ampre]*	0.069	0.116	0.198	0.343	0.616	1.125	2.109	3.656	5.6	7.01	7.45		
	Power	*[watts]*	0.008927	0.02523	0.073508	0.220592	0.71148	2.373047	8.339777	25.06188	58.8	92.13769	104.0672		

Trial (130)	*RPM*	*[rpm]*	130	129	132	131	131	130	132	130	131	131	131	**130.7273**	<-- Average RPM
	?X	*[inch]*	0.6875	0.8125	1	1.15625	1.3125	1.4375	1.625	1.71875	1.875	1.9375	2.03125		
	A	*[inch]*	-1.9443	-1.7252	-1.3843	-1.0869	-0.7747	-0.5120	-0.0906	0.1357	0.5441	0.7216	1.0080		
	Resistance	*[ohms]*	7.50	7.50	7.50	7.50	7.50	7.50	7.50	7.50	7.50	7.50	7.50		
	Voltage	*[volts]*	0.01	0.016	0.027	0.045	0.077	0.138	0.255	0.472	0.725	0.924	0.992		
	Current	*[ampre]*	0.072	0.12	0.203	0.349	0.611	1.144	2.125	3.873	5.77	7.31	7.81		
	Power	*[watts]*	0.00972	0.027	0.077267	0.228377	0.699977	2.45388	8.466797	28.12524	62.42419	100.1927	114.3677		

Trial (120)	*RPM*	*[rpm]*	121	120	120	120	120	119	119	120	119	120	121	**119.9091**	<-- Average RPM
	?X	*[inch]*	0.65625	0.8125	1	1.1875	1.3125	1.4375	1.5625	1.71875	1.84375	1.9375	2.03125		
	A	*[inch]*	-1.9982	-1.7252	-1.3843	-1.0258	-0.7747	-0.5120	-0.2353	0.1357	0.4588	0.7216	1.0080		
	Resistance	*[ohms]*	7.50	7.50	7.50	7.50	7.50	7.50	7.50	7.50	7.50	7.50	7.50		
	Voltage	*[volts]*	0.011	0.016	0.026	0.044	0.077	0.139	0.254	0.474	0.728	0.92	0.984		
	Current	*[ampre]*	0.072	0.119	0.201	0.345	0.624	1.141	2.12	3.897	5.78	7.27	7.73		
	Power	*[watts]*	0.00972	0.026552	0.075752	0.223172	0.73008	2.441027	8.427	28.47489	62.64075	99.09919	112.0367		

Appendix B – Course Reports

HYDROKINETIC TURBINE

Rotor Design and Performance Calculation

Nathaniel Allen

ME 795: Renewable Energy
2010 – 2011

UNIVERSITY of NEW HAMPSHIRE

Table of Contents

List of Figures

List of Tables

Introduction

The most important component of any turbine in respect to performance is the rotor. This is because in any given flow there is a finite amount of kinetic energy and the rotor is the component of a turbine which converts this kinetic energy into usable energy. The more efficient a rotor is the more energy a turbine will potentially be able to harvest from a flow. A simple one-dimensional momentum theory can be used to determine the performance from an ideal rotor which is generally characterized by its power coefficient. The power coefficient is the ratio of how much power the rotor extracts to the total power in the flow. The "Betz Limit" defines the theoretical maximum power coefficient for an ideal turbine rotor to be 16/27 or 0.593. This maximum performance only decreases when considering real world factors like two-dimensional momentum, wake rotation, turbulence, etc. which is why it is crucial for any turbine design to optimize the rotor performance.

Theory

Energy Extraction

The total theoretical power available in a flow of fluid is

$$P_{theoretical} = \frac{1}{2}\rho A U^3,$$

where ρ is the density of the fluid, A is the swept area of the rotor and U is the free stream velocity of the fluid. Because the density and swept area are assumed constant, the theoretical power in a flow is assumed proportional to the cube of its velocity.

In hydrokinetics the marine currents tend to be very slow compared to wind speeds, however since the density of water is 823 times greater than air, the energy content of a marine current of only 1 m/s is equivalent to a wind speed of 9 m/s.

The power that a turbine can actually extract from a fluid flow will be reduced by the efficiencies of the device. The actual power that can be extracted from a flow is

$$P_{actual} = \eta_R \eta_M \eta_E \frac{1}{2}\rho A U^3,$$

where η_R is the rotor efficiency which is typically referred to as the power coefficient, C_P; η_M is the mechanical efficiency of the device and incorporates transmission, bearing and gearbox losses; η_E is the electrical efficiency which includes the generator and power conditioning losses. The power coefficient is defined as the ratio of power extracted by the rotor to the theoretical power available in the flow.

Generally the electrical and mechanical efficiencies are very high, usually around 0.9. These efficiencies are typically much greater than the rotor efficiency. The maximum theoretically possible rotor power coefficient is defined by the Betz limit and is 16/27 or 0.5926. This is based on an idealized model and therefore in practice efficiencies of less than 0.5 are usually seen.

Angle of Relative Flow

It can be seen that blades designed for optimum power production have increasingly large chord and twist angle as one gets closer to the blade root. The blade is designed with twist so that each blade cross section will have an optimal angle of attack to the relative flow that is experienced by the blade. The angle and magnitude of the relative flow is dependent on the free stream velocity as well as the tangential velocity of each blade section. Below in Figure 1 is a velocity vector diagram that shows a blade cross section and its tangential velocity vector, the velocity vector of the free stream velocity and the relative velocity vector which is the vector sum of the previous two.

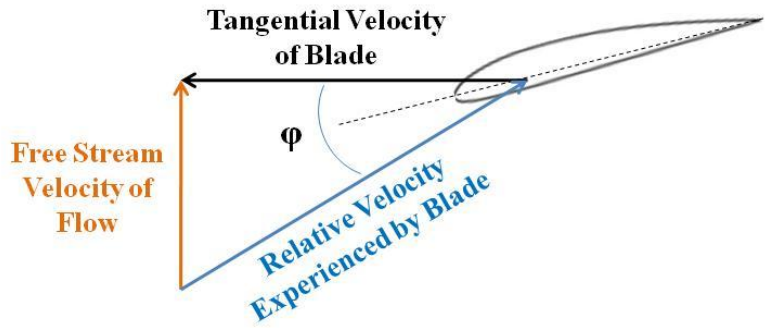

Figure 1: Velocity vector diagram of blade cross section

The angle of relative flow is the angle between the relative velocity vector and the rotor plane of rotation. This angle is depicted as φ in Figure 1 above. If the free stream velocity is assumed to be constant than that velocity vector will remain the same magnitude. The change of the angle of relative flow is created because the blade cross section at the blade tip is traveling at a greater tangential velocity than the blade cross section at the rotor hub. This change in tangential velocity changes the geometry of the vector diagram as seen below in Figure 2.

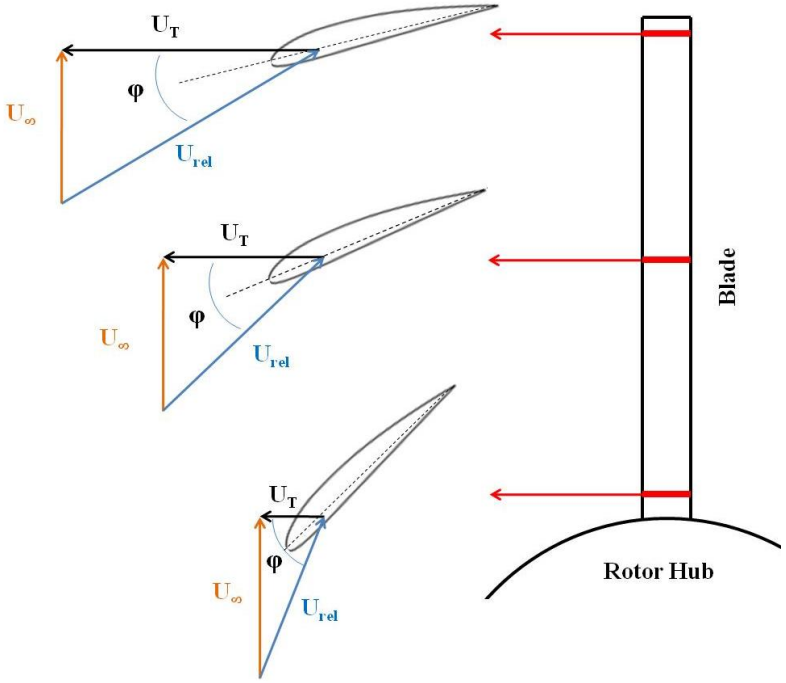

Figure 2: Velocity vector diagrams showing rotation of relative flow

General Aerodynamic Concepts

Hydrokinetic turbines power production depends on the interaction between the rotor and the current flow. Most horizontal axis turbine blade designs use airfoils to develop mechanical power. Airfoils are structures with specific geometric shapes that are used to generate mechanical forces due to the relative motion of the airfoil and the surrounding fluid flow.

Airfoil Terminology

The chord, *c*, of the airfoil is the straight line distance between the leading and trailing edges. The angle of attack, α, is defined as the angle between the chord line and the relative wind, U_{rel}. The thickness of an airfoil is the distance between the top and bottom surfaces measure perpendicular to the chord line. The mean camber line is the line that lies halfway between the upper and lower surfaces. If the airfoil is symmetric the mean camber line lies on the chord line. This terminology is shown pictorially on an airfoil profile below in Figure 3.

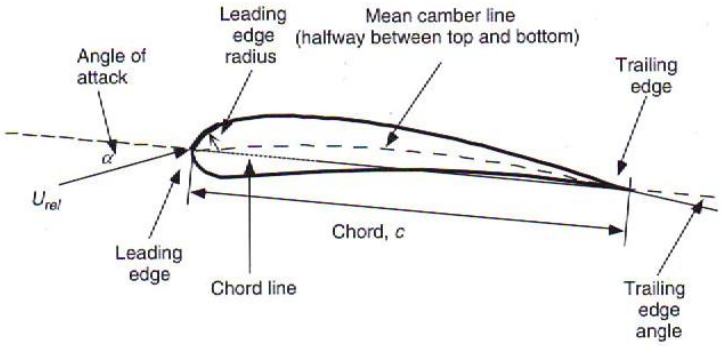

Figure 3: Airfoil Nomenclature

Aerodynamic Forces

A fluid flow over an airfoil creates a distribution of pressure and frictional forces. These pressure and frictional forces can be resolved into a lift force, drag force and pitching moment as displayed in the following figure. These resultant forces have been found to act along the chord at a quarter of its length measured from the leading edge. The lift force is defined to be the force perpendicular to the relative flow direction and the drag force is defined to be parallel to the relative flow direction. Cross sections of rotor blades have airfoil profiles, therefore the lift and drag forces that develop at a finite distance from the rotor's axis of rotation which creates a torque on the rotor making it spin.

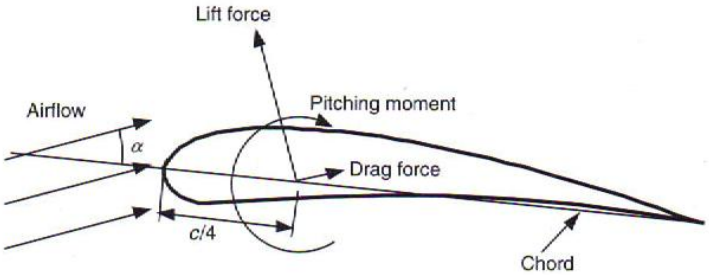

Figure 4: Forces and moments on airfoil section

The lift and drag forces can be numerically defined as

$$F_L = C_L \frac{1}{2} \rho A_p U^2 \text{ and } F_D = C_D \frac{1}{2} \rho A_p U^2$$

where C_L and C_D are the non-dimensional lift and drag coefficients, ρ is the density of the fluid, A_p is the planform area (chord x span) and U is the free stream velocity of the fluid. The lift and drag coefficients are functions of the Reynolds number, defined as the ratio of inertial to viscous forces. The Reynolds number is numerically represented as

$$Re = \frac{UL}{\nu},$$

where U is the water free stream velocity, L is distance traveled (chord length) and ν is the kinematic viscosity of water (μ/ρ). For every Reynolds number there are different flow characteristics around the airfoil resulting in different lift and drag coefficients. This relationship is characterized using experimental data as shown below in Figure 5. The figure shows the coefficient of lift versus angle of attack and the coefficient of drag versus angle of attack data for a NACA 0012 airfoil at varying Reynolds number.

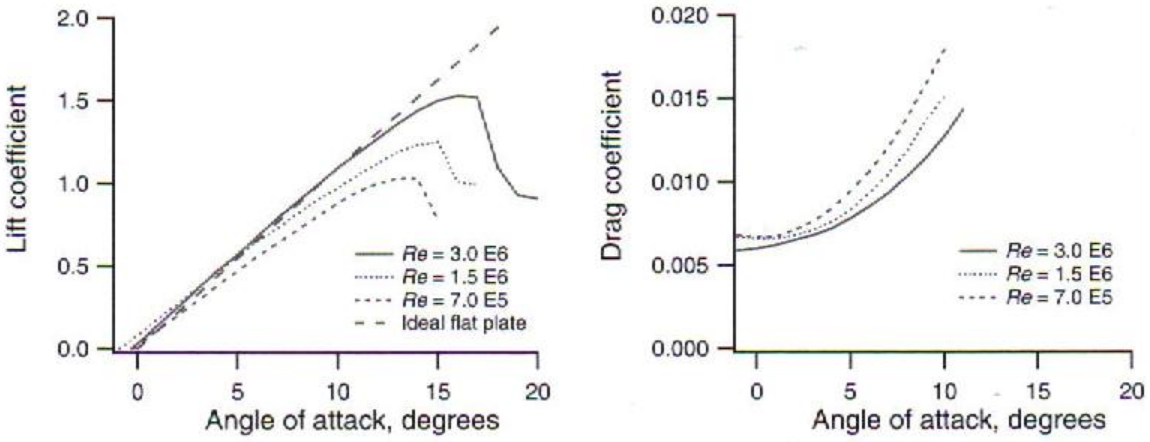

Figure 5: Experimental C_L and C_D

The optimal angle of attack can be determined using this experimental data by determining when the ratio of C_D/C_L is minimum. At this location there will be the largest lift force and the smallest drag force producing the maximum amount of torque.

Blade Design

An ideal blade shape was derived using Blade Element Momentum (BEM) theory which is extensively used in the Wind turbine industry. BEM theory is a combination of both momentum theory which is a control volume analysis of forces on the blade and blade element or strip theory which is the analysis of forces at a specific blade section as a function of local blade geometry. Using BEM the optimal blade shape and performance characteristics can be calculated for each annular section of the blade. The entire shape and performance of the blade can then be obtained by summing the calculated values for each annular section.

Blade Element Momentum Theory

As mentioned above, momentum theory relations can be combined with those from blade element theory to relate blade shape and performance. Due to the lengthy derivations in each theory and the complexity of the algebra as the theories are combined, only the resulting equations used to evaluate blade shape and performance are presented.

The ideal blade shape can be determined using an optimum rotor theory with wake rotation. This optimization includes wake rotation, but initially ignores drag and tip losses. The resulting equations for the optimized blade shape can be obtained by taking the partial derivative of the power coefficient equation that was derived from momentum theory including wake rotation.

The blade shape of each annular section is defined by the airfoil shape, chord and twist angle. The chord length of the airfoil profile was calculated using the following equation

$$c_i = \frac{8\pi r_i}{BC_{l,design,i}}\{1 - cos(\varphi_i)\}$$

with the subscript *(i)* indicating the blade section, *(c)* the chord length, *(r)* the radius to the center of the blade section, *(B)* the number of blades, $(C_{l,design})$ the chosen coefficient of lift for the blade design and (φ) the angle of relative flow. The angle of relative flow is defined as

$$\varphi_i = (2/3) * tan^{-1}(1/\lambda_i)$$

where (λ) is the tip-speed-ratio of blade section *(i)*. This angle of relative flow can also be used to define the twist angle of the blade. The twist angle of the blade section is calculated from the following equation

$$\theta_{T,i} = \left(\varphi_i - \alpha_{design,i}\right).$$

In this equation (θ_T) is the angle of twist of the blade section which closes tracks the angle of relative wind only being offset by the designed optimal angle of attack for that blade section, (α).

With the blade shape optimized its theoretical performance can then be determined. The blade shapes performance is evaluated using the power coefficient. The analysis of the power coefficient includes wake rotation, drag effects, losses from a finite number of blades and off-design performance. The power coefficient for each blade section is derived using an iterative method to determine acceptable axial and angular induction factors based on tip losses and thrust coefficients. The total power coefficient of the blade is calculated by summing the contributions of each annular section to approximate an integral. The power coefficient is calculated from this equation

$$C_p = \sum_{i=1}^{N} \left(\frac{8\Delta\lambda_r}{\lambda^2}\right) F_i sin^2(\varphi_i)\{cos(\varphi_i) - \lambda_{r,i} sin(\varphi_1)\}\{sin(\varphi_i) + \lambda_{r,i} cos(\varphi_{r,i})\} \ldots$$
$$[1 - \left(\frac{C_d}{C_l}\right) cot(\varphi_i)]\ {\lambda_{r,i}}^2$$

where *(C_p)* is the power coefficient, *(N)* is the number of blade elements chosen and *(F)* is the tip loss factor.

Rotor Design Code

A rotor design code was created in Matlab based off of a generalized rotor design procedure presented in Wind Energy Explained (Manwell, 2009). The code begins by allowing the user to define basic turbine parameters and operating conditions. An example of these inputted parameters is presented in Table 1 below.

Table 1: Input Parameters for rotor design code

Radius of Rotor [inch]	30.0
Radius of Hub [inch]	9.0
Number of Blades	6.0
Number of Blade Elements	20
Tip-Speed-Ratio	3.0
Flow Velocity [knots]	6.0
Reynolds Number	125,000

The values in the above table are the chosen parameters and operating conditions used for the design of the final blade shape. The diameter of the turbine rotor was designated to be 5 feet. To increase the direct drive generator efficiency, a 19 inch hub diameter was chosen. Therefore, the blades are designed to be 21 inches in length. Six blades were chosen for the complete rotor based on practical dynamic stability issues and on the tip-speed-ratios expected for a hydrokinetic application. The blades were designed for the largest flow speed expected, 6 knots or roughly 3 m/s. This was done to ensure that the blades would be most efficient when the flow contained the largest amount of kinetic energy allowing the rotor to extract maximum power. A tip-speed-ratio of 3 was chosen so that the rotor would spin at realistic rotational speeds for a marine application.

Once the operating conditions and parameters were inputted, the user then designates a hydrofoil profile for the code to use in design calculations. The user inputs this designation by inputting the name of the foil along with its aerodynamic characteristics, i.e. coefficient of lift and drag versus angle of attack. These performance characteristics are inputted into the code using a three column tabular form which the code can automatically interpret and sort. This performance data was compiled using Javafoil and therefore is only as accurate as the analytical model used in that program. Although Javafoil is less accurate than experimental data, it provided a much easier solution to obtain tabular data for all profiles tested, where as experimental data for some profiles tested was unavailable and tabular data was hard to come by.

Once the airfoil profile is chosen and the performance data is inputted, the code then implements BEM theory and derives the optimal blade shape for that profile. BEM theory begins by dividing the blade into a specified amount of annular sections. Our blade was designed using 20 sections which proved to have an effective balance between accuracy and computation time. The derived blade shape is defined using the chord and twist for each blade element.

To visually show the change in chord and twist versus the location along the blade radii, the code outputs two plots; chord length versus blade radius and blade twist angle versus blade radius. An example of these two plots can be seen in the following figure for an LS(1)-0413 airfoil profile. From these plots is can be seen that the optimal blade design has an increasingly large chord and twist angle as one approaches the rotor hub. Note the rotor hub is 19 inches in diameter therefore the blade does not start until a radial location of greater than 9.5 inches

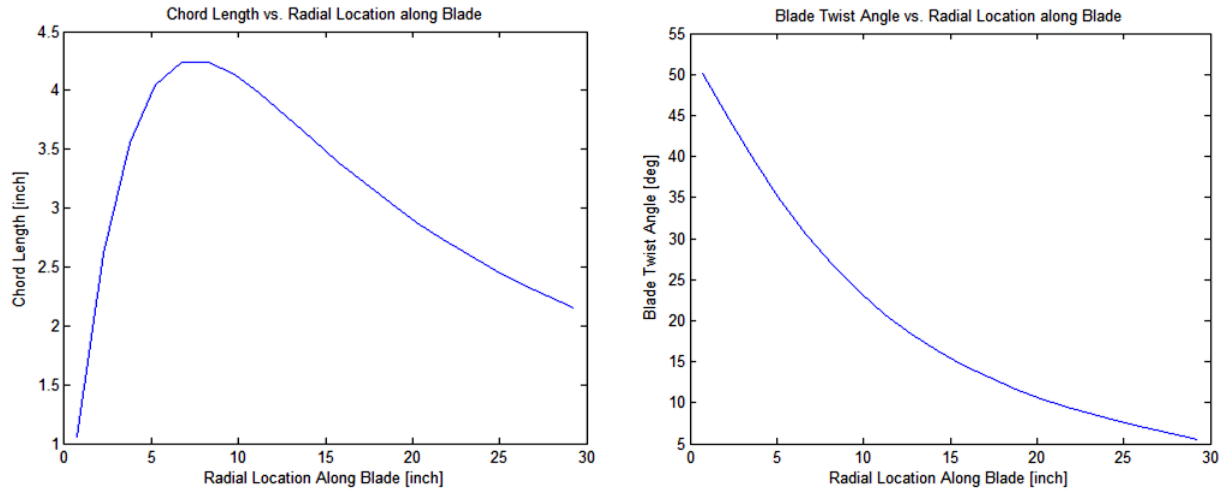

Figure 6: Chord length and angle of twist plots for an LS(1)-0413 profile

With the blade shape defined the code then calculates the theoretical rotor performance. The rotor performance is determined by calculating the power coefficient at each annular element. The total power coefficient of the blade is then determined using a sum approximating an integral over the blade. The power coefficient is defined as the ratio of how much usable energy the rotor extracts to how much theoretically available energy is in the flow. With the shape and performance calculated the code then analyzes the expected lift and drag forces on each blade element. These forces can then be used for a structural analysis of the blade. All these values are

outputted in an organized table showing the calculated values for each annular element and the totals for the entire blade. An example of this output is shown in Table 2 below for an Eppler E387 airfoil profile. The values in this table were derived using the input parameters given in Table 1 above.

Table 2: Design code output for a Eppler E387 profile

Radius [inch]	Chord [inch]	Angle of Relative Flow	Blade Twist Angle	Power Coefficient	Lift Force [lbs]	Drag Force [lbs]
9.8	5.49	30.48	24.98	0.0157	11.70	0.19
11.3	5.27	27.76	22.26	0.0187	13.05	0.22
12.8	5.02	25.41	19.91	0.0217	14.41	0.24
14.3	4.76	23.37	17.87	0.0246	15.77	0.26
15.8	4.51	21.61	16.11	0.0275	17.15	0.29
17.3	4.26	20.07	14.57	0.0304	18.53	0.31
18.8	4.04	18.71	13.21	0.0332	19.92	0.33
20.3	3.82	17.52	12.02	0.0358	21.33	0.36
21.8	3.63	16.46	10.96	0.0384	22.74	0.38
23.3	3.45	15.52	10.02	0.0405	24.15	0.40
24.8	3.28	14.67	9.17	0.0417	25.58	0.43
26.3	3.13	13.90	8.40	0.0416	27.01	0.45
27.8	2.99	13.21	7.71	0.0374	28.44	0.47
29.3	2.86	12.58	7.08	0.0142	29.88	0.50
			Totals →	0.4341	300.00	4.99

Design Analysis

Using this design code multiple sets of design iterations were run to determine the ideal airfoil for the specified conditions. A truly optimal blade might have different profiles or different thicknesses at different locations along the blade. This is because a thicker airfoil is more advantageous at the base because it will have a greater structural integrity. And conversely a thinner and more efficient airfoil is advantageous at the tip where more power is extracted and less force experienced. Various different comparative design analyses were done to try and identify ideal profiles and shapes for each section along the blade. These could then be compiled into the best overall blade design for our specific scenario.

First Analysis

For the first design analysis, 9 different airfoil profiles were selected to be compared. These 9 foils were chosen because they were all foils that are currently or have been traditionally used in wind turbine blade designs.

In the early development of wind turbines NACA 44XX and NACA 230XX were used because of their known high lift coefficients and low drag. As understanding of the optimal

blade shape grew, airfoils like the NASA LS(1)-XXXX and NACA 63(2)-XX became used to reduce the leading edge roughness sensitivity of the turbine blades. More recently, specific design codes have been developed and used to design new airfoil profiles specifically for horizontal axis wind turbines. One example of this includes the SERI or S-series airfoils.

The 9 airfoil profiles tested were; FX63-137, NACA 4415, SD 2030, LS(1)-0413, NACA 63(2)-15, SERI S819, NACA 23015, NACA 0012, E387. Figure 7 below shows the SERI S819 airfoil shape. The other 8 airfoil profiles are shown in Appendix-A.

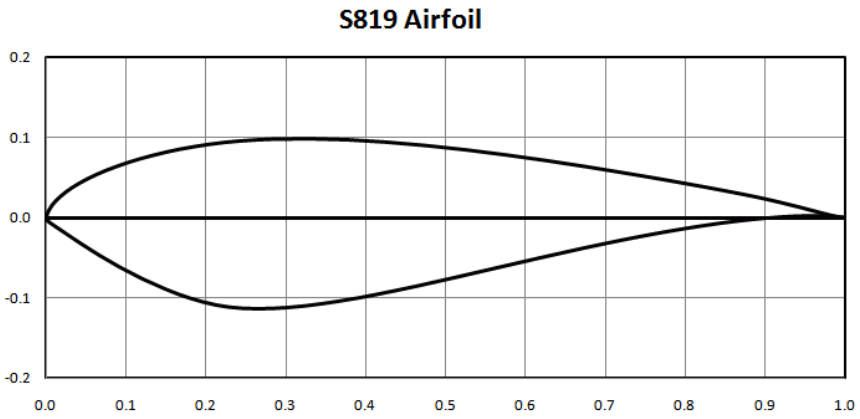

Figure 7: SERI S819 airfoil profile used in design code

These profiles were all run through the design code and the resulting blade shape and performance was determined. The overall performance of each airfoil was then compared to determine which foils proved better for our application. The different airfoil blade designs were compared based on the theoretically calculated blade performance. This blade performance was evaluated using the power coefficient. Table 3 below shows the calculated power coefficient for all 9 airfoil blade designs.

Table 3: Blade performance comparison

Airfoil	Cp
FX63 - 137	0.456
NACA 4415	0.447
SD 2030	0.444
LS(1)-0413	0.442
NACA 63(2)-15	0.440
SERI S819	0.439
NACA 23015	0.438
NACA 0012	0.435
E387	0.434

In the above table it should be noted how close the overall performance of each blade design is. The different profile designs only have a total power coefficient range of 0.022. This may seem small however; when considering each blade was designed to have an optimal shape for that specific profile it is more reasonable. The main variation between the blades is not the twist and taper but the performance characteristics of the airfoils. This being said each profile will have unique performance characteristics however as you can tell from the above table it does not affect the overall performance of the blade that drastically.

Second Analysis

Having effectively compared the overall performance of each chosen profile, it was also important to determine thickness effects for the different profile series that were chosen. This is important for determining the variation of profile thicknesses over the blade length. Four of the profile families tested above did not have profiles that varied only by percent thickness and therefore each profile had a fairly unique shape. This would add to the complexity of the blade analysis and therefore the following series of foils were not tested for thickness comparison; E3XX, FX63 – XXX, SD2XXX and the LS(1)-04XX. The remaining 5 airfoil series were all tested to determine the percent thickness effects which are presented in the following table.

Table 4: Profile thickness comparison

Airfoil Series	Profile	Cp
NACA 44XX	4412	0.4463
	4415	0.4469
	4418	0.4431
	4421	0.4407
	4424	0.4373
NACA 00XX	0012	0.4398
	0015	0.4282
	0018	0.4271
	0021	0.4251
	0024	0.4229
SERI S8XX	S815	0.4197
	S817	0.4273
	S819	0.4396
	S821	0.4277
	S822	0.4354
NACA 230XX	23012	0.4330
	23015	0.4378
	23018	0.4327
	23021	0.4333
	23024	0.4235
NACA 63(2)-XX	63(2)-12	0.4309
	63(2)-15	0.4402
	63(2)-18	0.4323
	63(2)-21	0.4299
	63(2)-24	0.4258

As expected there was variation in the performance within each series of airfoils depending on the percent thickness of the airfoil. The overall general trend seen is that the best thickness was on the thinner side and as the airfoil thickness increased its performance decreased. For the NACA 00XX series foils the blade design with the best performance was from its thinnest profile, the NACA 0012. For the rest of the NACA family foils, the best performance came from the profiles that had 15 percent thickness to chord. The SERI series foils were slightly different and its maximum performance came from its S819 profile. The NACA family foils experience much smoother and more predictable trend variations compared to the SERI series foils. For the S8XX profiles the performance did not very directly with the thickness. This series of foils also experienced the largest range of power coefficients. The airfoil series that experienced by far the smallest deviation of power coefficient was the NACA 44XX series airfoils. Not only did this series have the smallest variation for different profile thicknesses, it also had the highest C_p values out of all the airfoil series compared.

Final Blade Design

From the previously mentioned to analyses, the NACA 44XX series was chosen as the ideal airfoil series for our final blade design. This series was chosen because it had the second highest power coefficient compared to the other 8 profiles tested in the first analysis and because it had by far the smallest deviation of power coefficient with respect to the percent thickness in the second analysis. The high power coefficient was favorable because it increases the potential amount of energy that can be harvested from a flow. The small deviation and predictable trend of blade performance to profile thickness was ideal for a blade design having a varying thickness throughout the blade.

Using the optimal blade shapes for the five NACA airfoils (4412, 4415, 4418, 4421, and 4424) a finite element structural analysis was conducted in ME786 class, “Intro to FEA”. This analysis determined the NACA 4421 profile (21% thickness based on chord length) to be an acceptable thickness for the stress that the blade will be experiencing near the hub. The analysis also showed that the stress in the blade decreases as the radius increases, therefore the profile thickness could also decrease while still maintaining an acceptable factor of safety. The conclusion of the ME786 structural analysis was to vary the thickness starting at a 4421 for the hub and decreasing to a 4418 and then to a 4415 at the tip.

Due to the increased complexity of varying the thickness along the radii of the blade and due to the minimal decrease in overall power coefficient by keeping a constant thickness, the final blade design was chosen to use a NACA 4421 profile throughout the length of the blade. The greater profile thickness resulted in an overall stronger blade which is advantageous for the large forces experienced in marine environments. Along with this, a minimal decrease in performance was encountered making this the ideal choice for the final blade design.

The final blade design using a NACA 4421 profile and the operating parameters and conditions shown above in Table 1, is shown below in Figure 8. Figure 8 contains three different views of the 3D computer model of the blade made using Solidworks. The blade has a 3.84 inch chord length at the hub which tapers to a 2.00 inch chord at the tip of the blade. The blade twists from

approximately 23.5^{o} at the hub to 5.5^{o} at the tip. Therefore the blade contains 18 degrees of twist and 1.84 inches of chord taper.

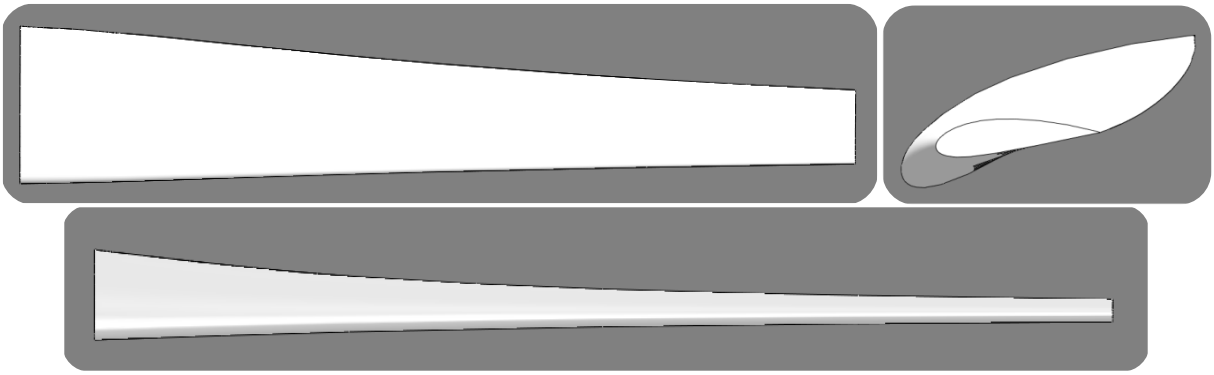

Figure 8: CAD model of final blade design
(top, end and side view)

Conclusion

An ideal blade shape for a 5 foot diameter hydrokinetic turbine was derived using Blade Element Momentum (BEM) theory. This was achieved by using BEM theory to create a design code in Matlab. This code was used to derive the optimal blade shape for various airfoil profiles. The code was also designed to evaluate the theoretical performance of these optimal blade shapes. By comparing various airfoil profiles and various profile thicknesses, the ideal airfoil series was determined that yielded a high power coefficient with minimal variation with respect to increasing profile thickness. The chosen airfoil series was the NACA 44XX series. The final chosen blade design used a NACA 4421 profile throughout which provided the necessary structural integrity while still maintaining a high power coefficient.

References

[1] Abbott, Ira H. A., and Albert Edward Doenhoff. *Theory of wing sections, including a summary of airfoil data,* . [Corr. version, ed. New York: Dover Publications, 1959. Print.

[2] "Analysis of Airfoils." *Javafoil*. N.p., n.d. Web. 1 Apr. 2011. <://www.mh-aerotools.de/airfoils/jf_applet.htm>.

[3] Eggleston, David M., and Forrest S. Stoddard. *Wind turbine engineering design* . New York: Van Nostrand Reinhold, 1987. Print.

[4] Manwell, J. F., J. G. McGowan, and Anthony L. Rogers. "3-Aerodynamics of Wind Turbines." *Wind energy explained: theory, design and application*. 2nd ed. Chichester, U.K.: Wiley, 2009. 83-140. Print.

[5] Spera, David A.. *Wind turbine technology: fundamental concepts of wind turbine engineering*. New York: ASME Press, 1994. Print.

Appendix – A *(Airfoil Profiles)*

NACA 63-215 AIRFOIL

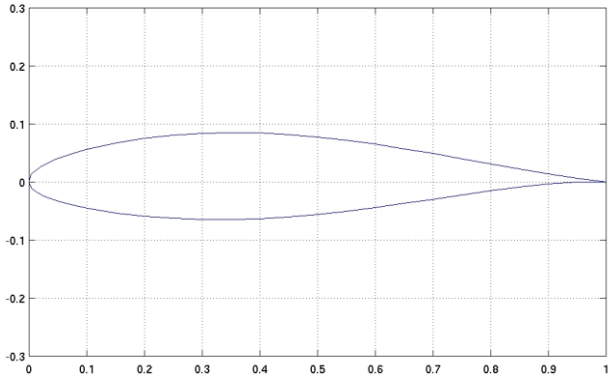

SD2030-086-88

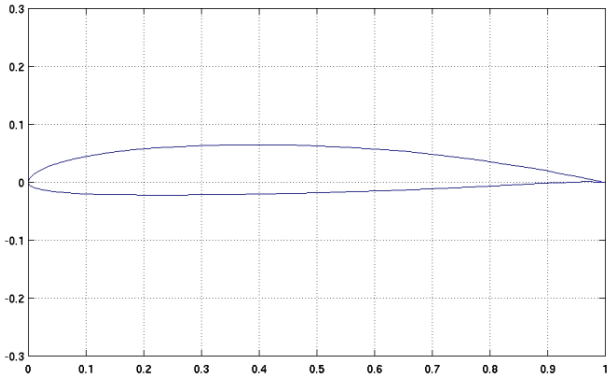

NACA 0015

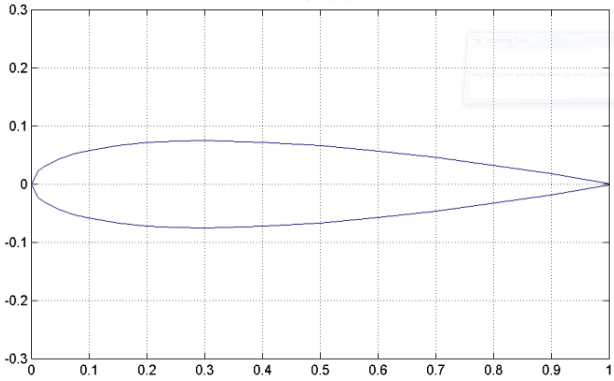

NACA 4415

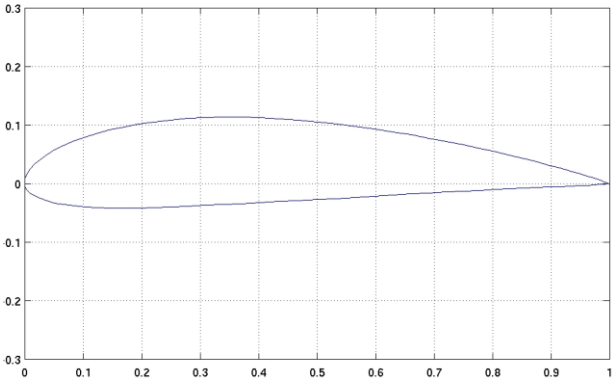

NACA 23015

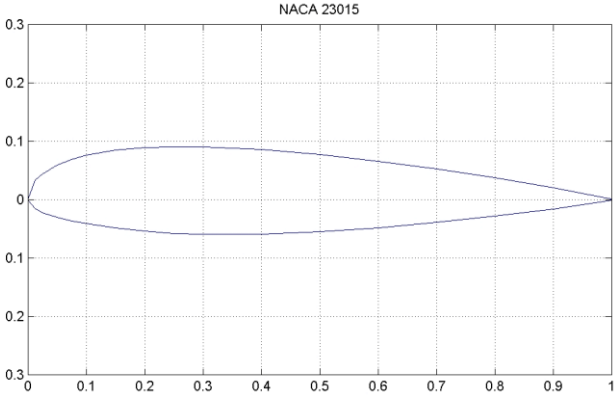

NASA/LANGLEY LS(1)-0413MOD AIRFOIL

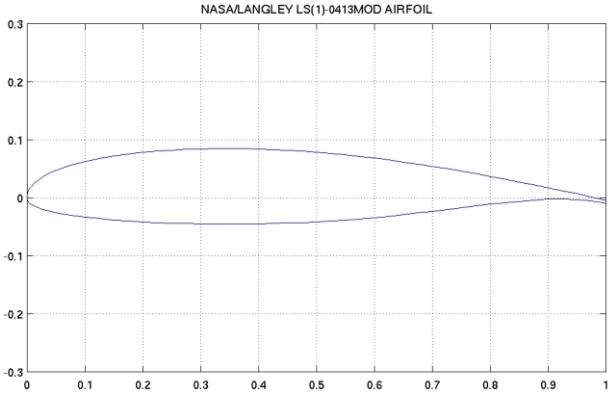

WORTMANN FX 63-137 AIRFOIL

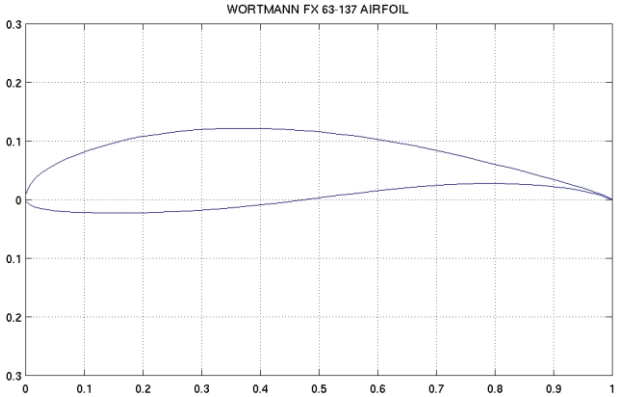

E387

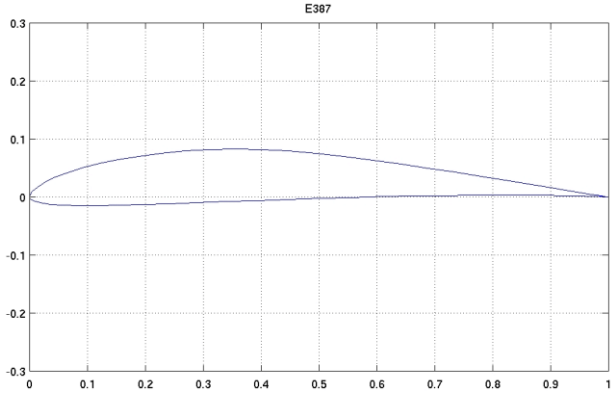

Appendix – B *(Matlab Design Code)*

```
%% Rotor Design
 clear;
 clc;

%% Basic Rotor Parameters
 % Radius of entire rotor, blade and hub [inch]
 R = 30;
 % Radius of hub only [inch]
 hub = 9;
 % Free Stream Velocity
 U_knot = 6; %[knots]
 U = (U_knot*1.687810)*(12); %[inch/s]
 % Tip-Speed Ratio [unitless]
 TSR = 3;
 % Number of Blades
 B = 6;
 % Number of blade elements
 N = 20;
 % Kinematic Viscosity of Water @ 50 F
 v = 1.407*10^-5; % [ft^2/s]

 % Airfoil choice
 % Imports empirical Cl, Cd, and alpha data
 profile = 'NACA 4421';
 airfoil = importdata('NACA4421j.txt');
 t=1;
 while(t <= length(airfoil))
     % Vector of angles of attack
     alpha_data(t,1) = airfoil(t,1);
     % Vetor of corresponding lift coefficients
     Cl_data(t,1) = airfoil(t,2);
     % Vector of corresponding drag coefficients
     Cd_data(t,1) = airfoil(t,3);
     t = t + 1;
 end

%% Define Blade Shape
 %%%% Optimal Angle of attack %%%%

 % Determines where(Cd/Cl)is minimum
 s = 1; % counter
 min = 1; % minimum (Cd/Cl) value. Assume initial value
 while (s <= length(airfoil))
     ratio = Cd_data(s)/Cl_data(s);
     if (ratio < min)
         min = ratio;
         % Indice of the minimum ratio
         z = s;
     end
     s = s + 1;
 end

 % The optimal angle of attack (design value)
 alpha_deg = alpha_data(z);  % [degrees]
 alpha = alpha_deg*(pi/180); % [radians]
```

```
% The optimal lift coefficient (design value)
Cl = Cl_data(z);

% The optimal drag coefficient (design value)
Cd = Cd_data(z);

%{ Note:
   The optimal angle of attack and the corresponding lift and drag
   coefficients were assumed to be the same for every blade element. This
   will only vary if there is a large change in the Reynolds number From
   element to element.
%}

%%%% Optimum Rotor Theory %%%%
%{ Note: lowercase letters indicate the value for each element. %}

%{ Note: The tip of the blade is defined to have 0 twist %}

% Angle of relative flow at the blade tip
phi_o = (2/3)*atan(1/TSR);

% Blade pitch angle at the tip)
theta_po = phi_o-alpha;

% Radius to the center of each element
i = 1;
while (i <= N)
    r(i) = (R/(2*N))+((R/N)*(i-1));
    if (r(i)< hub)
        hub_index = i;
    end
    i = i + 1;
end

% Tip-Speed Ratio for each element
tsr = TSR.*(r./R);

% Angle of relative flow for each element
phi = (2/3).*atan(1./tsr);  % [radians]
phi_deg = phi*(180/pi);     % [degrees]

% Section pich angel for each element
theta_p = phi-alpha;           % [radians]
theta_pdeg = theta_p*(180/pi); % [degrees]

% Angle of twist for each element
twist = theta_p - theta_po;  % [radians]
twist_deg = twist*(180/pi);  % [degrees]

% Chord lenth for each element
c = (((8*pi).*r)./(B*Cl)).*(1-cos(phi)); % [inch]

% Calculates the Reynolds number of the flow
Re = (U*c)/(v*12^2);
```

```
  %%%% Plot of Chord vs. Radial Location along Blade %%%
  figure;
  plot(r,c);
  title('Chord Length vs. Radial Location along Blade');
  xlabel('Radial Location Along Blade [inch]');
  ylabel('Chord Length [inch]');

  %%%% Plot of Blade Twist Angle vs. Radial Location along Blade %%%%
  figure;
  plot(r,theta_pdeg);
  title('Blade Twist Angle vs. Radial Location along Blade');
  xlabel('Radial Location Along Blade [inch]');
  ylabel('Blade Twist Angle [deg]');

%% Rotor Performance
  %%%% Intitial Values %%%%
  %{ Based off of the design values chosen for an optimal blade %}

  % Angle of relative flow for each element
  phi_1 = (2/3)*atan(1./tsr);

  % Local Solidity
  sol = (B*c)./(2*pi*r);

  % Axial Induction Factor
  a_1 = 1./(1+((4*(sin(phi_1).^2))./(sol.*Cl.*cos(phi_1))));

  % Angular Induction Factor
  aa_1 = (1-(3*a_1))./((4*a_1)-1);

  %%%% Iteration Process %%%%
  acc_a = 1;
  acc_aa = 1;
  l = 1;
  while (acc_a == 1 || acc_aa == 1);
      % Starting values of interation
      phi_1 = atan((1-a_1)./((1+aa_1).*(tsr)));
      F_1 = (2/pi)*acos(exp(-((B/2)*(1-(r./R)))./((r./R).*sin(phi_1))));
      alpha_1 = phi_1-theta_p;

      w = 1;
      while (w <= length(alpha_1))
          x = 1;
          diff = 1;
          while (x <= length(alpha_data))
              diff = (alpha_1(w)*(180/pi))- alpha_data(x);
              if (abs(diff) <= .25)
                  Cl_1(w) = Cl_data(x);
                  Cd_1(w) = Cd_data(x);
                  element = x;
              end
              x = x + 1;
          end
          w = w + 1;
      end
```

```
    Ct_1 = (sol.*((1-a_1).^2).*((Cl_1.*cos(phi_1))+(Cd_1.*sin(phi_1)))./((sin(phi_1).^2));

    % Values after iteration
    q = 1;
    while (q <= length(Ct_1))
        if (Ct_1(q) < 0.96)
            a_2(q) = 1/(1+((4*F_1(q)*(sin(phi_1(q))^2))/(sol(q)*Cl_1(q)*cos(phi_1(q)))));
        end
        if (Ct_1(q) >= 0.96)
            %fprintf('Ct_1 > 0.96\n');
            a_2(q) = (1/F_1(q))*(0.143 + sqrt(0.0203 - (0.6427*(0.889-Ct_1(q)))));
        end
        q = q + 1;
    end

    aa_2 = 1./(((4*F_1.*cos(phi_1))./(sol.*Cl_1))-1);

    acc_a = 0;
    acc_aa = 0;
    t = 1;
    while (t <= length(Ct_1))
        diff_a(t) = abs(a_2(t)-a_1(t));
        if (diff_a(t) > 0.1)
            acc_a = 1;
        end
        diff_aa(t) = abs(aa_2(t)-aa_1(t));
        if (diff_aa(t) > 0.1)
            acc_aa = 1;
        end
        t = t + 1;
    end

    if (l > 10)
        acc_a = 0;
        acc_aa = 0;
    end
    l = l + 1;

    if ( acc_a == 1 || acc_aa == 1)
        a_1 = a_2;
        aa_1 = aa_2;
        %fprintf('test   ');
    end
    %fprintf('Iteration\n');
end

% Power Coefficient
ro = 0.036127;
o = hub_index;
Cp = 0;

while (o <= length(a_2))
    Cp_element(o) = ((8*(TSR/N))/(TSR^2))*(F_1(o)*(sin(phi_1(o))^2))*...
                (cos(phi_1(o))-(tsr(o)*sin(phi_1(o))))*...
                (sin(phi_1(o))+(tsr(o)*cos(phi_1(o))))*...
                (1-(Cd_1(o)/Cl_1(o))*cot(phi_1(o)))*(tsr(o)^2);
```

```
        Cp = Cp + Cp_element(o);
        o = o + 1;
    end

%% Blade Analysis
    % Relative Wind Velocity [in/s]
    Urel = U*((1+(tsr.^2)).^(1/2));

    % Density of Salt Water [lb/in^3]
    ro = 0.037030474;

    m = hub_index;
    L_total = 0;
    D_total = 0;
    while (m <= length(r))
        % Lift Force [lb]
        L(m) = Cl*((1/2)*ro*(Urel(m)^2)*((R/N)*c(m)))*(1/386);
        L_total = L_total + L(m);

        % Drag Force [lb]
        D(m) = Cd*((1/2)*ro*(Urel(m)^2)*((R/N)*c(m)))*(1/386);
        D_total = D_total + D(m);
        m = m + 1;
    end

%% Torque
    y = 6;
    while (y <= N)
        % Tangential Force
        Ft(y) = (L(y)*sin(phi(y)))-(D(y)*cos(phi(y)));
        %fprintf('Ft = %f\n', Ft(y));
        %fprintf('L = %f\n', L(y));
        %fprintf('D = %f\n', D(y));
        %fprintf('phi = %f\n', phi(y));

        y = y + 1;
    end

    y = 6;
    T_total = 0;
    while (y <= N)
        % Torque
        T(y) = Ft(y)*r(y);
        T_total = T_total + T(y);
        %fprintf('T = %f\n', T(y));
        %fprintf('r = %f\n', r(y));

        y = y + 1;
    end

    % Brake Force
    y = 1;
    while (y <= 20)
        Fb(y) = (6 * T_total)/y;
        y = y + 1;
    end
```

```
%% Results

  % Outputs chosen airfoil profile
  fprintf('************************\n');
  fprintf('****  %s  ****\n', profile);
  fprintf('************************\n\n');

  % Outputs chosen operating parameters
  fprintf('Parameters\n');
  fprintf('=========================================\n');
  fprintf('Radius of Rotor [inch]      %4.1f \n', R);
  fprintf('Radius of Hub [inch]        %4.1f \n', hub);
  fprintf('Number of Blades            %4.1f \n', B);
  fprintf('Tip-Speed-Ratio             %4.1f \n', TSR);
  fprintf('Flow Velocity [knots]       %4.1f \n', U_knot);
  fprintf('Reynolds Number             125,000\n');
  fprintf('=========================================\n\n');

  % Outputs optimal blade shape and theoretical performance
  fprintf('Blade Shape and Performance\n');
  fprintf('=================================================================\n');
  fprintf('Radius    Chord        Angle of          Section         Power\n');
  fprintf('[inch]    [inch]     Relative Flow     Pitch Angle Coefficient\n');
  fprintf('-----------------------------------------------------------------\n');
   m = hub_index;
   while (m <= N)
       fprintf('%4.1f       %5.2f        %5.2f         %5.2f      %.4f\n',...
       r(m),c(m),phi_deg(m),theta_pdeg(m),Cp_element(m));
       m = m + 1;
   end
  fprintf('-----------------------------------------------------------------\n');
  fprintf('                Total Power Coefficient of Blade ---> %.4f\n', Cp);
  fprintf('=================================================================\n');

   if (l > 10)
     fprintf('                                Stopped After 10 Iterations\n');
   end

  % Outputs lift and drag forces per blade element
  fprintf('Lift and Drag Forces on Blade Elements\n');
  fprintf('=============================================================\n');
  fprintf(' Chord     Angle of    Rel.Veloctiy   Lift Force   Drag Force \n');
  fprintf(' [in]    Relative Flow    [knots]        [lbf]       [lbf] \n');
  fprintf('-------------------------------------------------------------\n');
   m = hub_index;
   while (m <= N)
       fprintf('%5.2f        %5.2f       %6.2f      %7.2f      %5.2f \n',...
       c(m),phi_deg(m),Urel(m)/(1.687810*12),L(m),D(m));
       m = m + 1;
   end
  fprintf('-------------------------------------------------------------\n');
  fprintf('            Total Forces --->  %7.2f   %5.2f\n', L_total, D_total);
  fprintf('=============================================================\n');
```

```
% Outputs torque created from lift and drag forces
fprintf('Lift Forces and Torque on Blade Elements\n');
fprintf('=================================================================\n');
fprintf(' Radius     Angle of     Lift Force    Torque \n');
fprintf(' [in]    Relative Flow     [lbf]      [lbf-in] \n');
fprintf('-----------------------------------------------------------------\n');
 m = hub_index;
 while (m <= N)
     fprintf('%5.2f        %5.2f        %6.2f       %7.2f       \n',...
     r(m),phi_deg(m),L(m),T(m));
     m = m + 1;
 end
fprintf('-----------------------------------------------------------------\n');
fprintf('    Total Forces --->     %7.2f      %5.2f\n', L_total, T_total);
fprintf('=================================================================\n');

% Outputs braking force needed at various moment arms
fprintf('\nBrake Force At Varying Radii\n');
fprintf('============================================================\n');
fprintf(' Radii From COR      Brake Force \n');
fprintf('     [inch]            [lbf] \n');
fprintf('------------------------------------------------------------\n');
 m = 1;
 yy = 0;
 while (m <= 20)
     yy(m) = m;
     fprintf('%10.2f        %12.2f \n', yy(m),Fb(m));
     m = m + 1;
 end
fprintf('============================================================\n');
```

Structural Analysis

of Hydrokinetic Turbine Blades

December 9, 2010

Nathaniel Allen
Patrick Kilar
Brian Roy

Scope

Nate Allen, Pat Kilar and Brian Roy are all members of the TECH 797 Hydrokinetic Turbine senior design project. As a group we are in the process of designing a new more efficient version of last year's first generation turbine featuring Variable Flux Generation (VFG). One of the major components being redesigned to increase efficiency is the rotor, and more specifically the rotor blades. The efficiency of the rotor has been optimized by designing new blades containing both twist and taper along the length of the blade. However, one design constraint of the blades that has not been considered in the optimization is their structural integrity or the blades ability to function without failure in their implementation environment and conditions. The most efficient blade design is not good if it fails during normal operation conditions, and therefore to fully accurate design the rotor blade the structural dependability must be considered.

Although the free stream current of the ocean may be assumed constant for the analysis, the relative speed of the ocean current increases along the radius of the blade due to the increase in tangential speed of the blade towards the tip. Considering the force acting on the blade is proportional to the square of the velocity, as the relative velocity increases from base to tip, so does the net lift and drag forces on the blade, leading to a varying force distribution on the blade.

To quantify the effects of this type of force distributions, Finite Element Analysis (FEA) software will be utilized. From our design optimization, the NACA 44 series airfoil was chosen as the most efficient blade profile. Five different blade designs will be analyzed, all having a NACA 44 series profile and a percent cord thicknesses varying from 12 to 24 percent. The objective of the FEA structural analysis is to determine an acceptable airfoil thickness for each radial location on the blade. The FEA analysis will yield stress and displacement relationships along the length of the blade which can be used to draw conclusions on our design objective of designing an efficient yet structurally sufficient blade.

As mentioned above each blade will experience a distributed load of lift and drag forces along its length. This type of loading can be accurately modeled as a cantilevered beam, with the base of the foil fixed and the loads applied throughout the unsupported length of the blade. To predict the resulting lift and drag forces applied to the surface of the blades, the following equation

$$F_{(L,D)} = C_{(L,D)} A_p \frac{1}{2} \rho U_{rel}{}^2 , \quad (1)$$

was used at each designated blade element. This equation is dependent on the planform area (A_p) of the blade element which is the product of the elements chord and length, the density of the fluid medium (ρ) in our case sea water, the relative flow velocity (U_{rel}), as well as the Coefficient of lift (C_L) or drag (C_D) depending on the force being solved. From this equation an accurate prediction of the net lift and drag forces distribution experience by the blade can be found.

In order to accurately determine the distribution of the applied loads, each blade was divided into sectional elements. The resulting lift and drag forces will then be applied to outer edge each blade element, modeling each element as a cantilevered beam with a point load at its tip. With these loads applied to every blade element, the blade assembly as a whole will be a cantilevered beam fixed at its base with a distributed force acting on it its length. This model will them be

used to run FEA simulations for the applied loading and the resulting stress and displacement plots will be used to identify the structural stability of the blade designs having different thicknesses.

Implementation

As previously stated, A MATLAB program was used to optimize the efficiency of the blade shape, ultimately resulting in a unique taper and twist for each of the five blade designs. In order to accurately design a three dimensional (3-D) model of each blade, the calculated chord lengths from the efficiency program were used. From these chord lengths x and y coordinates for the specific airfoil profile used where determined for each blade element. Fifteen profiles for each blade were designed, forming a total of fourteen blade elements. From the design constraint of a 21 inch blade length, the resulting length of each element was 1.5 inches.

The most desirable Finite Element Analysis software was determined to be SolidWorks due to its ability to create the necessary complex shapes and user familiarity. SolidWorks enables its user to easily design a three dimensional models and assign important physical properties, enabling a highly realistic simulation. Using this computer modeling software, each element was designed separately to allow a surface to be referenced for the application of lift and drag forces. Using the two profiles associated with each element, a loft was used to form the contour of the element. To allow the application of the forces a reference point was sketched on the outer surface each blade element. The resultant lift and drag forces on an airfoil profile act through the axis of rotation defined at the quarter chord profile. Once the formation of all elements was finalized, five assemblies were made forming the three dimensional representations of the turbine blades. These assemblies were then constrained and assigned material properties which would allow for stress and displacement analysis through each blade. Acting as a cantilever beam, each blade was constrained with a fixed base and loaded appropriately with lift and drag forces acting along the quarter chord of the blade profile. The material used for the analysis of all five blade designs was a heat treated 6061-T6 aluminum alloy. This material is ideal for the final design because of its structural properties and physical properties making it ideal for a marine environment.

Assumptions had to be made in order to account for any possible differences between the simulation and validation testing. The number of elements, and therefore the number of forces applied, directly influences the accuracy of the applied load on the blade. The relatively small number of elements used to design each blade did not allow for a highly accurate uniform distributed load; however it was enough elements to generally describe the load variation. Therefore the stresses and displacements represented by the simulation will not have precise values with respect to a validated test under the same conditions. Similarly, because of the method involved in the formation of elements for each blade, the blade takes a linear sectional profile instead of a splined curve that would be associated with the higher precision calculation of a greater number of elements throughout the blade length. This approximation of the chord at a given point along the blade, while not drastic, does have an impact on the sectional area that opposes the applied forces distributed along the blade.

Validation

As mentioned previously, the blades were modeled as cantilever beams fixed at their base with a point loads applied along their length. It is good check for consistency to physically emulate the simulations as close as possible (material, loading and boundary conditions) to quantify the simulations validity in producing reasonable results. Being the second generation hydrokinetic turbine, last year's blade being a NACA 0012 extruded aluminum airfoil was readily available. To experimentally test the blade, it was fixed to a table top at one end while the rest of the blade was unsupported to simulate cantilever beam loading. Further a 6 lb force was applied 18" inches from the supported end. It was assumed that the c-clamp perfectly fixed the base of the blade, the blade was initially perfectly horizontal and the load applied perfectly vertically 18" inches from the supported end. To measure the deflection of the tip when a force was applied a micrometer was used to measure both the loaded and unloaded position. The micrometer is assumed to be an acceptable instrument because it measures in the thousands of an inch similar to the computer simulation data. In order to validate our modeling technique, we created a SolidWorks model of the NACA 0012 blade having the exact same material, profile, chord and length as the blade tested. The boundary conditions and loads were also applied to the model in the same fashion as they were applied during the experimentation. Figure 1 below depicts the SolidWorks model of the NACA 0012 blade. In this picture the fixed boundary condition is shown by green arrows and the applied 6 lb_f load is shown in purple.

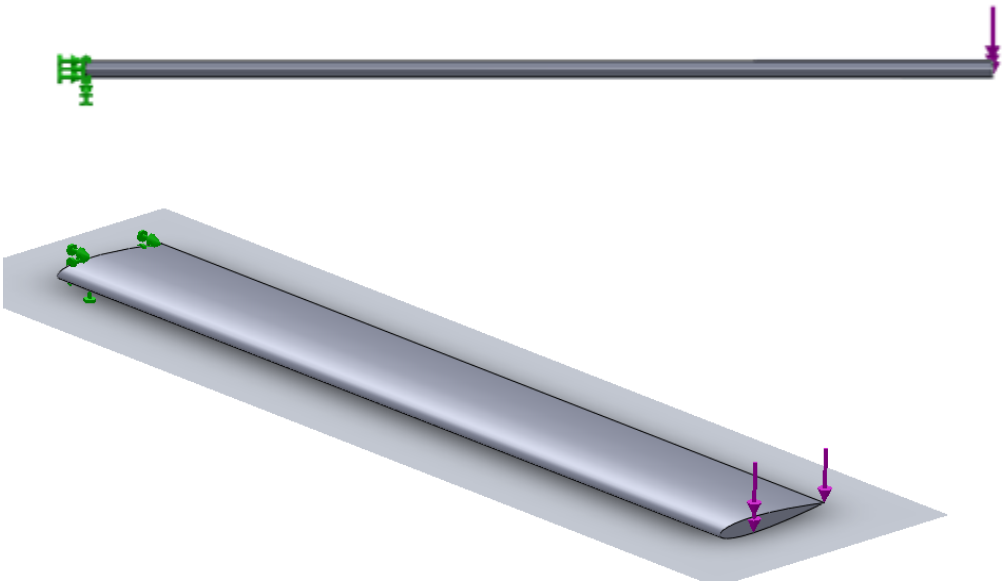

Figure 1:
SolidWorks model of the NACA 0012 blade depicting a fixed boundary condition and a 6 lb_f load, shown by green and purple arrows respectively.

The NACA blade was modeled by lofting between two sketches, the same method used to create the 44 series blades. The NACA blade material tested was 6063-T6 aluminum which was also defined as the material property within the model. Compared to the 44 series blades the NACA blade had no twist, and the forces were not applied at various angles. However the SolidWorks model shown in Fig. 1 is similar in length, type of cantilevered loading, boundary conditions, meshing, and material. Considering these similarities between our actual blade models and this

simplified validation model, it was assumed to be a good approximation for validation. If the experimental test results are close in magnitude to the results from the FEA simulation, then the method for analyzing the blades will be validated.

Figure 2 below shows the displacement results of the FEA simulation. In this figure, the color bar on the right depicts magnitudes of relative displacements in inches. Red and blue colors correspond to the maximum and minimum displacements respectively. Using the probe tool the displacement of a node can be displayed anywhere along the blade. It was found the maximum displacement observed at the tip of the blade was 0.304" inches.

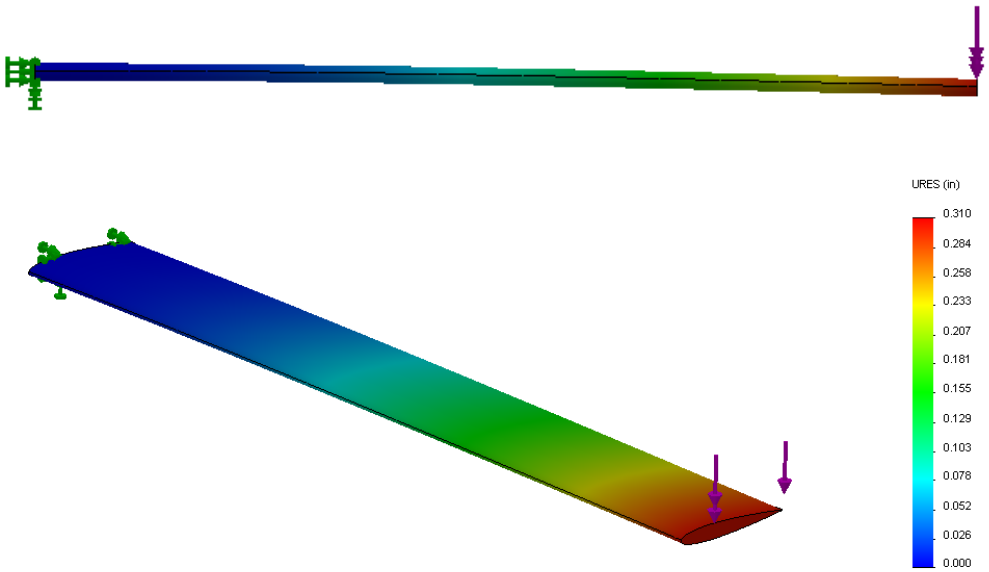

Figure 2:
FEA results for the displacement of the NACA 0012 validation blade.
The color bar on the right depicts magnitudes of displacements in inches of deflection.

In the experimental tests the maximum deflection measured was 0.384"inches at the tip of the blade. Table 1 below compares the deflection from FEA simulation to the experimental test results. The percent difference between the simulation and experimental analysis was calculated to be 26.3% or 0.08" inches. The actual difference between the two methods is very small and easily attributed to error induced by our assumptions made such as the blade not being perfectly horizontal hindering our micrometer readings and the force not applied perfectly vertical exactly 18 inches from the base. In conclusion, the displacement results acquired from our experimental test validate this type of model, loading, boundary conditions, and meshes.

Table 1:
Validation results of FEA, and Experimental deflection and their corresponding percent difference.

Validation Results	Value
FEA Deflection	0.304
Experimental Deflection	0.384
Percent Difference	26.3

Note: Units of deflection are inches.

Analysis

Fixed at its base and unsupported along the rest of its length each blade was modeled as a cantilever beam being loaded by lift and drag forces along its length. In order to get a more accurate loading along the blade, each blade was discretized into 14 elements. The resultant lift and drag forces can be modeled to act at a quarter chord of the blade profile. These forces will act parallel and perpendicular to the angle of relative flow. The corresponding lift and drag forces were quantified for each blade element using Eq. 1 above. It was found that each element along that blade had a unique lift and drag force acting on it. The lift forces on each element for the 5 blades at a maximum flow speed of 6 knots are shown below in Table 2.

Table 2:
A chart of the lift forces applied to each of the 14 elements along the blades.

Element	Radial Distance @ Application [inch]	Lift Force [lb_f]	Angle of Relative Flow [deg]
1(Base)	1.5	11.7	30.48
2	3.0	13.05	27.76
3	4.5	14.41	25.41
4	6.0	15.77	23.37
5	7.5	17.15	21.61
6	9.0	18.53	20.07
7	10.5	19.92	18.71
8	12.0	21.33	17.52
9	13.5	22.74	16.46
10	15.0	24.15	15.52
11	16.5	25.58	14.67
12	18.0	27.01	13.90
13	19.5	28.44	13.21
14 (Tip)	21.0	29.88	12.58

Note: Lift Force acts perpendicular to angle of relative flow and drag force acts parallel.

The total corresponding lift force acting on the blades was determined to be 300 lb_f,. The drag force on the blades was almost negligible in comparison and accumulated to a total force of less than 3 lb_f. Figure 3 below, depicts one of the 44 series blades with its respective loading; fixed base and lift and drag forces applied to the outer edge of each element. The boundary condition is depicted by the green arrows and the loads are indicated by the purple arrows.

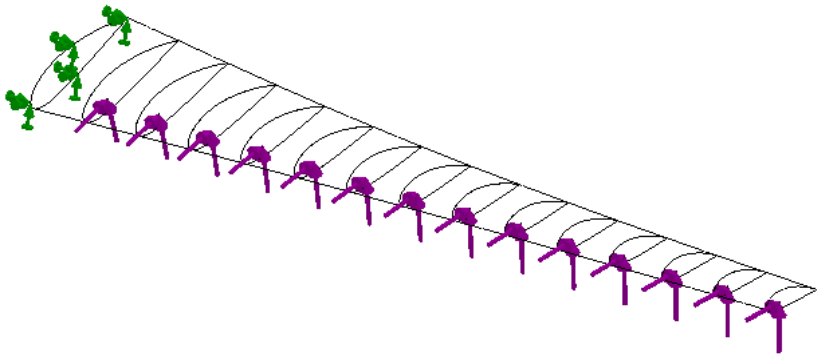

Figure 3:
SolidWorks model of a NACA 44 blade with prescribed loading conditions. The green arrows depicted a fixed boundary condition while the purple arrows represent the lift and drag forces applied at each blade element.

To achieve accurate results for the blade, it was subdivided into many small three dimensional elements. The FEA elements used were tetrahedral elements which each have 4 nodes and 12 possible degrees of freedom. Subdividing each of the 14 blade elements into a mesh of many small FEA elements will produce fairly accurate results of how the blade will actually deflect. Another key aspect of using three dimensional FEA elements is their ability to display the deformed shape after the analysis, making it easier to visualize the deflection being experienced.

To identify the optimal mesh resolution, i.e. the tetrahedral element size, different meshes were analyzed and the accuracy of the results where compared. Figure 4 below displays two finite mesh examples, a course mesh and a fine mesh the left and right pictures respectively. The mesh shown on the left of the figure is a course mesh that was initially tried. This mesh contained approximately 15,000 nodes and 10,000 tetrahedral elements each with a 10.3 mm element size. This mesh was later found to give us inaccurate results. One reason for this is because the mesh on the top and bottom surface is reasonably fine for the size of the foil, however, when looking at the profile of the blade, the mesh only consisted of 1 or 2 elements throughout the thickness of the blade, which does not give very good resolution for the stress distribution throughout the thickness of the blade.

Based on this finer and finer meshes were analyzed until a suitable mesh was determined that was fine enough to give accurate results, but so fine that it took hours to simulate. The suitable mesh chosen is shown on the right in Fig. 4 below. This mesh contained roughly 80,000 nodes and 50,000 elements each with an approximate element size of 4.3 mm. As seen in the figure below, this mesh contained 5 or 6 elements throughout the thickness of the blade which allowed for more stress and displacement resolution within the blade, leading to more accurate results.

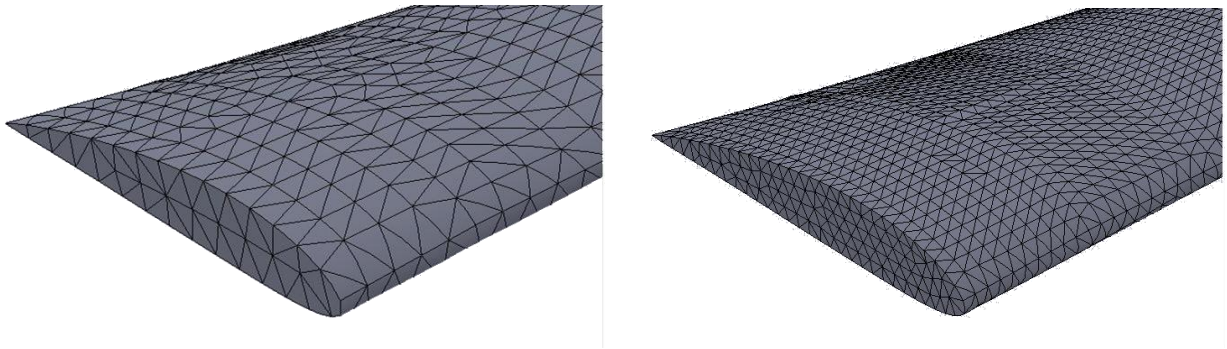

Figure 4:
A course and a fine FEA mesh of 3-D tetrahedral elements.
The mesh on the right was chosen as a suitable mesh to achieve accurate results.

One of the main criterions being evaluated to determine the structural integrity of the blade is its total deflection. Using the chosen mesh and material (6061–T6 Aluminum), as well as the boundary conditions and appropriate loads as described above, the FEA simulation was run and the resulting displacement of the element was plotted. Due to the twist of the blade, the unique cross section and the angle of forces, blades actually twist during deformation. However, because the lift force is the dominant load, only the total resultant displacements of the blade elements were considered. Consistent with a cantilevered beam theory, the maximum deflection in each blade was determined to be at the very tip. Table 3 below displays the maximum deflection at the tip for all 5 blades. From this table it is clear that as the thickness of the blades increases, the allowable displacement decreases. Overall, it was found that the blades had a considerable amount of deflection, however as will explain later the material is still well below yielding and therefore it is acceptable to experience this kind of deflection at the worst case, maximum load conditions.

Table 3:
Chart displaying the maximum deflection experienced in each blade due to loading.

Blade Number	Profile and Thickness of Blade	Max Resultant Displacement [inch]
1	NACA 4412 (12% thickness of chord)	1.277
2	NACA 4415 (15% thickness of chord)	1.156
3	NACA 4418 (18% thickness of chord)	0.971
4	NACA 4421 (21% thickness of chord)	0.882
5	NACA 4424 (24% thickness of chord)	0.687

Due to the attribute of using three dimensional finite elements, the displacements along the entire blade can be easily shown from viewing the deformed model of the blade. Fig. 5 below displays the deformed shape of all 5 blades on a scale of 1. The original shape/location of the blade is shown semi-transparently in the figure as well making it clear how much the blade deformed. The color bar shown at the right displays the resultant displacement of each node in inches. In the figure, the top blade corresponds the blade number 1 having a NACA 4412 profile and the other blades are in the same order given in the table above.

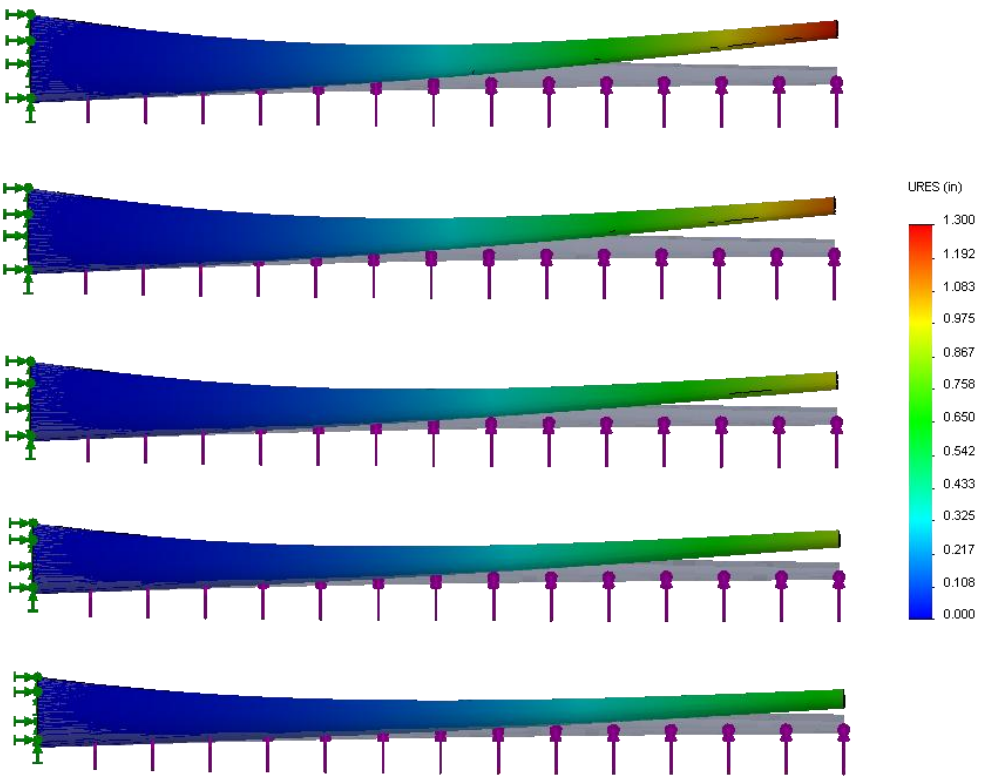

Figure 5:
Displays the deformed shape of all 5 blades, on a scale of 1. The color bar corresponds to the resultant displacement and is in inches. The blades are in the same order given in Table 3.

Fig. 5 above is a good visual representation of the actual deflection of the blade under loading. The figure above is a nice way to visualize the data given in Table 3. The thickest blade located on the bottom of the above figure clearly has the smallest deflection of all blades. Likewise, as the blade thicknesses decrease the deflection of the blade begins to increase, therefore having the largest deflection for the thinnest blade, blade number 1 (NACA 4412).

Another important factor that is crucial to the structural integrity of the turbine blades is the stress that develops due to loading and deformation. Because the blade is twisting and bending under loading, it will be experiencing normal stresses, bending stress and shear stresses in all three coordinate directions. Since there are so many stresses acting on the blades it is hard to identify the critical stress that should be considered. Do to this complexity it is reasonable to consider on the von Mises stress which is based on the von Mises-Hencky theory, also known as the Maximum distortion energy theory. The von Mises stress (σ_{vm}) is a combination of the three principle stresses (σ_1, σ_2, σ_3) and can be expressed as

$$\sigma_{vm} = \sqrt{\frac{(\sigma_1-\sigma_2)^2+(\sigma_2-\sigma_3)^2+(\sigma_1-\sigma_3)^2}{2}}. \quad (2)$$

The principle stresses will incorporate all the stress acting on the blade and because the von Mises stress is defined based on the principle stresses it is also based on the bending and shear stresses that the blade is experiencing. In addition to this, the theory states that a ductile material starts to yield at a location when the von Mises stress becomes equal to the yield strength of the material. This is why the maximum von Mises stress criterion is an ideal criterion to use when evaluating the stress within the blades.

Each of the 5 blades where simulated under the loading conditions and the resulting von Mises stress distribution within the blades was plotted. From these plots/figures the von Mises stress was evaluated against yielding and compared to the other blades to determine the relative magnitude of stresses in the blades. For all 5 blades a similar stress distribution was observed, which is what was expected considering the blades are form the same airfoil series and have similar twist and taper. Below in Fig. 6 is a plot of the von Mises stress distribution on the top edge of the second element for blade 1 (NACA 4412). This plot demonstrates the general trend that was found for all blades. This trend shows lower tresses on the blade edges and a high stress concentration near the center but offset slightly to the leading edge of the blade.

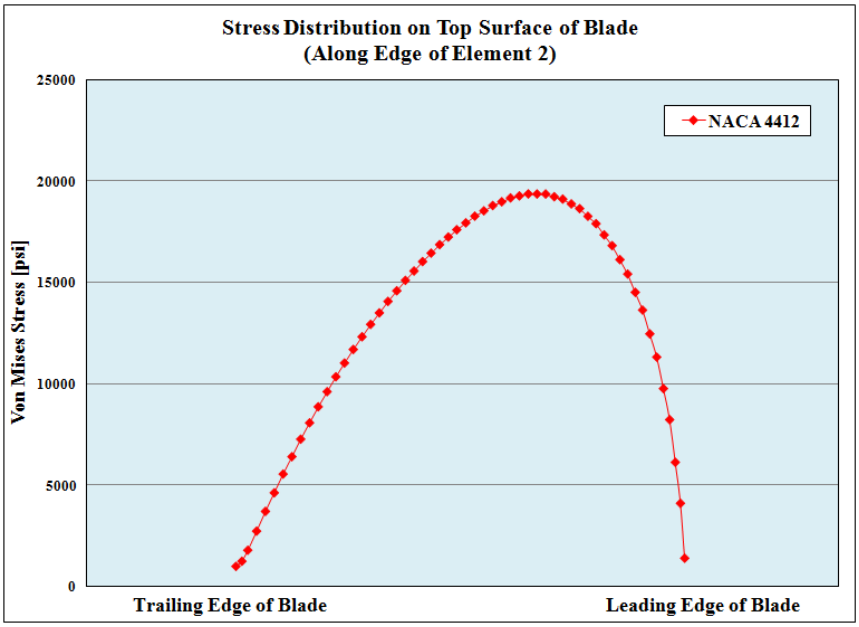

Figure 6:
Is a plot of the typical von Mises stress distribution seen on the top surface of all 5 blades. The nodes along one element edge are plotted for blade 1 (NACA 4412).

Another typical trend of all the blades was observed from the von Mises stress plots, which is the distribution of stresses along the length of the blade. For all blades it was found that the magnitude of stress was largest a few elements away from the base of the blade and the stress decreased from that point to the tip of the blade. This trend is depicted in Fig. 7 below, which plots the maximum stress observed in each element along the length of the blade. The maximum stresses plotted in Fig. 7 correspond to the "peak" stress points on the top surface of the element as shown above in Fig. 6. It is clear from the plot below that the relative maximum stresses experienced by the blade elements decreases as the blade thickness increases.

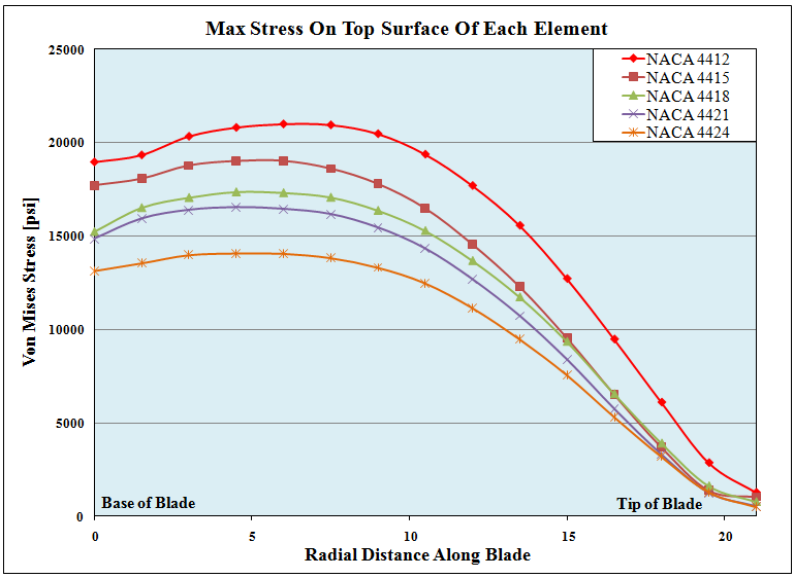

Figure 7:
Is a plot of the maximum von Mises stress of each blade element for all 5 blades.

Although trends like the two presented above are helpful in understanding the general characteristics of the stress, to fully visual and understand the entire stress distribution throughout the blade the resulting stress plots from the simulations must be considered. Fig. 8 below shows the von Mises stress distribution for all 5 blades from a top down view. The ranges of stresses are denoted by the color bar to the right of the blades and are given in psi. The blade on the far left is blade 1 which has a NACA 4412 profile. The blade profiles increase in thickness to the right in the same order as given above.

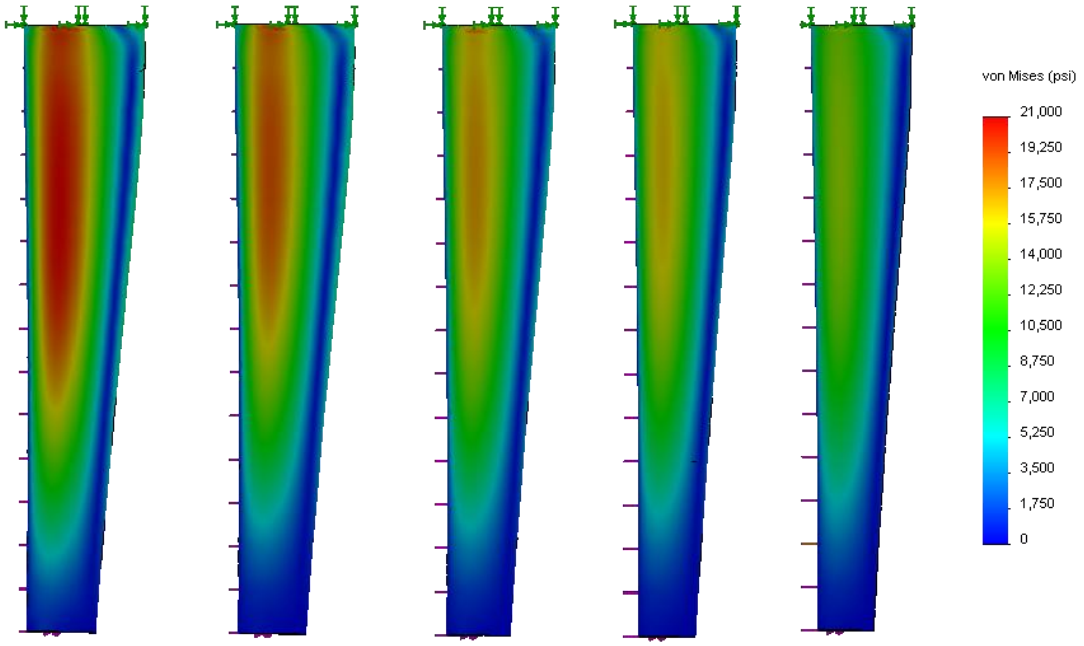

Figure 8:
Is the resulting von Mises stress distribution for the deformed blades after loading. The blades increase in thickness from left to right starting with blade 1 (NACA 4412).

From the above figure it is evident that all 5 blades exhibit similar stress distributions. They all have rather low stresses (blue region) at the tip of the blade and along the trailing edge, shown as the edge on the right. In addition to this all the foils have an increasing stress concentration towards the base of the blade and offset slightly toward the leading edge. All 5 blades are plotted against the same color scale, with red being the largest stress of 21,000 psi and blue being the least stress around 1,000 psi. Based on this it is clear the foil on the left has the largest stress concentration. This is to be expected considering that is the blade with the smallest thickness. The same trend as shown in the plot above is shown in Fig. 8. As the blade thickness increases the stress concentration being experienced is lessened. A similar trend shown on by these top view was experienced on the bottom as well, however the stress distribution is different and not as visually clear.

Although Fig. 8 nicely displays the actually stresses being experienced in the blades, it is unclear whether these stresses are acceptable or not. To evaluate the stresses in the blades, the maximum von Mises stress criterion as mentioned above was applied. The relative von Mises stress in the blades was dividing by the yield strength of the 6061-T6 aluminum alloy which results in the Factor of Safety (FOS) from yielding. For example a FOS of 2 means the stress experience is half of the maximum yield stress of the material before it fails. Below in Fig. 9, is a plot of the factor of safety from yielding distribution for all 5 blades. The blades are arranged in the exact same manner as where in Fig. 8.

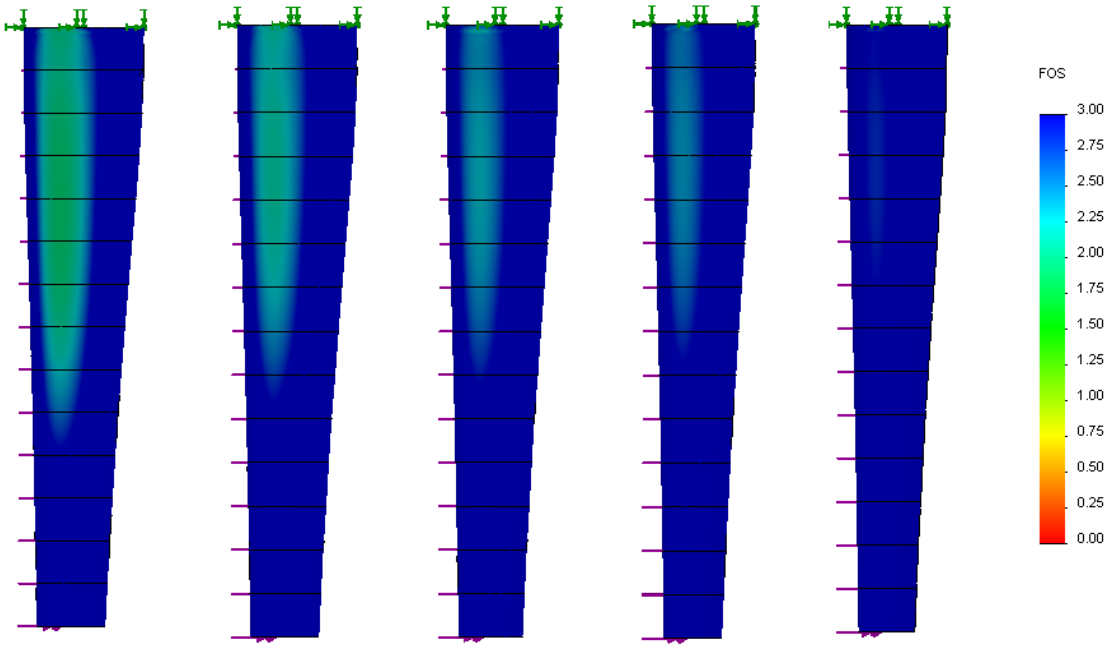

Figure 9:
Is the Factor of Saftey from yielding distribution for the deformed blades after loading. The Factor of Safety was base on the maximum von Mises stress criterion. The blades increase in thickness from left to right starting with blade 1 (NACA 4412).

The blades shown above have the same general trend, which is expected because Fig. 9 was generated by dividing the stress at every point of the blade by the yield stress of the material and

then plotting that value instead of the stress magnitude. A general rule of thumb for a conservative design is to use a FOS of 3. The blades above are all plotted against a scale from 0 to 3 FOS, with the dark blue color corresponding to a FOS of 3 or higher, due to the limitation of the scale. By comparison of all 5 blades, it is clear that at the base of the thinner blades the factor of safety from yielding decreases and is slightly less than 2 for blade 1 (NACA 4412). Using the FOS plot is a good way to compare stresses in the blades because the exact value of the stresses in the blade are far less important than the knowledge how close that stress is to yielding.

Conclusion

The initial objective of this project was to determine an acceptable blade profile and thickness for each element along the blade to come up with a blade having ideal structural integrity and performance. Based on the deflection results, von Mises stress results, and the FOS results it can be determined which blades/profiles are acceptable for which elements. The displacement results give a more generalized blade result; however the characteristic found can be directly applied to the determination of our final design. From the displacement it was clear that the thicker the blade the less the blade deflects. Increasing the thickness from 12 to 24 percent decreased the deflection by almost half. Therefore an ideal blade would have minimal deflection, meaning a thicker blade is desirable, especially at the base where most of the bending occurs.

The von Mises stress and FOS results are both plots of the same thing and can best be used in conjunction. From the results of the von Mises stress shown in Fig. 8, it was determined that the stress concentration in the blade was minimized by increasing the thickness of the blade. However, from the top view of the blade it was also clear this was mostly important towards the base of the blade and not the tip. Based off of this, the FOS plot can then be used to identify which blade profile would be acceptable at which element. For an initial conservative design a FOS of close to 3 would be optimal. Therefore, the only blade profile that fully achieves a FOS of 3 near the base is the thickest blade with a NACA 4424 profile. For the elements in the middle region of the foil, a thinner profile can be acceptable especially as you approach the tip region. At the tip it was found that even the thinnest blade with a NACA 4412 profile maintained a factor of safety of 3 or greater.

Drawing the conclusions from all three, the one possible ideal blade design might consists of the NACA 4424 profile for the first 4 elements, then the NACA 4418/4421 for the next 3 elements, then the NAVA 4415 for the next 4 elements and lastly the NACA 4412 profile for the final 3 elements. This design will have a reduced deflection and reduced stress concentration due to the thicker profiles at the base, and will also have the more efficient thinner profiles at the tip where most of the power is extracted. This is one possible configuration and further analysis and parameters will be considered to choose the final blade design.

The 21 inch blades were broken up into 14 elements each 1.5 inches in length. This subdivision is fairly course and therefore will not yield the most accurate results possible; however, it is enough elements to give a reasonable first order estimate of the overall deflection and stresses in the blade. The biggest factor leading to inaccuracy of our model is the application and distribution of the loads. Firstly the net lift and drag forces are continually changing throughout

the radial location on the bade and therefore a more accurate force distribution could have been achieved using more elements, however, once again 14 elements did allow for varying load to be applied resulting in decent first order results. The main inaccuracy of our model however, came from the type and application of the loads. On a real turbine blade, or airfoil for the matter, the net lift and drag forces are due to the difference in pressure distribution over the profile of the blade. Therefore the most accurate simulation of these loads would be a surface load with the carrying characteristics of the pressure distribution instead of applying the net resultant forces as point loads acting through a quarter chord (inside the blade).

Improvements to the model and loads could be done to allow for more accurate results to be calculated. In addition to this loads for different flow speeds could also be analyzed to see if the same type trends are found. Considering the current model and loads are accurate enough further analysis could be done to determine an optimal arraignment of profiles for each element, similar to the design presented above. For this, a composite blade model consisting of different profiles for different elements could be made and then analyzed with the appropriate loads to determine if the simulation yields the expected results from this initial analysis or if the characteristics change due to varying thicknesses.

Appendix

End view of blades aligned in order 1 through 5 displaying how the thickness of the blade profile changes between blades.

View of the entire blade with the chosen FEA mesh.

UNIVERSITY of NEW HAMPSHIRE

Course Number and Name: ME 747: Experimental Measurement and Modeling of Complex Systems	
Semester and Year: Fall 2010 Semester	**Name of Lab Instructor:** Professor Barry Fussell
Lab Section and Meeting Time: Section 03: Wednesdays 2:10-5:00pm	**Report Type:** External (Group)
Title of Experiment: **Implementation of a Rotational Speed Measuring Device**	
Date Experiment Performed: December 6-11, 2010	**Date Report Submitted:** December 17, 2010
Names of Group Members: Nate Allen Shane Baia Chris Carrier Pat Kilar	**Grader's Comments:**
	Grade:

Hydrokinetic Energy LLC.
33 Academic Way
Durham, NH 03824

December 17, 2010

Dr. Barry Fussell
University of New Hampshire
Kingsbury Hall
33 Academic Way
Durham, NH 03084

Dear Dr. Fussell,

We are submitting the attached report entitled *Implementing of a Rotational Speed Measuring Device.*

The following report on the laser-tachometer sensor will describe how its calibration curve and time constant have been quantified along with how it performs at measuring different revolutions per minute (RPM) at different distances, angles, and through different mediums. To emulate the rotor, the experimental setup from Lab 6 was retrofitted such that a cardboard disk with 6 tick marks for the laser sensor was attached to the end of the motor shaft. The report details the laser-tachometers calibration curve, its optimal distance and angle from the rotor as 3-6 inches oriented at 15 degrees, its approximate speed of response, and how passing through different mediums has negligible effects on its ability to quantify the rotational speed. Such results imply this laser sensor is a suitable candidate for rotational speed measurements of the hydrokinetic turbine.

This report has validated the use of this laser sensor which I hope will lead to its successful implementation on the second generation hydrokinetic turbine.

Sincerely,
Patrick Kilar, Co-Founder
Hydrokinetic Energy LLC.

Encl: *Implementation of a Rotational Speed Measuring Device*

Table of Contents

List of Figures

List of Tables

Objective

[Chris Carrier]

The ability of a rotational speed measuring device to accurately measure rotational speed of a rotating disk was investigated using various distances, angles and mediums. This experiment will determine if a rotational speed measuring device is capable of being implemented on a hydrokinetic (underwater) turbine featuring Variable Flux Generation (VFG). As this type of turbine has a rotor that is variably displaced axially with respect to a fixed stator, traditional measuring devices are not applicable. This laser sensor will measure the rotational speed by shooting a laser from the fixed stator to the rotor. The rotor contains 6 reflective spots which the device senses as they cross the path of the laser.

The purpose of the experiment is to identify if the chosen laser tachometer will be able to accurately measure the rotational speed of the rotor. In this experiment the sensor's output rotational speed will be measured and compared to that of a pre-calibrated tachometer. The sensor will be tested for various rotational speeds and rotor displacements as well as transient rotational speeds. The sensor will also be validated for a marine application by implementing the sensor through a medium of sea water. The accuracy of these results will then be used to calibrate the sensor and to validate whether this device can be implemented for this scenario.

Summary of Results

[Shane Baia]

Overall, the laser optical rotational measuring device proved to be sufficiently accurate for its intended application. In order to properly compare the laser-tachometer's output to that of the motor-tachometer, the motor-tachometer first had to be calibrated. From this calibration, the sensitivity of the motor-tachometer was found to be 0.00302 volts/RPM. The laser-tachometer was then calibrated and found to have a sensitivity of .00967 volts/RPM which was slightly lower than the manufacture's indicated sensitivity of 0.01 volts/RPM.

When testing the accuracy of the device at varying distances, it was found that the device is inaccurate for distances less than 3 inches and is accurate to at least 48 inches. The percent differences of the laser-tachometer's measured rotational speed compared to that of the motor-tachometer's is seen below.

X (in)	% Difference	X (in)	% Difference	X (in)	% Difference
0.5	63.016	3	0.323	12	0.784
1	27.038	4	0.714	24	0.739
1.5	29.310	5	0.451	36	0.858
2	0.418	6	0.431	48	0.827

A rotational speed transient of both decreasing (set 1) and increasing (set 2) speeds were measured by both tachometers. The measured responses from the laser-tachometer were then compared to that of the motor-tachometer. The measured time constants from the laser-tachometer were all within 9% of those measured from the motor-tachometer as seen below. This percentage equates to less than 0.01 seconds which for the intended application can be considered negligible.

			Time Constant		
Set	**Trial**	**Transient Type**	$(\tau)_m$	$(\tau)_L$	**% Difference**
1	1	Decreasing	0.878	0.933	6.264
	2	Decreasing	0.886	0.9627	8.657
	3	Decreasing	0.931	0.986	5.908
Average			**0.898**	**0.961**	**6.479**
2	1	Increasing	0.7314	0.8008	9.489
	2	Increasing	0.797	0.867	8.783
	3	Increasing	0.6881	0.7379	7.237
Average			**0.739**	**0.802**	**7.865**

NOTE: Subscripts L and m represent values measured by the laser and motor respectively

Lastly, to emulate the underwater environment, the device was tested through several mediums and at various angles with respect to the rotating cardboard rotor. The results from these trials are displayed in the following three charts below. The optical laser sensor proved accurate through both the Lexan and saltwater mediums, and therefore was validated to be implemented successfully on the VFG Turbine later next semester.

AOA = 0 deg			
Medium	**$(RPM)_L$**	**$(RPM)_m$**	**% Difference**
Air	290.41	288.29	0.737
Lexan	278.94	277.02	0.691
Lexan & Water	287.83	285.64	0.767

AOA = 15 deg			
Medium	**$(RPM)_L$**	**$(RPM)_m$**	**% Difference**
Air	290.31	287.96	0.817
Lexan	290.52	288.29	0.773
Lexan & Water	299.82	297.90	0.646

AOA = 45 deg			
Medium	**$(RPM)_L$**	**$(RPM)_m$**	**% Difference**
Air	284.31	281.99	0.823
Lexan	294.55	292.27	0.781
Lexan & Water	293.62	291.27	0.806

NOTE: Subscripts L and m represent values measured by the laser and motor respectively

Experimental Methods

The hydrokinetic turbine will be emulated using a DC motor and a cardboard circle attached directly to its shaft. The DC motor will spin the cardboard circle which will act as the rotor and the rotational speed will be measured by the optical laser sensor. For this, a 12 inch cardboard disk was cut out and reflective tape was placed at 6 locations symmetrically about the center and concentrically coupled to the shaft of the DC motor.

The DC motor will be driven using a National Instruments (NI) function generator, however to drive the motor the signal must first be sent through a power op-amp. The power op-amp used in the experiment is shown in the following figure.

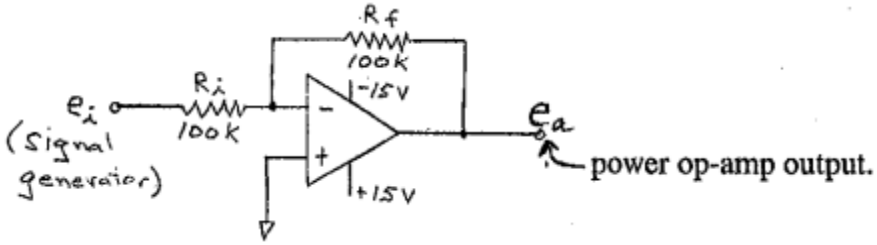

Figure 1:
Electrical diagram of the power op-amp used to drive the DC motor.

The output signal from the function generator (e_i) was then wired to the appropriate location on the power op-amp as shown above. The op-amp was then powered with ±15 V signal from a National Instruments (NI) power supply. The output from the power op-amp was then wired to the positive and negative motor input leads as described in the experimental procedure. Lastly, the built in motor-tachometer was wired to the oscilloscope. For further guidance, refer to the Experimental Procedure located in Appendix-E.

The output signal from the laser sensor is a voltage pulse signal and therefore must be sent through a tachometer to convert it to a constant DC signal which will be proportional to the rotational speed of the rotor. The tachometer input and output leads are displayed in the following figure.

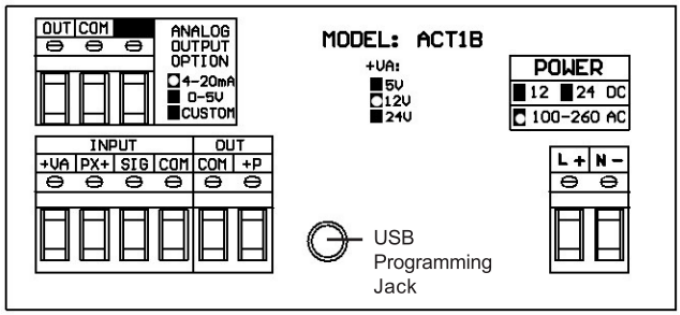

Figure 2:
Back Panel of ACT-1B Tachometer showing output and input wiring locations.

The ACT-1B tachometer was powered using a 12 volt DC signal with the NI power supply by wiring the leads to the L+ and N- locations shown in the above figure. Leads from the oscilloscope were then connected to the Analog Output ports on the tachometer. The laser sensor is then connected to the input panel on the tachometer wiring the blue, brown, black and shield wires to the corresponding locations on the back of the tachometer as shown in the figure below. For further guidance, refer to the Experimental Procedure located in Appendix-E.

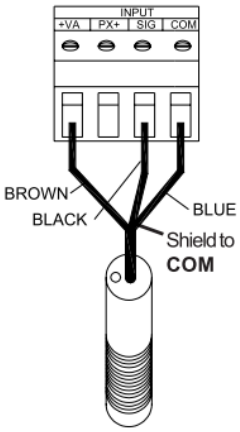

Figure 3:
Back Panel of ACT-1B Tachometer showing wiring diagram for optical laser sensor.

During initial testing of the laser-tachometer, it was discovered that its output signal was extremely noisy, such that the individual peaks were non-distinguishable. To correct this, a 741 op-amp was used to create a low-pass filter.

I. Speed Calibration of Sensor

[Chris Carrier]

The tachometer built into the motor is specified by the manufacturer to have a sensitivity of 0.003 ± 10%. To determine a more accurate sensitivity that can be used to determine the true RPM of the cardboard rotor, it must first be calibrated against a more accurate device. For this, an OMEGAETTE HHT-1501 portable tachometer with an accuracy of ± 0.1% was used. For 10 increments over the range of 0 to 500 RPM, the measured RPM from the portable tachometer were recorded as well as the average output voltage of the motor tachometer. These two values were then used to determine the true sensitivity of the device.

For the calibration of the laser sensor, it was positioned 3 inches perpendicular to the front of the rotating disk, and aimed at the reflective strips. This can best be described by looking at Figure I.1 below.

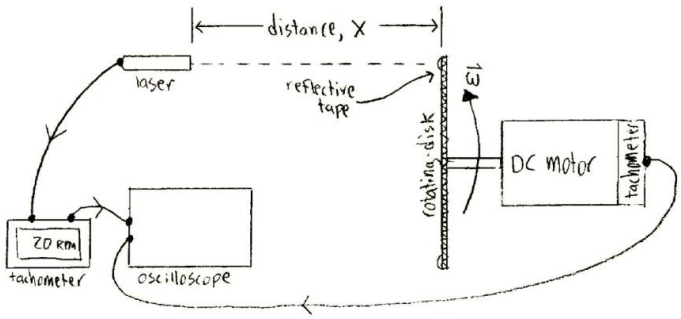

Figure I-1:
Experimental Setup for Calibration

With the laser sensor in the correct position, the rotational speed of the rotor was then varied over 10 increments between a range of approximately 0 to 500 RPM. The NI function generator was adjusted for a 1 mHz square wave. The amplitude of the square wave was varied from 0 to 4 volts at approximately 0.25 volt increments. The power supplies to the motor and laser-tachometer were enabled.

At each increment the average voltage output of both the motor-tachometer and the laser-tachometer were recorded. The average output voltage of the motor-tachometer was then converted to revolutions per minute (RPM) using the experimentally calculated motor-tachometer sensitivity determined from the motor calibration.

II. Distance Validation of Sensor

[Pat Kilar]

In this part of the experiment, the rotational speed of the disk will be fixed at a constant rotational speed (RPM) and the distance the optical laser is from the rotating cardboard rotor will be varied. To accurately position the sensor a certain distance from the rotor, a 60 inch strip of tape was adhered to the lab bench positioned such that it was approximately perpendicular to the cardboard rotor. With respect to the outside edge of the cardboard rotor the following increments were measured and marked on the tape: ½, 1, 1½, 2, 3, 4, 5, 6, 12, 24, 36 and 48 inches. These marks will indicate the various distances the laser will be tested at.

To set the cardboard rotor at a constant RPM, the NI function generator was adjusted to a 1 mHz square wave with an amplitude of 2.75 volts which corresponded to approximately 300 RPM. With the function generator set, the +15 and -15 volt signals from the NI power supply to the DC motor were enabled. In a similar fashion, the laser-tachometer was powered by enabling the 12 volt DC signal from the power supply. With the function generator set and all devices powered, the cardboard rotor should be spinning at an approximately constant rotational speed. With the rotor spinning, the laser was positioned at each mark, previously made on the tape. At each position the average output voltage from both tachometers was recorded using the oscilloscope. These voltages were then converted to an RPM using the sensitivities found during the calibrations done previous.

III. Transient Velocity Measuring

[Nate Allen]

For this part of the experiment, the rotational speed measuring device's response to transient rotational speeds will be tested. For this the laser sensor will be mounted at a fixed distance of 3 inches from the front of the cardboard rotor and will not change during the experiment. As in previous sections, the output voltages of laser-tachometer and the motor-tachometer were both wired to the NI oscilloscope. The oscilloscope was triggered to capture the step response of both the motor-tachometer and the laser-tachometer; however, the trigger was set using only the signal from the motor which is the most accurate and fastest to respond. With the trigger set, the NI power supplies for both the motor and laser-tachometer were enabled. Lastly, the transient or varying rotational speed will be generated using the NI function generator.

To account for any hysteresis in the laser sensor, both increasing and decreasing transient rotational speeds were tested. For the decreasing rotational speed transients, the function generator was set to have a 1 mHz square wave with an amplitude of 3.5 volts. This voltage input spins the cardboard rotor at approximately 400 RPM. To create a sudden change in the cardboard rotor's RPM, the voltage amplitude of the square wave in the function generator was changed to 1.5 volts and then applied. This sudden drop in voltage causes the DC motor to decrease its rotational speed until it reaches the correct speed for a 1.5 volt input which is approximately 100 RPM. Therefore, changing the motor's input voltage from 3.5 volts to 1.5 volts causes a transient decrease in rotational speed of the rotor from roughly 400 RPM to 100 RPM. This decreasing transient response was measure by both the laser sensor and the motor-tachometer and then stored on the oscilloscope. Three trials for the decreasing transient response were done, to ensure enough data to obtain accurate results.

For the increasing rotational speed transients, the same method was used; however the initial square wave voltage amplitude on the function generator was set to 1.5 volts and then was changed to 3.5 volts. This sudden increase in the motor's input voltage causes it to continually increase its speed until it reaches the appropriate RPM. Therefore, changing the motor's input voltage from 1.5 volts to 3.5 volts causes a transient increase in rotational speed of the rotor from roughly 100 RPM to 400 RPM. As done for the decreasing transient, this response was measured and stored three times for both the laser sensor and motor-tachometer.

IV. Validation for Marine Environment Implementation

[Shane Baia]

The laser sensor under test will ultimately be implemented in an underwater environment and will need to be waterproofed in order to do so. One proposed method of water proofing the device is by incasing it in a Lexan container which will act as a barrier between the laser and the surrounding water. However, the laser beam itself will have to travel through the layer of Lexan, followed by several inches of seawater, and back through the Lexan to the sensor. Before this setup could be implemented, the accuracy of the laser sensor needed to be tested under similar circumstances. To simulate the predicted operating conditions, the laser beam will be set up to pass through a Lexan container filled with seawater in order to measure the rotational velocity of the spinning disk. A diagram of the setup can be seen in Fig. IV-1 below where the medium is considered to be two layers of Lexan and the saltwater.

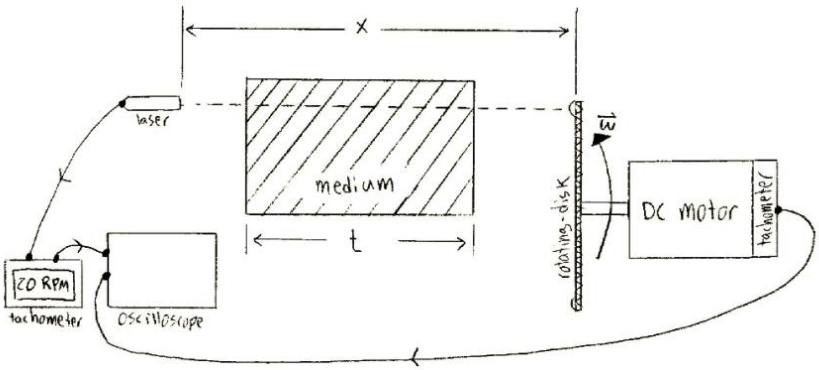

Figure IV-1:
Experimental setup designed to simulate operation in an underwater environment.

For this test, the laser sensor will be positioned a fixed distance from the rotating disk which is set to rotate at a constant speed. At this position, the laser sensor will first measure the rotational speed of the disk with air as the only medium between the laser sensor and the disk. Also, the laser beam will be positioned perpendicular to the rotating disk. Next the laser sensor will be rotated so the beam hits the disk at a 15 degree angle of attack (AOA) followed by a test with the laser sensor rotated again so that the beam hits the disk at a 45 degree AOA. These three tests will be carried out again with first an empty Lexan container between the sensor and disk, followed by a scenario with the same Lexan container filled with sea water. For each of the nine tests, both the voltage output from the laser-tachometer and the motor-tachometer will be recorded. By changing the angle of the laser, the refraction the beam experiences will differ and may change the accuracy. Also, by testing each medium independently, the effects that each medium have on the laser beam can be clearly observed. The results of this experiment will validate the sensor's ability to accurately measure rotational speed though the changing mediums it will experience underwater.

Theory

I. Speed Calibration of Sensor

[Chris Carrier]

In order to ensure the most accurate results possible, both the laser and motor tachometers were calibrated. For this, the rotational speed of the rotor was varied over 10 increments between 0-500 RPM. For the calibration of the motor-tachometer, at each increment its average output voltage was recorded along with the digital RPM measured by the more accurate portable tachometer. From this data the average output voltage can be plotted against the corresponding RPM to create a calibration curve. The sensitivity of the motor-tachometer can then be determined from a best linear fit to the data. The best linear fit will result in the following equation

$$y = mx + b\ , \qquad \text{I.1}$$

where m is the slope and b is the y-intercept. The sensitivity of the device is given as the slope (m) of this best fit line.

For the calibration of laser-tachometer, the average output voltage from both tachometers was recorded at each increment. The motor-tachometer's average output voltage was then converted to an RPM using its previously found sensitivity. From this data a calibration curve was created plotting the average voltage output from the laser-tachometer versus the corresponding RPM calculated from the motor-tachometer's output. Again, a best linear fit can be applied to the data and the sensitivity can be determined from the slope of the line.

II. Distance Validation of Sensor

[Pat Kilar]

As mentioned above, for this part of the experiment the rotational speed of the rotor was fixed and the distance the optical laser is from the rotating cardboard rotor was varied. The average output voltages of both tachometers were recorded at each distance. These output voltages can then be converted to a rotational speed or RPM using the sensitivity determined during each devices calibration. The sensitivity of the devices is given in volts/RPM and therefore by dividing their recorded tachometer output voltage by this value the corresponding RPM of the rotor can be determined. These rotational speeds can then be plotted against their corresponding distance to identify any characteristic trends or deviations

III. Transient Velocity Measuring

[Nate Allen]

As mentioned in the experimental methods section, a voltage step input was applied to the DC motor causing the motor to have a transient response or continually changing rotational speed until it reached steady state. The motors transient response was measured by both the laser-tachometer and the motor-tachometer and their output voltages per unit time were recorded. The accuracy of the laser sensor can be determined by comparing its measured response to that of the highly accurate motor-tachometer. The best way to quantify the characteristics of each response

is to determine their respective time constants. This will not be the time constant of the measuring devices but will be the motor's time constant for a voltage step input. However, by comparing this value from both tachometers, the speed, accuracy and characteristics of the two measuring devices can be identified.

As shown visually in the Fig. III-1, the time in which it takes any system to reach 63.2% of its final steady state output is defined as that system's time constant (τ). Considering the motor's transient speed response was also a first order response, this relationship can therefore be applied to the experimental data recorded by both tachometers. The time constant was determined by first identifying the value of the step by taking the difference of the initial and final values. By taking 63.2 percent of this difference and adding it to the initial value before the response, the value when the motor has reached one time constant can be determined. Knowing this value, the experimental data can be used to identify the time at which the response curve passes this value. The time constant can then be calculated by taking the difference of this time and the initial time at the start of the response. This process will then be done for both tachometers and for all 6 transient response trials. The time constants measured by the two tachometers can then be compared and characteristics can be identified.

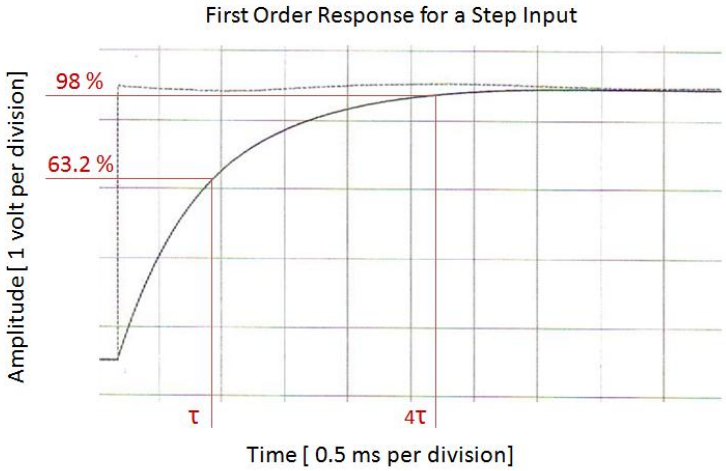

Figure III-1:
An example of a first order transient response to a step input displaying the relationship between the systems time constant and percent of response.

IV. Validation for Marine Environment Implementation

[Shane Baia]

A laser is a form of light that has a specific waveform and color. Unlike ordinary light, a laser is monochromatic meaning it consists of only one color, and is coherent meaning the wavelengths are in phase. Despite its differences, this light form interacts with changing mediums just as all light waves do. When a laser passes through a medium interface at a non-perpendicular angle part of the light is refracted. Also, if the new medium has higher indices of refraction, some of the light is reflected. A diagram of a laser passing through two mediums with different indices of refractivity (n) is illustrated in Fig. IV-2 below.

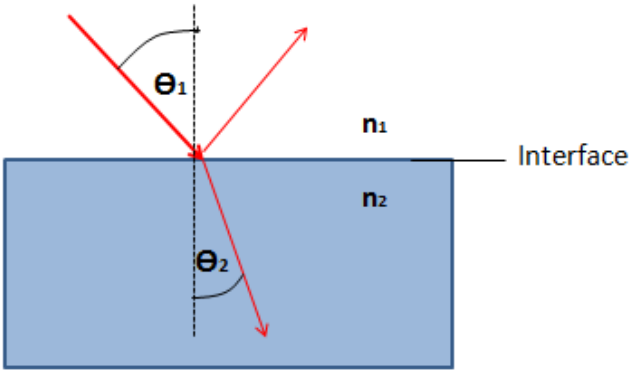

Figure IV-2:
Illustration of a laser being both reflected and refracted as it crosses the interface between two mediums with different indices of refractivity.

The angle of refraction (θ) can be found using Snell's Law which is given by the equation

$$n_1 sin\theta_1 = n_2 sin\theta_2 \ , \qquad \text{IV.1}$$

where *n* is the indices of refractivity and is dependent of the materials dielectric constant or optical density. Snell's law also predicts that the laser will always refract to an angle more normal to the interface if the second medium has a higher indices of refractivity. The indices of refractivity of air, water, and Lexan are 1.0003, 1.33, and 1.51 respectively. Both seawater and Lexan have higher indices of refractivity than air and will cause a level of refractivity in the laser beam for both the 15 degree and 45 degree AOA tests. Since the laser is visible as it makes contact with the rotating disk, the laser can be positioned to hit the reflective tape and account for the refraction. However as the laser reflects off the reflective tape, it would not hit the laser sensor if the beam was not dispersed. The reflective tape is designed to disperse the reflected beam to cover a wider area and increase the likelihood of hitting the sensor. If too much of the laser beam is reflected off the interface, it is unlikely that the laser sensor will measure accurate rotational velocities. To predict the percent of the laser that will be reflected (R) between two mediums the following equation can be used,

$$R = \left(\frac{n_1 - n_2}{n_1 + n_2}\right)^2 \ . \qquad \text{IV.2}$$

From this it can be predicted that there will be some reflection as the laser passes through the interfaces, but sufficient light will still pass through to accurately measure the rotational speed of the disk.

Results and Discussion

I. Speed Calibration of Sensor

[Chris Carrier]

Although most instruments come with a calibration curve from the manufacturer, the device is often calibrated for a different range than what the user will actually be experimenting with. To ensure the most accurate results, the devices were calibrated for specific rotational speeds expected during the experiment, 0 to 500 RPM.

The output voltage from the motor-tachometer plotted against the rotational speed from the portable tachometer can be seen below in Figure I.2.

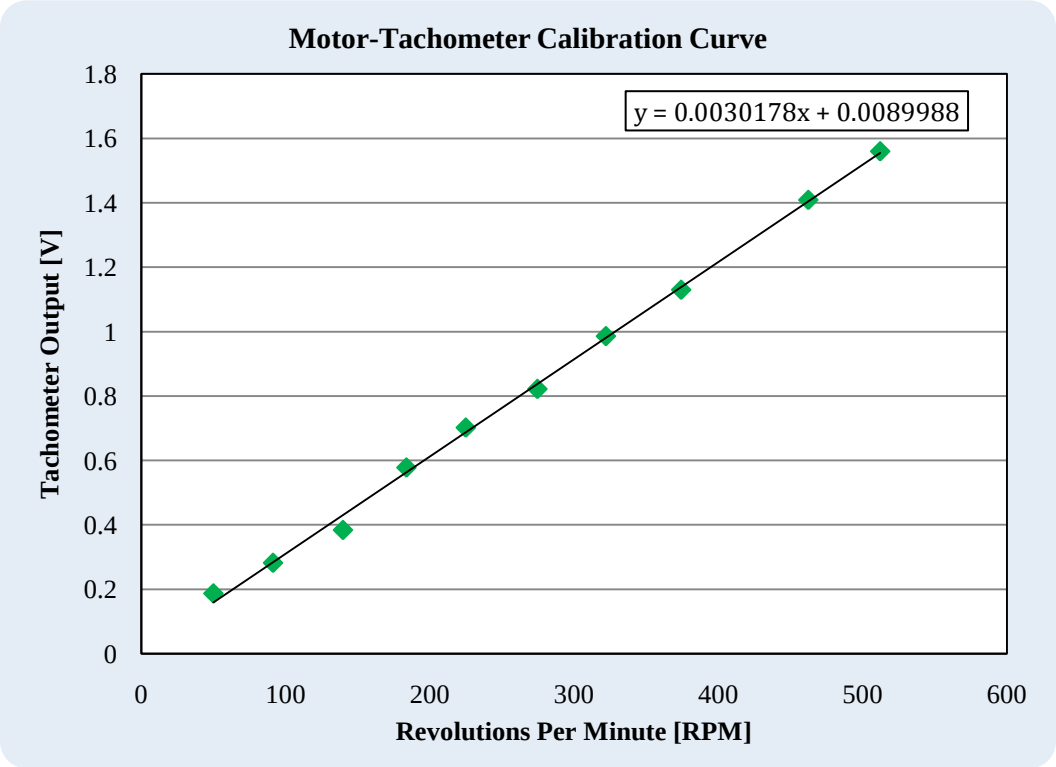

Figure I-2:
Calibration curve for the DC motor's built-in tachometer.

The specified sensitivity of the motor-tachometer was given as 0.003 ± 10% volts/rpm. The experimental sensitivity determined from the slope of the best fit line in the figure above was found to be 0.00302 volts/RPM.

A calibration curve for the laser-tachometer is shown below in Fig. I-3. This figure is a plot of the output voltage from the laser tachometer versus the corresponding RPM determined from the motor-tachometer.

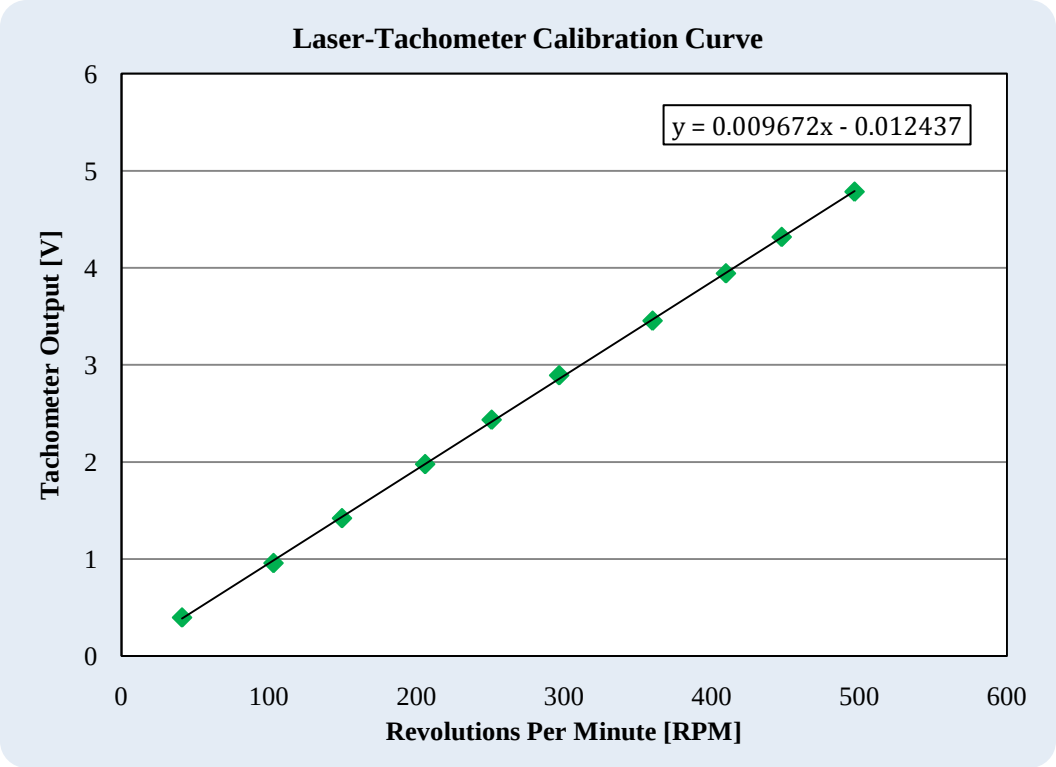

Figure I-3:
Calibration curve for the laser-tachometer.

From the laser's calibration data, the experimental sensitivity of the device was determined to be 0.00967 volts/RPM. The experimental sensitivities are compared to the ideal sensitivities in Table I.1 below.

Table I-1:
Manufacture's rated sensitivities vs. experimental calculated sensitivities

	Manufacturer's Specified Sensitivity	Experimental Sensitivity
Motor-Tachometer	0.003 ± 10%	0.00302
Laser-Tachometer	0.01 ± 10%	0.00967

Note: Sensitivities given in [volts/RPM]

For both devices, the experimental sensitivity was found to be slightly different from the manufacturer's specified sensitivity; however, the deviations were within an acceptable range.

II. Distance Validation of Sensor

[Pat Kilar]

The manufacturer states that the optical sensor should be accurate for a range of distances between 1 inch and 25 feet. However, for our application the device will be used over small distances; therefore data was collected to validate the accuracy of the sensor at small distances. As indicated above with the sensor mounted perpendicular to the rotor, both tachometers output

voltages were converted to RPM and plotted against their corresponding distance as shown in Fig. II-1 below. The laser distances from the rotor were separated into small, intermediate and large classifications, sets 1-3 respectively. To clearly represent the small and intermediate distances, set 3 was omitted from the plot.

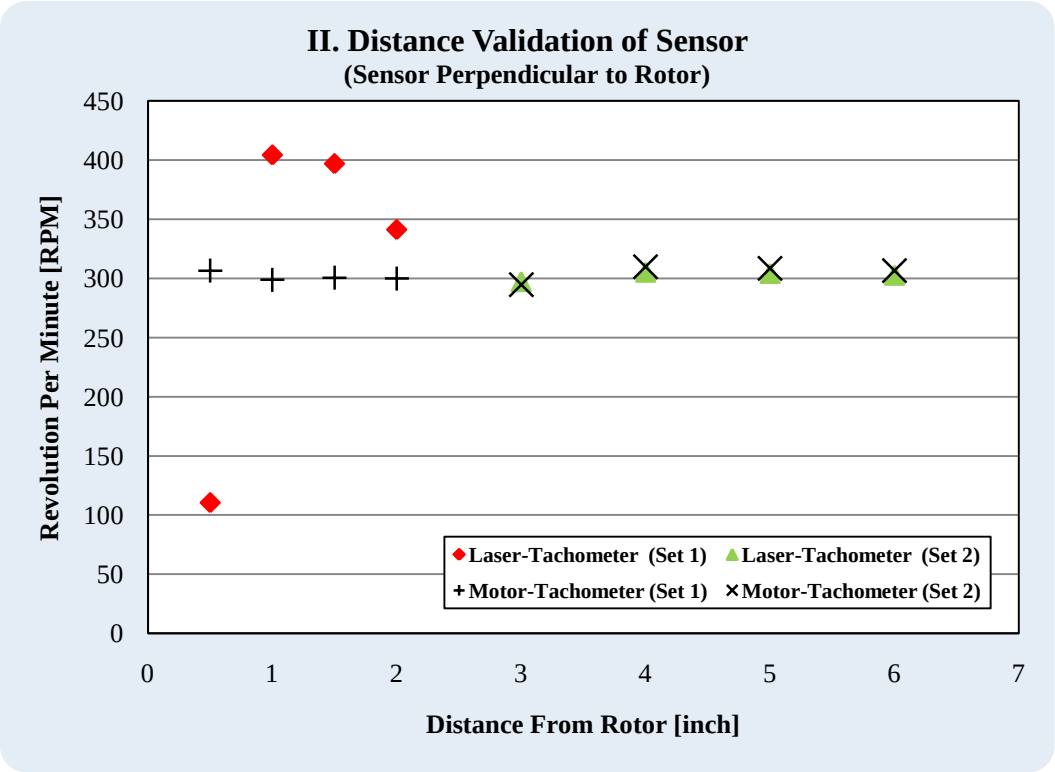

Figure II-1:
A plot of the measured RPM of both the motor-tachometer and laser-tachometer versus the distance the sensor is from the rotor.

Ideally, the laser-tachometer should have the same RPM measurement as the motor-tachometer; however a slight variation is expected. From the plot above, it is apparent that the device encountered severe inaccuracies for all distances less than 3 inches. Due to these inaccuracies, it was decided to re-run the experiment using the manufacturer's recommended 15 degree AOA. The results of this additional testing are displayed in the same manner in Fig. II-2 below.

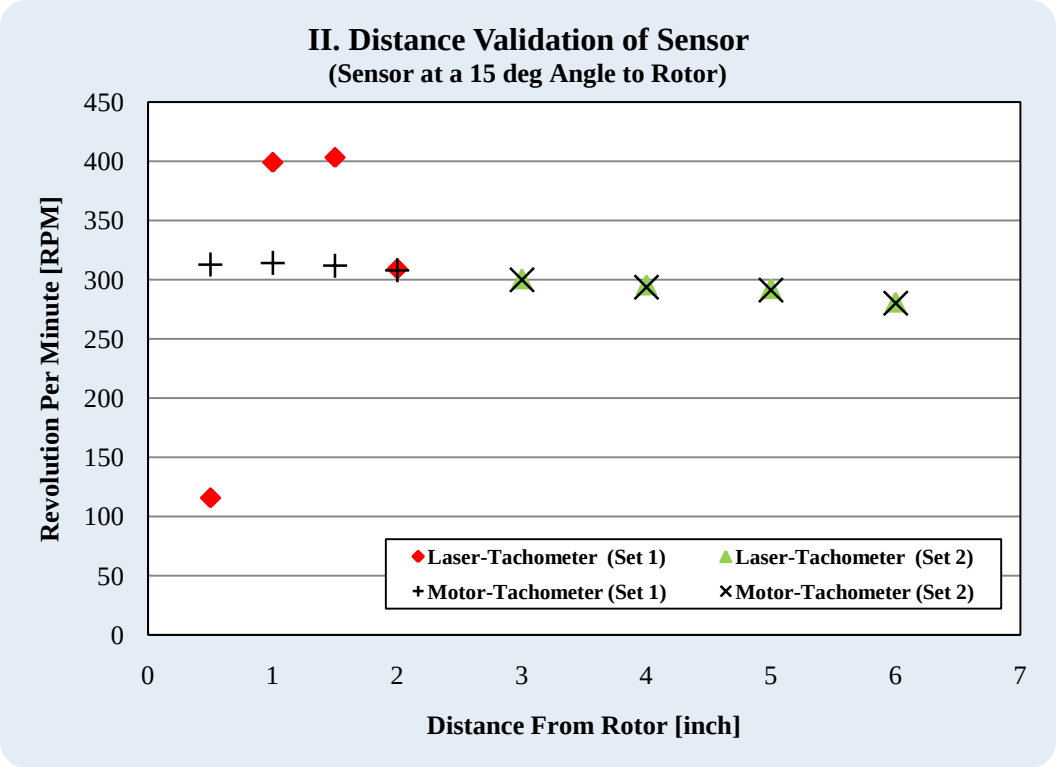

Figure II-2:
A plot of the measured RPM of both the motor-tachometer and laser-tachometer at a 15 degree AOA.

In this repeat experiment, similar inaccuracies were found at small distances; however, the RPM measurement at 2 inches proved to be accurate. Although it was determined that the device is capable of measuring accurate RPM up to 48 inches, the ideal range of distances for its practical application was determined to be between 3 and 6 inches.

III. Transient Velocity Measuring

[Nate Allen]

Our chosen laser sensor only records 6 ticks per revolution which is far less than the high accuracy motor-tachometer which has thousands of ticks per revolution. Due to the limited number of ticks of our measuring device, how accurately it can record a changing in rotational speed was unknown. Therefore, the transient response from the laser-tachometer was compared to the highly precise response of the motor-tachometer in order to quantify how accurately it measures changing rotational speeds. To compare these two responses, the time constant of the motor was calculated from the output signal of each device.

These experimentally found time constants, as well as the 2 percent settling time, are displayed below in Table III-1. In the following table, set 1 corresponds to a step input to the motor of decreasing voltage which causes a decreasing rotational speed transient. In contrast, set 2 corresponds to a step input of increasing voltage which causes an increasing rotational speed transient. Due to the slight oscillations within the tachometer output responses, experimentally determining the exact time constant was hard to identify. Because of this, the average time constant for both sets of transients were calculated which gave a more truthful representation of

the actual value. Also displayed in the chart are the differences between the time constants calculated from the laser-tachometers signal and the motor-tachometers signal.

Table III-1:
Table of the calculated time constants and speed of responses for the DC motor determined from both the motor and laser tachometer output signals.

			Time Constant			Speed of Response		
Set	**Trial**	**Transient Type**	$(\tau)_m$	$(\tau)_L$	**Diff**	$(4\tau)_m$	$(4\tau)_L$	**Diff**
1	1	Decreasing	0.878	0.933	0.055	3.512	3.732	0.220
	2	Decreasing	0.886	0.962	0.077	3.544	3.851	0.307
	3	Decreasing	0.931	0.986	0.055	3.724	3.944	0.220
Average			**0.898**	**0.961**	**0.062**	**3.593**	**3.842**	**0.249**
2	1	Increasing	0.731	0.801	0.069	2.926	3.203	0.278
	2	Increasing	0.797	0.867	0.070	3.188	3.468	0.280
	3	Increasing	0.688	0.738	0.050	2.752	2.952	0.199
Average			**0.739**	**0.802**	**0.063**	**2.955**	**3.208**	**0.252**

Note: The (m) and (L) subscripts indicate determined value from the laser and motor tachometers respectively. All values are given in seconds.

For each experimental trial, the motor-tachometer sensor and the optical laser sensor were set up to measure the same response of the motor. Therefore, the time constant determined by the laser-tachometer and the motor-tachometer should ideally be identical. However, when examining the data shown above it is clear that the two time constants are different. By looking at the "Diff" column above, it is clear that for each trial in both sets the laser-tachometer has a slightly larger time constant. To get a more accurate representation of the true time constant determined by the devices, the "Average" row was considered. For a decreasing rotational speed transient, set 1, the average time constant determined by the motor-tachometer was 0.898 seconds compared to that of the laser-tachometer, which was 0.961 seconds. This results in a difference of 0.062 seconds. The average time constants for an increasing transient were found to be 0.739 and 0.802 seconds from the motor and laser respectively. The difference of these two average time constants was 0.063 seconds which is almost identical to the difference found from set 1, the decreasing transient. This proves that even for different transient changes in rotational speed, the laser-tachometer output signal has a fairly consistent, slightly slower response than that of the precise motor-tachometer.

The initial assumption for this slower time constant was that the time in-between ticks for the laser sensor was much larger than that of the motor-tachometer sensor. However, when quantifying this time between ticks, even at a slow speed of 100 RPM, it was found to be only 0.001 seconds which is an order of magnitude less than the overall difference calculated and therefore cannot be the sole contributor to this slower response. When looking at the tachometer output signal response curves for both tachometers, it became clear that for almost all trials, the laser-tachometer had a slight "lag" or delay before its response started in comparison to the start of the response from the motor-tachometer. This slight delay is depicted in the following plot which displays the output signal responses for both tachometers for a decreasing transient. From

this figure, it is clear that both tachometer output signals have similar response characteristics, with the only difference being the initial delay of the laser-tachometers signal.

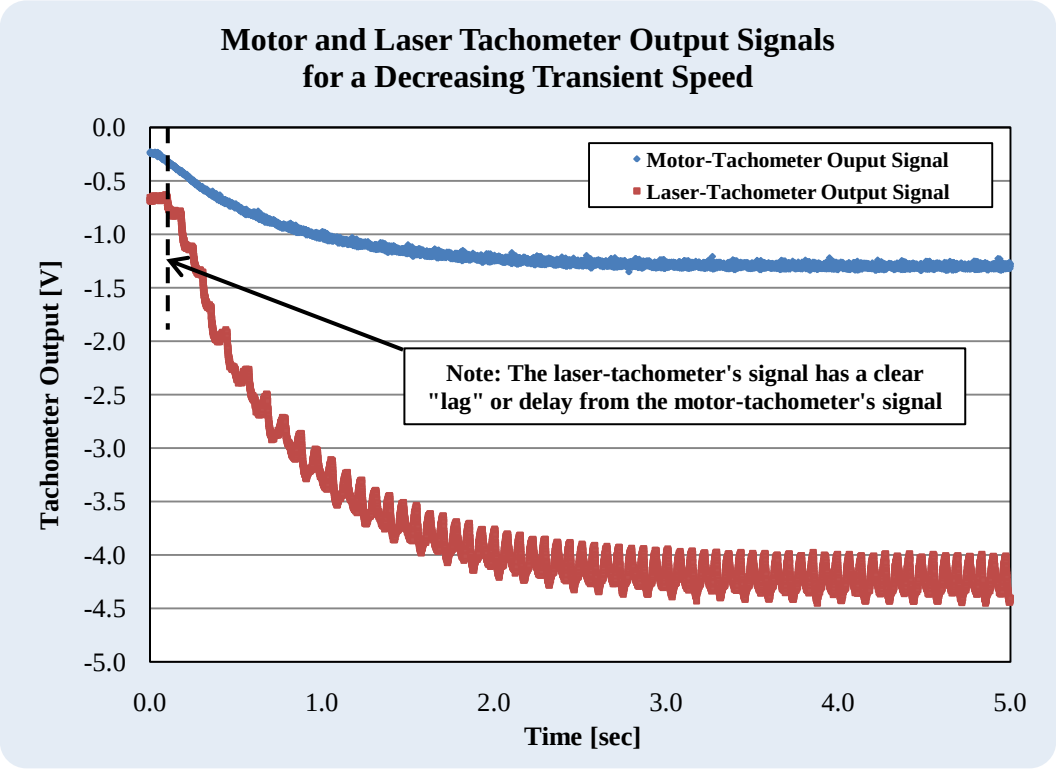

Figure III-2:
Plot of the motor-tachometer's and laser-tachometer's output voltage signal for a decreasing transient rotational speed response of the DC motor to a step input.

In summary, the slightly slower time constant determined by the laser-tachometer was found to be mostly due to this definite delay or response rather than the resolution of ticks per revolution on our laser sensor. The exact cause of this "lag" is not fully known. One possibility is that the delay could be caused by the filter that the laser-tachometer's output signal was sent through. It is known that a filter can remove noise from a signal; however, if it is not designed with appropriate capacitances the characteristics of the signal can be affected and changed. Therefore, it may have been the op-amp filter that was used to remove noise from the signal that caused this delay in the response signal. However, the most likely cause of this delay was due to the laser-tachometer itself. The laser-tachometer operates by taking a voltage pulse signal from the optical laser sensor, converts that signal into an RPM and then outputs a voltage signal that is proportional to the RPM, which is what we recorded. Although the exact characteristics of the laser-tachometer are unknown, it is likely that the tachometer waits until it receives a few revolutions worth of voltage pulse signals to make sure it has enough data to accurately convert into an RPM before it sends an output voltage. If this assumption is true, this would explain why the laser-tachometer's output signal does not start until slightly after the motor-tachometers signal. It also justifies that once the response starts it has very similar characteristics to that of the motor-tachometer because they are both accurately measuring the same transient response.

IV. Validation for Marine Environment Implementation

[Shane Baia]

For this part of the experiment, the laser sensor was used in a simulated underwater environment, emulated by a Lexan container filled with saltwater. The laser visually passed through all three mediums and made contact with the reflective tape. Also, the device was able to measure a rotational velocity that was comparable to the velocity indicated by the pre-calibrated motor-tachometer. Though the refraction of the laser beam was not visible, the reflection could be observed on the Lexan surface. From Eq. IV-2 above, the percent reflection of the laser between the air/Lexan interface was calculated to be 4.07 %. This small percentage indicates that a sufficient portion of the laser beam passed through the interface and reached the reflective tape. The fraction of laser light that is needed to excite the laser sensor is unknown but is assumed to be fairly small since the feedback laser is a scattered low intensity light wave. As stated above, there is associated refraction in the beam as it travels through the mediums. The predicted refraction angles are seen in Fig. IV-3 below.

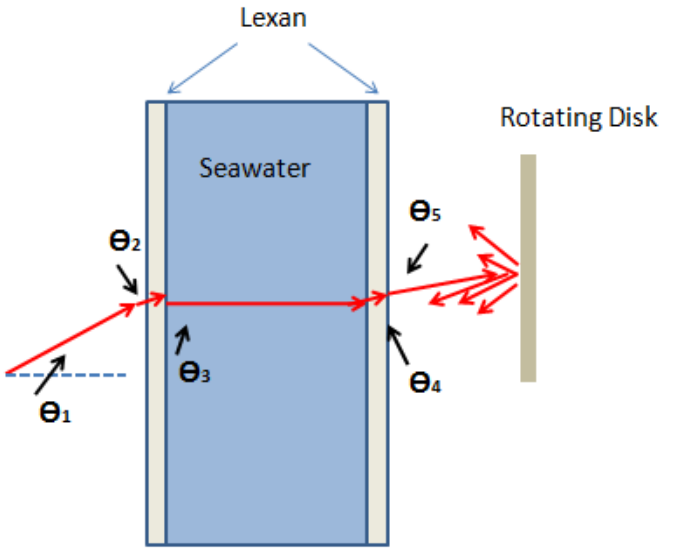

15 degree AOA		
Θ1	*15*	*degrees*
Θ2	*9.89*	*degrees*
Θ3	*11.26*	*degrees*
Θ4	*9.89*	*degrees*
Θ5	*14.99*	*degrees*
45 degree AOA		
Θ1	*45*	*degrees*
Θ2	*28.01*	*degrees*
Θ3	*32.22*	*degrees*
Θ4	*28.01*	*degrees*
Θ5	*38.52*	*degrees*

Figure IV-3:
Illustration of the refraction of the beam from the laser sensor to the disk.
List of the angles of refraction calculated using Snell's Law for both AOA.

In all three scenarios and all AOAs, the laser-tachometer was sufficiently accurate compared to the pre-calibrated motor-tachometer. The output voltages of the motor-tachometer $(e_o)_m$ and laser-tachometer $(e_o)_L$ were recorded and converted to RPM using their sensitivities. These values as well as the percent error of the laser-tachometer compared to the motor-tachometer can be seen below in Table IV-1.

Table IV-1:
Table of the output voltages from the motor-tachometer and laser-tachometer and their corresponding RPMs for all nine scenarios.

AOA = 0 deg					
Medium	**$(e_o)_L$**	**$(e_o)_m$**	**$(RPM)_L$**	**$(RPM)_m$**	**% Difference**
Air	2.809	0.87	290.41	288.29	0.737
Lexan	2.698	0.836	278.94	277.02	0.691
Lexan & Water	2.784	0.862	287.83	285.64	0.767

AOA = 15 deg					
Medium	**$(e_o)_L$**	**$(e_o)_m$**	**$(RPM)_L$**	**$(RPM)_m$**	**% Difference**
Air	2.808	0.869	290.31	287.96	0.817
Lexan	2.81	0.87	290.52	288.29	0.773
Lexan & Water	2.9	0.899	299.82	297.90	0.646

AOA = 45 deg					
Medium	**$(e_o)_L$**	**$(e_o)_m$**	**$(RPM)_L$**	**$(RPM)_m$**	**% Difference**
Air	2.75	0.851	284.31	281.99	0.823
Lexan	2.849	0.882	294.55	292.27	0.781
Lexan & Water	2.84	0.879	293.62	291.27	0.806

From Table IV-1 above, it is evident that the tachometer was effective at reading the rotational velocity of the disk since the percent difference for all scenarios were under 1%. The least accurate scenario proved to be the tests with an AOA of 45 degrees. There seemed to be no clear difference in accuracy when testing the device through any combination of the three mediums.

It should be noted however that the laser-tachometer always read a RPM that was slightly faster than that of the motor-tachometer. This observation may be better observed from Fig. IV-4 below. This observation is likely not due to the medium that the laser is traveling through, but rather is a characteristic of the device. Either the laser-tachometer or the motor-tachometer may be slightly inaccurate. For the intended application of the laser-tachometer, this inconsistency is irrelevant.

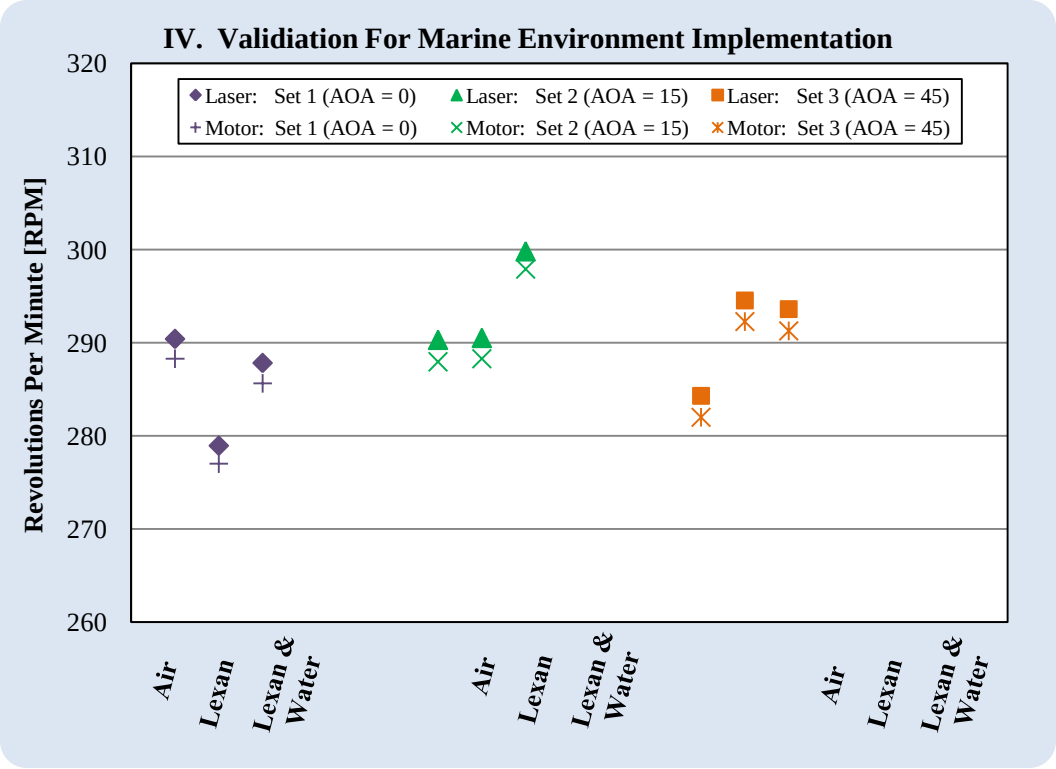

Figure IV-4:
Plot of all nine scenarios comparing the output of the laser-tachometer to the motor-tachometer

Conclusion (Nate Allen)

The overall objective of the experiment was to determine if a rotational speed measuring device could successfully be implemented on a hydrokinetic (underwater) turbine featuring Variable Flux Generation (VFG). For this unique marine environment application, the chosen rotation speed measuring device was an optical laser sensor connected to a tachometer. This laser sensor will measure the rotational speed by shooting a laser from a fixed position at the turbine's rotor which will be spinning and moving axially. The rotor will contain 6 reflective spots which the device senses as they cross the path of the laser.

The purpose of our laboratory experiments was to validate whether or not the chosen laser tachometer will be able to accurately measure the rotational speed of the rotor in the prescribed underwater conditions. To verify the laser sensor's accuracy it was compared against a highly accurate traditional tachometer mounted to the rotating shaft of the rotor. To ensure a fair comparison the traditional (motor-tachometer) was calibrated over the probable RPM range for this application, approximately 0-500 RPM. From this calibration the exact sensitivity of the device was determined, which was very close to the manufacturers specifications verifying are results. Before any validation or performance of the laser sensor was done it had to be calibrated. The sensor was positioned at a fixed distance from the rotor and calibrated over the same range of 0 – 500 RPM. The sensitivity of the device was determined to be 0.00967 volts/RPM which can be used in all proceeding experiments to identify the true RPM that corresponds to the laser-tachometers output voltage.

With the device calibrated, the first experiment was to validate that the laser does work over the manufacturer's specified range of distances, 1 inch to 25 feet. From the experiments it was determined that for our application the device does not have repeatable accuracy until a distance of 3 inches from the rotor. The likely acceptable range the device will be finally implemented to operate in is 3 to 6 inches. The next important characteristic of the device that needed to be determined was how accurate it was at changing rotational speeds. The device was mounted at a fixed distance and set up to record various increasing and decreasing transient changes in the rotational speed of the rotator. By comparing the time constants determined by the laser-tachometer and the motor-tachometer it was identified that the laser-tachometer consistently had a slightly slower value. This slower value was attributed to a delay in the laser-tachometers response which is assumed to be caused by the characteristics of the laser-tachometer itself. The final and arguably the most important experiment left to conduct was to validate whether the device can be implemented in a simulated underwater environment. For our specific application the laser sensor would have to be used through Lexan as well as saltwater. Due to light diffraction the device was test perpendicular to the rotor as well as at various angles to the rotor. From the experiments it was found that at all angles the laser worked accurately through both the Lexan and the saltwater.

In summary, the results to all 4 of our experiments allowed us to determine both the characteristics of our device and whether or not it can be implemented for our application. It was found that the device accurately measures and records constant and transient rotational speeds with only a slight delay in its response, which should not be a problem in our application. The optical laser sensor was also validated to work accurately in a simulated underwater environment and therefore should be able to be implemented for use on our hydrokinetic turbine.

Conclusion (Shane Baia)

Overall, the laser optical rotational measurement device was effective at measuring rotational speed, but some important criteria was found that will be taken into consideration before the device is implemented on the VFG turbine project. This device's RPM output will be used to determine the efficiency of the turbine rotor and will be used in the actuator control system, and the results from this experiment show that this device can accurately read within the required precision.

From the calibration of the device, it is not entirely clear if the dissimilarity between the laser-tachometer's calibrated sensitivity and the manufacturer's sensitivity is accurate or if it is just due to the inaccuracies of the motor-tachometer. Either way, the sensitivity is realistic and will produce sufficiently accurate RPM readings to be used in reality. Also the device can read the rotational velocity within the range of RPMs that is expected from the turbine. From a distance, the device is accurate past 2 inches and to at least 48 inches. However, with distances shorter than 2 inches, the accuracy of the device is compromised significantly. This is due to the fraction of light that is reflected off the disk, which at a close range is intense enough to trigger the laser-sensor.

The device's ability to measure the changing speed of the rotating disk was also accurate to within 1% of the motor-tachometer. The laser-tachometer's ability to measure changing speed is dependent on the distance between the reflective tape. However, since the rotating disk is spinning at a reasonably fast RPM, the time between ticks is reduced to milliseconds. The second cause for inaccuracies in measuring changing speed is the laser-tachometer's ability of turning pulse readings into a constant voltage. This conversion may cause most of the lag between the two tachometers. Lastly, the device was effective through all tested mediums as expected. The laser will experience minimal reflection and the refraction can be accounted for visually when setting up the device. When the laser reflects off the tape, the return beam is scattered so it will likely be picked up by the sensor.

I am confident in this device's ability to measure rotational velocity for our application as long as the device is at a distance greater than 2 inches from object being measured. Finally, I believe that the test through the mediums accurately simulated the underwater environment and should justify our proposed waterproofing method.

Conclusion (Chris Carrier)

To ensure the most accurate results possible, both the motor-tachometer and laser-tachometer were calibrated based on what we expected in the real life application. Although the ideal sensitivities of both devices were known, it is best not to assume the devices have been properly calibrated. It was discovered that the experimental sensitivity from the calibration process was almost identical to the ideal sensitivities with percent error of less than three percent.

With the devices calibrated, the laser tachometer was validated for varying distances from the rotating disk. These distances occurred at set distances from as close as 0.5 inches to 4 feet. The laser was also placed at both 0º and 15º with respect to the rotating disk. The laser-tachometer manufacturer states that the optical sensor should be accurate for a range of distances between 1 inch and 25 feet however this did not coincide with our data. It was discovered that any data collected with the sensor less than 2 inches away from the disk gave very bad and unpredictable data. This error at close range is most likely due to the sensor getting too much reflection from the laser. Lastly, while the laser tachometer accurately obtained data at the other distance increments, the ideal range of operation was determined to be between 3 and 6 inches and at an angle of 15º.

The transient velocity response was measured to quantify how accurately the laser-tachometer can measure the abrupt changes in rotational speed it will likely encounter during the real world application. Before the experiment, it was assumed that because the motor-tachometer has thousands of ticks per revolution compared to our devices 6, it would have a slightly faster system response. In the end, it was discovered that while the motor-tachometer did have a faster response as expected, it wasn't much faster than that of the laser-tachometer. This indicates that the laser-tachometer can be successfully implemented to measure real time transient response during application.

As the turbine that is going to be tested next semester will be underwater, the water medium test was the most important experiment performed during the lab. Most likely, the laser will be encased in a Lexan box during deployment, so experiments were run with only Lexan, then Lexan and Salt Water. Before the experiments, we were concerned that the laser would experience significant refraction while going through the water leading to erroneous data. However, the laser-tachometer was successful at measuring RPM accurately at 0º, 15º and 45º with respect to the rotating disk, validating the sensors ability to accurately measure rotational speed while in a marine environment.

In the beginning of the experiment, we had some doubt as to whether or not the laser would be able to be used underwater due to the refraction light experiences as it passes through an angle. However, this experiment proved that as long as you have the instrument correctly positioned and properly calibrated, the laser-tachometer can accurately be used in a marine environment. Some error was experienced, such as the erroneous data we gathered when the sensor was less than 2 inches away from the rotating disk. This erroneous data proved useful in constructing an ideal distance and angle of attack setup to get the best results. Further experimentation could have narrowed the setup distances further, but the current setup yields results accurate enough for our uses.

Conclusion (Patrick Kilar)

We are involved in the second generation development of the hydrokinetic turbine featuring variable flux generation. A component of our senior projects design is that it requires a reliable rotational speed sensor accurate through water and Lexan (the material of the waterproof container) at small displacements. A laser-tachometer sensor has been chosen and we have quantified its calibration curve and time constant along with its performance at measuring different RPM at different distances, angles, and through different mediums. The laser tachometer was calibrated between 0-500 RPMs and it exhibited a linear trend. This was what we expected. Using that value we can now accurately transform the DC output voltage from the laser-tachometer to a rotational speed for accurate speed measurement in the future. The manufacturer stated the laser-tachometer was accurate in a range between 1 inch and 25 feet away from the rotating surface. However for our application the laser will only operate through small distances between ~1-6 inches. The rotor was kept at a constant RPM and the RPM from the motor-tachometer and the laser-tachometer were close to one another for the operating distances we are small operating distances we are considering. Closeness between the laser-tachometer and motor-tachometer was improved when the laser was offset at a 15 degree angle. The laser manufacture states the improvement is attributed to the decrease in laser interference. Overall the optimal distance to place the laser sensor is 3-6 inches away from the rotor at an angle offset by 15 degrees.

In application the turbine will not be rotating at constant speeds. It will vary over the course of the day depending on the specific tidal flow changes. Based on this parameter the laser-tachometers speed of response should be relatively quick. From various disturbances we examined it was found the speed of response was on the order of milliseconds. We believe that this speed of response is more than acceptable for our application. The laser sensor was also validated to work through Lexan and a water filled container at various angles to verify if any hypothesized refraction or measurement degradation would be induced by measuring through these mediums. We found the laser sensor did not suffer any noticeable measurement degradation or refraction from measuring through different mediums that we hypothesized might occur. From the results of our study we now have the confidence that the laser sensor can operate accurately at acceptable design distances, through different mediums, and with a reasonable speed of response to changing currents.

References

[1] Figliola, R. S., and D. E. Beasley. *Theory and design for mechanical measurements* . 4th ed. Hoboken, N.J.: John Wiley & Sons, 2006. Print.

[2] Ogata, Katsuhiko. *System dynamics* . 4th ed. Upper Saddle River, NJ: Pearson/Prentice Hall, 2004. Print.

[3] "Optical Laser Sensors." *Monarch Instrument*. N.p., n.d. Web. 20 Nov. 2010. <http://www.monarchinstrument.com/product.php?ID=46>.

[4] "Panel Tachometers: ACT Series ." *Monarch Instrument*. N.p., n.d. Web. 20 Nov. 2010. <http://www.monarchinstrument.com/product.php?ID=16>.

[5] "Refraction - Snell's Law." Web. 14 Dec. 2010. <http://interactagram.com/physics/optics/refraction/>.

Appendix - A

Equipment List

- ACT-1B Panel Tachometer
- Remote Optical Laser Sensor
- Reliance Electric DC brush motors and tachometers
- Power Op-Amp (gain of 1)
- National Instruments Oscilloscope
- National Instruments Function Generator
- National Instruments Power Supply
- Powered Protoboard

Appendix - B

Data Tables

Appendix - C

Raw Data Sheets and Sample Calculations

Appendix - D

Experimental Procedure

Appendix - E

Manufacturer's Brochures

- Optical Laser Sensor
- ACT-1B Panel Tachometer

Generator Actuation Research and Development

TECH 797: Ocean Projects

Patrick Kilar

Fall 2010

Design Constraints

i. Force of Engagement
   a. Magnetic Force

Variable flux generation is controlled by the axial displacement between the magnets and the stator. As the axial displacement between the stator and magnets decreases from Regime 1 to 2 the magnetic pull force toward the stator becomes significant. Conversely once the magnet has become engaged in the stator in Regime 3 there is little pull force. These regimes are depicted below in Figure 1.

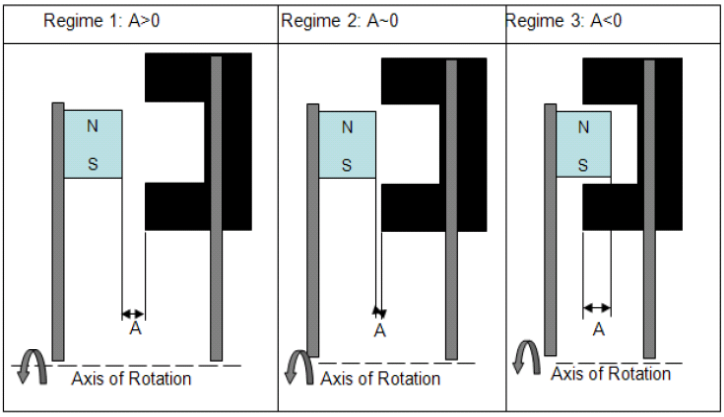

Figure 1:
Three distinct magnetic pull force regimes that depend on the relative distance between the magnet and stator.

Research was carried out to create an actuator to "filter" the significant magnetic pull force in order to allow the operation of the variable flux generator.

   b. Force of Drag

When the tidal currents velocity is low the magnets will become disengaged from the stator to allow minimal start up torque, which in turn allows the turbine to generate electricity at low flow speeds. As the tidal currents velocity increases the magnet engagement within the stator should also increase thereby generating more power. In the ideal operation the engagement will vary based on the amount of flow induced drag on the rotor. Based on theoretical equations that modeled the turbine as a flat plate, the most drag the turbine will see at 6 knots is ~3,000 pound-force acting over the 5' diameter area encompassed by the turbine.

Design Considerations

Magnet/Stator actuation concepts can be divided into two categories those controlled by the induced drag on the rotor and those controlled by a user. Autonomous concepts include a walking beam, piston and spring, and active shock. Non-autonomous concepts include an electronically controlled linear actuator, Teleflex cable, and a hydraulic cylinder.

Autonomous

i. Walking Beam

Two springs of different stiffness's and lengths a pivot point can be used together to accommodate the different force regimes. This walking beam can sufficiently provide repeatable engagement in all three regimes. Theoretical equations could be used to simulate the forces acting on each spring based on forces and different engagements. Significant time would need to be dedicated to calibrating and fine tuning this arrangement through several field tests.

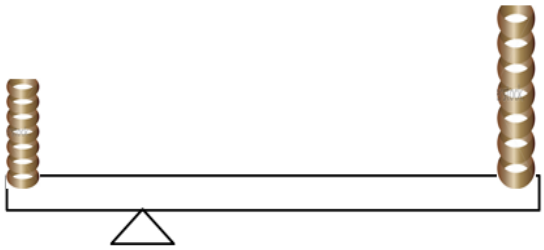

Figure 2:
Walking beam with springs and a pivot point.

ii. Piston and Spring

A spring alone would be insufficient to control the actuation because of the three distinct engagement regimes. However together with a piston that was correctly sized a new piston spring device potentially could handle the distinct regimes better. It would operate by bleeding water to change position. Again time would need to be spent calibrating and fine tuning this arrangement through several field tests.

Non-Autonomous

iii. Electronically Controlled Linear Actuator

Construct a computer logic controlled Proportional Integral Derivative (PID) controller to regulate the distance between the magnets and stator to keep the rotor rotating at a constant frequency. Figure 2 shows a complete system diagram of a frequency driven PID controller applied to the turbine.

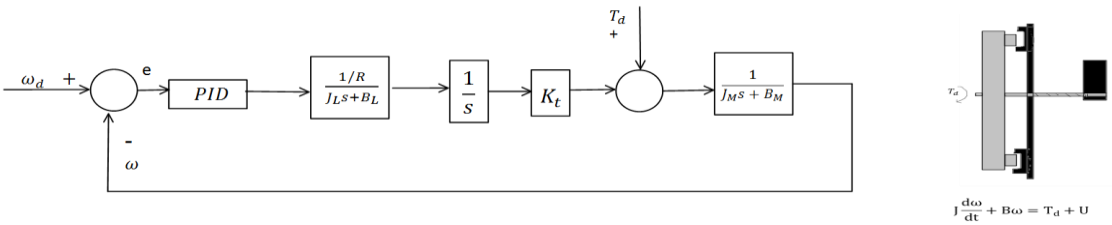

Figure 2:
Complete system diagram of frequency driven PID controller applied to the turbine.
The frequency based closed-loop control system can be simulated using Matlab / Simulink.

Using Ziegler-Nichols tuning and root locus modeling the controller was optimized in terms of speed of response, controller stability, and percent overshoot.(shown in Appendix)
The rotors rotational speed will be the input to the control system. Therefore a rotary speed sensor was purchased. The “laser tachometer was validated at several angles, through seawater,

and distances away from the plate whose rotational speed it was measuring. In order to implement this system a waterproof housing needed to be built and tested.

iv. Active Shock Technology

Using a 12 Volt direct current input to power its processor Active Shocks monitor and control the damping instantaneously. In order to do this electronically controlled hydraulic valves change the orifice size which changes the amount of damping. They boast ½ to 10 times the damping of standard shocks with a full scale step response time of ~10ms. Although this is a Manchester, NH based company this company was unable to collaborate with us.

v. Teleflex Boat Steering Cable

Teleflex steering cables have the long length that we would need to control it from above the water, are waterproof, and are inexpensive. Researching this option further and contacting Teleflex engineers it was determined that the Teleflex steering cable did not have enough strength to withstand the force of drag acting on it at 6 knots.

vi. Hydraulics

Using a small diameter rod and high fluid pressures, hydraulic cylinders can be sized to actuate at the large force of drag seen by the 5' diameter turbine at 6 knots. Hydraulic units may be powered by 12 volt batteries which can be kept on the deck of the boat, and the hydraulic cylinder will be capable of being immersed in the water for the tests we want to perform. Hydraulics was chosen because it could control the position and withstand the large forces most effectively. The walking beam and piston and spring both would require building test models to determine a final design. We could not collaborate with activeshock, the Teleflex cable was not strong enough, and to implement the PID controller we would have to build and test a water-proof housing.

Testing and Calibration

The complete hydraulic system needed to be sized appropriately to withstand the large forces and pressures, the relative distance between the magnets and the stator needs to be quantified as the position changes, and the system needs to be integrated onto the deployment structure.

a. Sizing the Cylinder

A hydraulic cylinder capable of ~ 15,000 lbs of pushing power with a 6" stroke, 3" bore, powered by a 12 Volt battery power unit, containing Envirologic hydraulic fluid operating at 2,000 psi was used. The engineering calculations to support the force calculations are listed in the appendix.

b. Positioning

Instead of purchasing a standard push button controller we built our own controller from buttons and electronic relays. This controller allowed the hydraulic rod to be extended and retract freely using two separate buttons, and allowed it to move specific distance either direction using another two buttons.

c. Integration into the Deployment Structure

There are several components involved in the hydraulic system. The core component is the 12 Volt powered hydraulic power unit which is the reservoir of hydraulic fluid that regulates the pressure differential in the hydraulic lines in which the fluid travels. In order to make the design more robust a lock valve was put between the power unit and cylinder to ensure the cylinder end would not move. The hydraulic system showing the position controller, hydraulic power unit, 12 Volt battery, lock valve, hydraulic lines, and hydraulic cylinder are shown below in Figure 4.

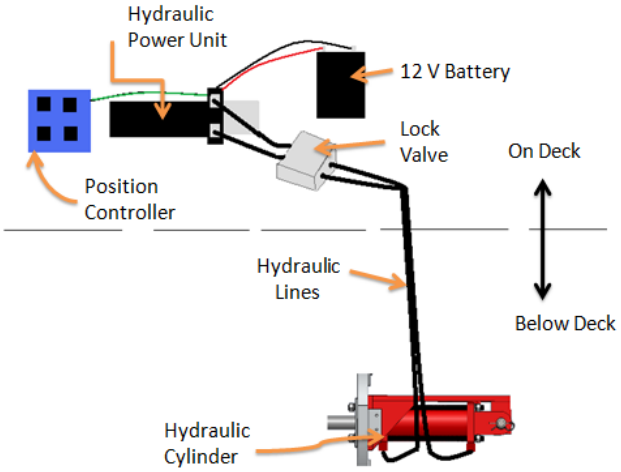

Figure 4:
The hydraulic system integrated to the deployment structure; showing the position controller, hydraulic power unit, 12 Volt battery, lock valve, hydraulic lines, and hydraulic cylinder.

To make the installation of the cylinder to the deployment structure the hydraulic lines could be disconnected from the lock valve without spilling oil using “quick disconnect” fittings. This allowed the on deck components to be securely fastened to the barge deck, while the hydraulic cylinder and lines could be mounted to the underwater structure.

Appendix A – (Hydraulic Cylinder Design Calculations)

Given information;

3" cylinder bore
1.25 rod diameter
6" stroke
System pressure 2,000 psi

Results;

Cylinder Calculation

1) FULL End of cylinder, push
Find surface area of piston first;
= (radius of piston) squared x Pi pi = 3.14 radius = 1/2 diameter of piston
= 1.5 squared x 3.14
= 2.25 x 3.14
= 7.065 sq inches

Force of cylinder push = piston area x hydraulic pressure
= 7.065 x 2000 psi
= 14,130 lbs push

2) ROD End of cylinder, pull
Find surface area of piston and subtract area of rod.
Area of full end piston = 7.065 sq inches
Area of rod
= (radius of rod) squared x Pi pi= 3.14 radius = 1/2 diameter of rod
= .625 squared x 3.14
= .47266 x 3.14
= 1.226 sq inches

= 7.065 sq inches piston - 1.226 sq inches rod
= 5. 839 sq inches acting on rod end

Force of cylinder pull = piston area x hydraulic pressure
= 5.839 x 2,000 psi
= 11,678 lbs pull

3) Volume of oil to extend (cubic inches)
Area of piston x stroke (length)
= 7.065 x 6
= 42.39 cubic inches of oil

1 cubic inch = .554112554 fluid ounces

42.39 cubic inches of oil = 23.488 fluid ounces

Power Unit

Item Number	84463207
Brand	Stone
Maximum PSI	2000.00
Voltage	12 VDC
GPM	1.35
Amperage Rating	225
Tank Capacity	3.0 Qts.
Port Size	9/16-18 SAE
Length (Decimal Inch)	20.250
Height (Decimal Inch)	7.00
Width (Decimal Inch)	8.1300
Description	Solenoid Operated Power Unit for Double-Acting Cylinder
Big Book Page #	3918

Hydraulic Cylinder

Baileynet.com

ChiefTC3 Agricultural Tie-Rod Hydraulic Cylinders

Availability: On Order

Price Each/Quantities of:

1 - 9	$109.00
10 - UP	$100.00

BUY

These 3000 PSI cylinders are available in bore sizes from 2" to 5" and stroke sizes from 4" to 60". ChiefTC3 cylinders are backed by a 4-year limited warranty and are ideal for construction and agricultural applications.

BORE	3" Bore - 3000 PSI	**COLUMN LOAD**	21200 lbs
STROKE	6"	**PORT SIZE**	SAE 8
ROD DIA	1 1/4"	**PIN DIA**	1"
RETRACTED	16 1/4"	**SHIP WT.**	23
EXTENDED	22 1/4"	**BAILEY NO**	211-346

Appendix – B (Rotor Rotational Velocity Control)

Low flow tidal currents	$\omega_{operating} = 115$ rpm
Self-propelled barge top speed	$\omega_{barge} = 320$ rpm
Maximum rotation	$\omega_{max} = 500$ rpm

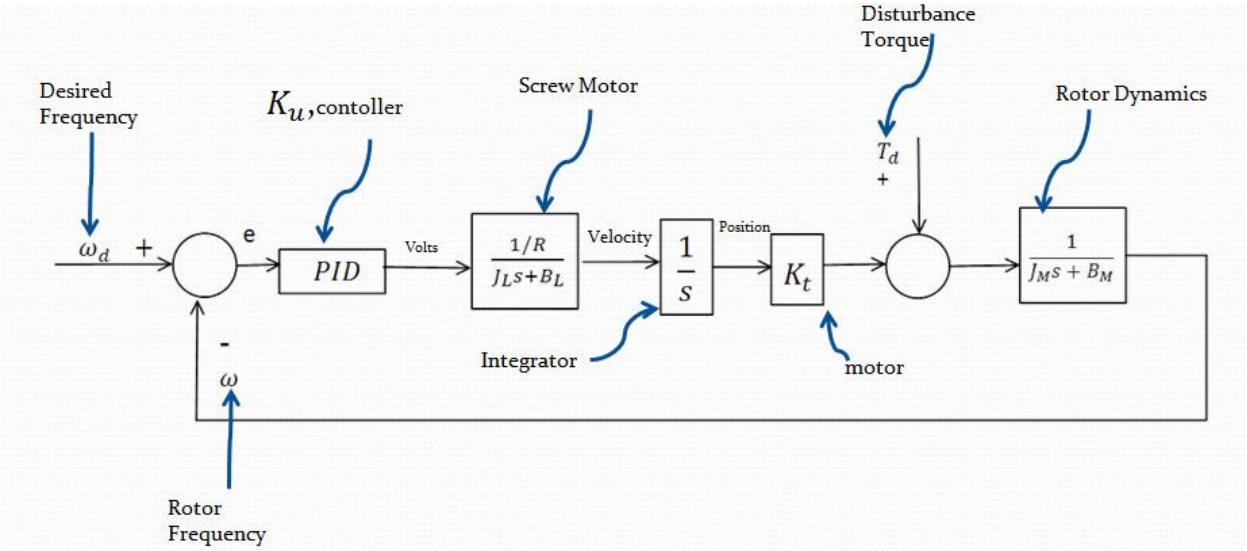

Figure 1:
Block Diagram of the System.

PID Controller Design

Using Ziegler Nichols

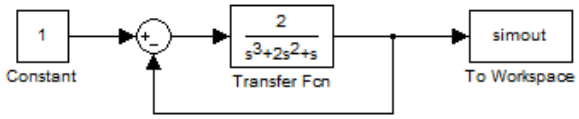

Figure 2:
Simulink representation of transfer function. Constant input of 1 into system.

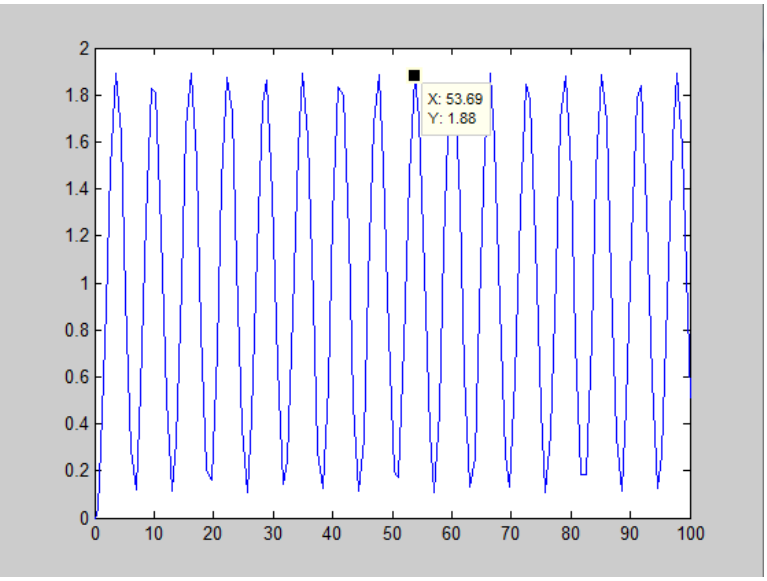

Figure 3:
Simulink representation of transfer function Simout from Figure 2. Constant input of 1 into system.

```
Kcr = 2;
Pcr = 5.97;
%% Outut parameters
Kp = 0.6*Kcr;
Ti = 0.5*Pcr;
Td = 0.125*Pcr;
G_c = Kp*(1+(1/Ti*s)+Td*s);
G_cONE = 0.075*Kcr*Pcr*(((s+(4/Pcr))^2)/s);

tf2_num = G_c*lin_num*int_num*K_torque*rotor_num;
tf2_den = lin_den*int_den*rotor_den;

TF_2= tf2_num/tf2_den;
```

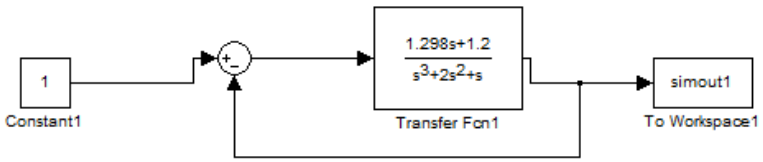

Figure 4:
Simulink representation of transfer function with P I and D values quantified by Zeigler method. Constant input of 1 into system.

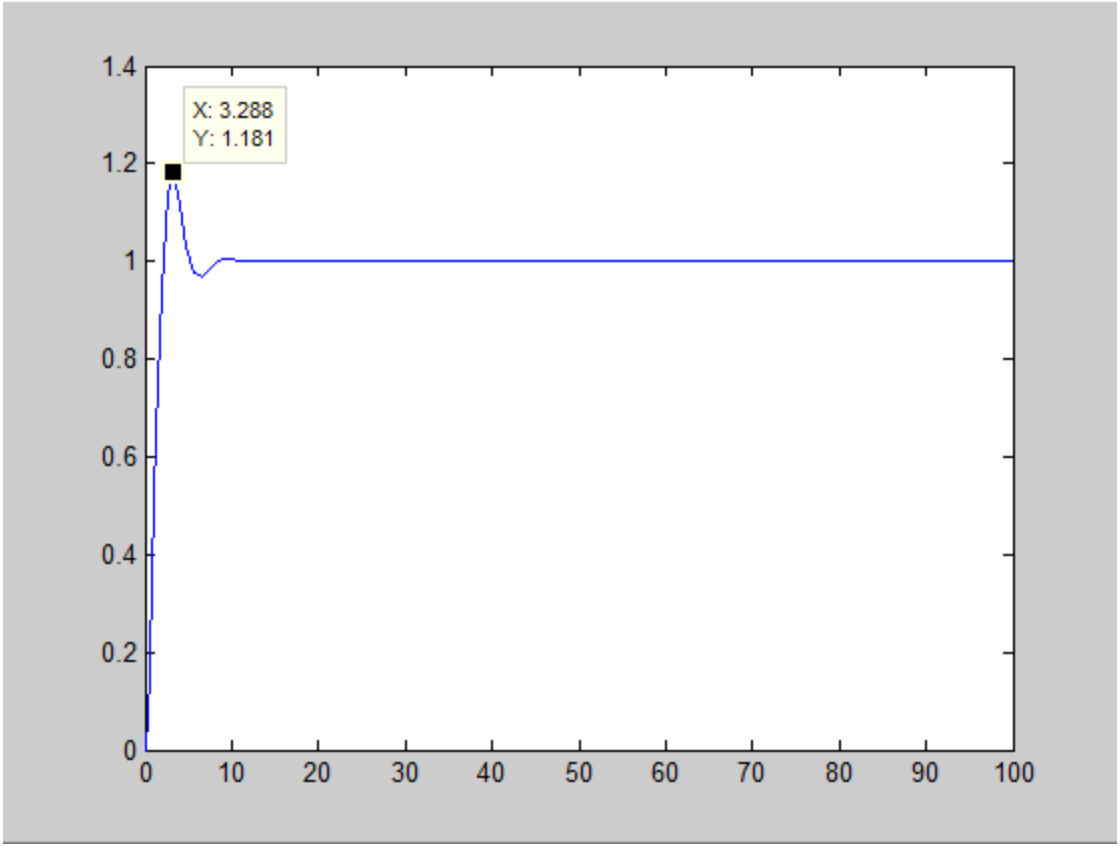

Figure 5:
Simulink representation of transfer function with P I and D values quantified by Zeigler method. Constant input of 1 into system. 18% overshoot.

Quantifying System Parameters

At steady state all the "s" terms of Figure 1 reduce to zero. The terms left are referred to as the DC steady state gain, and can be quantified by (neglecting the motor assuming it is much faster)

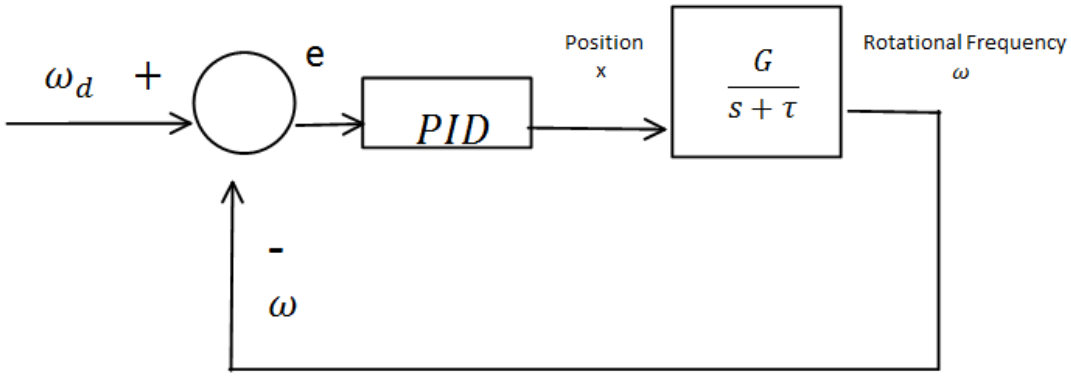

Further considering steady state,

$$\frac{\mathrm{G}}{\tau} = \frac{\Delta\omega}{\Delta x} = \frac{\mathrm{K}_t}{\mathrm{R\ B_L\ B_M}} \qquad \text{(EQ)}$$

So the idea is not to get slowed down by quantifying individual parameters rater allow the DC steady state gain G, represent the quantity, $\frac{\mathrm{K}_t}{\mathrm{R\ B_L\ B_M}}$. What is needed now is the relationship ratio of percent change in frequency to change in linear actuation.

$$\frac{\Delta\omega}{\Delta x} = ratio\ of\ change\ in\ frequency\ to\ change\ in\ linear\ actuation$$

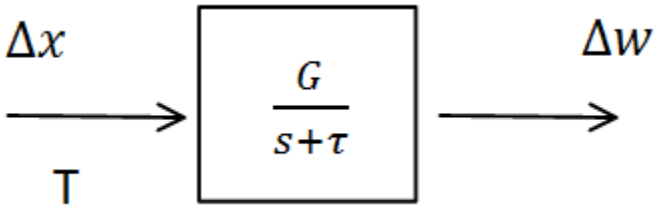

The system should now be simulated using the topmost block diagram, and scope set to the position, outside the PID controller to see if it operates in the acceptable range of our linear actuator. Where τ is the time constant of the rotor, it can be experimentally measured by timing the rotors time to stop after a constant velocity had been applied, mathematically this can be quantified as

$$\tau = \frac{settling\ time}{4} = \mathrm{B/J}$$